Measurement and correction of aberrations in light and electron microscopy

Jonas Binding

Dissertation

submitted to the

Combined Faculties for the Natural Sciences and for Mathematics

of the Ruperto-Carola University of Heidelberg, Germany

for the degree of

Doctor of Natural Sciences

and to the

Université Pierre et Marie Curie of Paris, France

Speciality Physics

(ED 389 - La Physique de la Particule à la Matière Condensée)

for the degree of

Docteur de l'Université Pierre et Marie Curie

Put forward by

Diplom-Physiker Jonas Rolf Hans Binding

born in Heidelberg, Germany

Oral examination: 15th of June, 2012
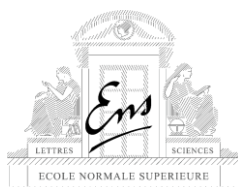
Measurement and correction of aberrations in light and electron microscopy

Examining committee:

Prof. Dr. Matthias Bartelmann	Jury member
Prof. Dr. Claude Boccara	Thesis advisor France; invited jury member
Dr. Laurent Bourdieu	Jury member
Prof. Dr. Winfried Denk	Thesis advisor Germany
Prof. Dr. Rainer Heintzmann	Referee
Prof. Dr. Agnès Maître	Jury member
Prof. Dr. Rasmus Schröder	Jury member
Prof. Dr. Tony Wilson	Referee

Abstract (English)

Imperfections in image formation, called aberrations, often preclude microscopes from reaching diffraction-limited resolution. Aberrations can be caused either by the microscope itself or by the sample and can be compensated for by using an active element integrated into the beam path which is functioning as a corrector. The optimal settings for this corrector need to be determined without excessive damage to the sample. In particular, for sensitive biological samples, the potential gain for signal and/or resolution needs to be weighed against sample damage.

Here I present the development of a special type of optical coherence microscopy (called deep-OCM), which allows the precise determination of the average rat brain refractive index *in vivo*. The conclusion is that two-photon microscopy is affected by optical aberrations in this sample starting at depths around 200 µm. Deep-OCM is well suited for imaging myelinated nerve fibers. Individual fibers can be visualized in the living brain in unprecedented depths beyond 300 µm.

In the second part of this thesis I describe the development and testing of an auto-focuser and auto-stigmator (called MAPFoSt) for a scanning electron microscope to ensure optimal imaging quality after switching samples or during long acquisition series. MAPFoSt determines the three focus and stigmation parameters from only two test images.

Keywords: Adaptive Optics, Wavefront, Refractive Index, Myelin, Optical Coherence Microscopy, Autofocus, Phase Diversity

Résumé (français)[1]

La diffraction constitue une limite fondamentale en microscopie, mais souvent cette limite n'est même pas atteinte. Des imperfections dans la formation d'image, appelées aberrations, peuvent être induites par le microscope ou l'échantillon. Un élément actif, dit correcteur, est intégré au chemin optique pour leur compensation. Les paramètres de ce correcteur doivent être déterminés sans dommage excessif pour l'échantillon. Il faut comparer le gain en signal et/ou en résolution avec cet endommagement, surtout pour des échantillons biologiques fragiles.

En première partie de cette thèse je présente une modalité particulière de la microscopie par cohérence optique (nommé deep-OCM). Ce développement a permis la mesure exacte et in vivo de l'indice de réfraction moyen du cerveau du rat. Cette valeur implique que la microscopie bi-photonique est limitée par des aberrations optiques à partir d'une profondeur de 200 µm dans ce type d'échantillon. Le deep-OCM est bien adapté à l'imagerie de fibres nerveuses myélinisées. Des fibres individuelles peuvent être visualisées in vivo dans le cerveau à des profondeurs auparavant inaccessibles, supérieures à 300 µm.

Dans la deuxième partie de cette thèse je présente le développement d'un autofocus et auto-stigmateur (nommé MAPFoSt) pour le microscope électronique à balayage qui permet d'assurer la qualité maximale des images lors d'un changement d'échantillon ou pendant des séries d'acquisitions de longue durée. MAPFoSt permet de déterminer avec précision les trois paramètres du focus et du stigmatisme en utilisant seulement deux images de test.

Mots clés : optique adaptative, front d'onde, indice de réfraction, myéline, microscopie par cohérence optique, autofocus, diversité de phase

---

[1] Un résumé substantiel de cette thèse se trouve à la fin du document, à partir de la page 132.

Zusammenfassung (deutsch)

Abbildungsfehler, so genannte Aberrationen, verhindern in der Mikroskopie häufig das Erreichen einer beugungsbegrenzten Auflösung. Aberrationen können durch Unzulänglichkeiten im Mikroskop verursacht sein, oder andererseits durch die Probe selbst. Zur Korrektur wird ein aktives Element in den Strahlengang integriert. Insbesondere für empfindliche biologische Proben müssen jedoch die Parameter des Korrektors bestimmt werden, ohne die Probe zu sehr in Mitleidenschaft zu ziehen; daher muss der mögliche Gewinn an Signalstärke und/oder Auflösung gegen die Schädigung der Probe abgewägt werden.

Im ersten Teil dieser Arbeit beschreibe ich die Entwicklung einer speziellen Form der optischen Kohärenzmikroskopie (genannt deep-OCM), die die exakte Bestimmung des mittleren Brechungsindex des lebenden Rattenhirns erlaubt. Daraus ergab sich, dass die Zwei-Photonen-Mikroskopie für diese Probe spätestens ab 200 μm Tiefe durch optische Aberrationen limitiert ist. Deep-OCM eignet sich zur Abbildung von myelinisierten Nervenfasern. Einzelne Fasern können im lebenden Gehirn in bisher unerreichbarer Tiefe von über 300 μm dargestellt werden.

Im zweiten Teil dieser Arbeit präsentiere ich die Entwicklung und Charakterisierung eines Autofokus und Autostigmators (genannt MAPFoSt) für ein Rasterelektronenmikroskop, der nach Probenwechsel oder bei langen Aufnahmeserien die optimale Abbildungsqualität sicherstellt. MAPFoSt ermöglicht es, mit nur zwei Testbildern die drei Fokus- und Stigmationsparameter zu bestimmen.

Schlagworte: Adaptive Optik, Wellenfront, Brechungsindex, Myelin, Optische Kohärenzmikroskopie, Autofokus, Phase Diversity

This thesis was carried out as a cotutelle project with enrollment at the Ruperto-Carola University (Heidelberg, Germany) and the Université Pierre et Marie Curie (Paris, France). The research was done at the Institut de Biologie de l'Ecole Normale Supérieure (Paris) under the supervision of Dr. Laurent Bourdieu, at the Institut Langevin, ESPCI ParisTech under the supervision of Prof. Dr. Claude Boccara and at the Max Planck Institute for Medical Research (Heidelberg), Germany, in the department of Biomedical Optics under the supervision of Prof. Dr. Winfried Denk. I have conducted the experiments myself, except when noted otherwise, and prepared the dissertation myself. All resources used (literature, equipment) are specified.

Parts of this dissertation have been published in:

1. BINDING, J., BEN AROUS, J., LÉGER, J.-F., GIGAN, S., BOCCARA, C. & BOURDIEU, L. (2011). Brain refractive index measured in vivo with high-NA defocus-corrected full-field OCT and consequences for two-photon microscopy. Opt. Express **19**(6), 4833-4847.
2. BEN AROUS, J., BINDING, J., LÉGER, J., CASADO, M., TOPILKO, P., GIGAN, S., CLAUDE BOCCARA, A. & BOURDIEU, L. (2011). Single myelin fiber imaging in living rodents without labeling by deep optical coherence microscopy. J. Biomed. Opt. **16**(11), 116012.
3. BINDING, J., S. MIKULA, S. & DENK, W., Low-dosage Maximum-A-Posteriori Focusing and Stigmation (MAPFoSt), submitted.

Contents

1   Introduction

1.1   We want to image the brain

To many people the brain is the most fascinating organ of the human body, and much of its function still escapes our understanding. Since fundamental advances in understanding are often brought about by the availability of new techniques, our aim is not only to study the brain, but also improve upon the existing imaging techniques.

While there is a lot of work being done in neuronal cell culture and organotypic brain slices, there is an increasing interest in observing the circuits of the brain *in vivo*, putting severe accessibility and environmental constraints on the experimental apparatus. Even when considering organisms much smaller than humans, e.g. common lab animals such as mice or rats, the brain has a diameter of many millimeters, while individual functional units such as dendritic spines can have diameters below 100 nm (Harris & Kater, 1994), requiring experimental procedures spanning several orders of magnitude in size. Blood vessels are found throughout the brain, blocking visible access to regions behind them (Haiss, et al., 2009). Visible light is strongly scattered by blood vessels, with the mean free path between scattering events as low as a few hundred microns (Vo-Dinh, 2003). In such an environment it is clear that for a thorough understanding, a multitude of observational methods should be combined, for example pharmacological studies, electrophysiology, and different imaging modalities such as magnetic resonance imaging, light microscopy and electron microscopy.

1.2   Optical aberrations cause imperfect imaging

Imaging is the predominant form of data collection in natural science. Images are well adapted for further processing by the human mind, allowing quick hypothesis testing even before resorting to complex mathematical analysis methods. It provides a highly intuitive representation of raw experimental findings from the sub-nanometer scale to the scale of millions of light years, for example scanning probe microscopy such as scanning tunneling microscopy (Binnig, et al., 1982b; Binnig, et al., 1982a) on one extreme and astronomic imaging of galaxy clusters (for example George, et al., 2009) on the other.

Most imaging systems rely on particle beams or electromagnetic radiation, which is focused by an optical system (Figure 1-1a) on some type of detector. In either case, imperfect focusing can lead to sub-optimal images which reduces the amount or quality of information obtained.

Even though post-processing can often boost the remaining information to make it more visible, and analysis might still allow experimenters to answer the underlying scientific questions, information that is not contained in the initial images cannot be restored.

The reasons for imperfect imaging are generally referred to as optical aberrations. Aberrations can be caused by imperfections in the components of the imaging system, by misalignment of these components (Figure 1-1b) or by sources outside the experimenter's control such as the sample itself (Figure 1-1c).
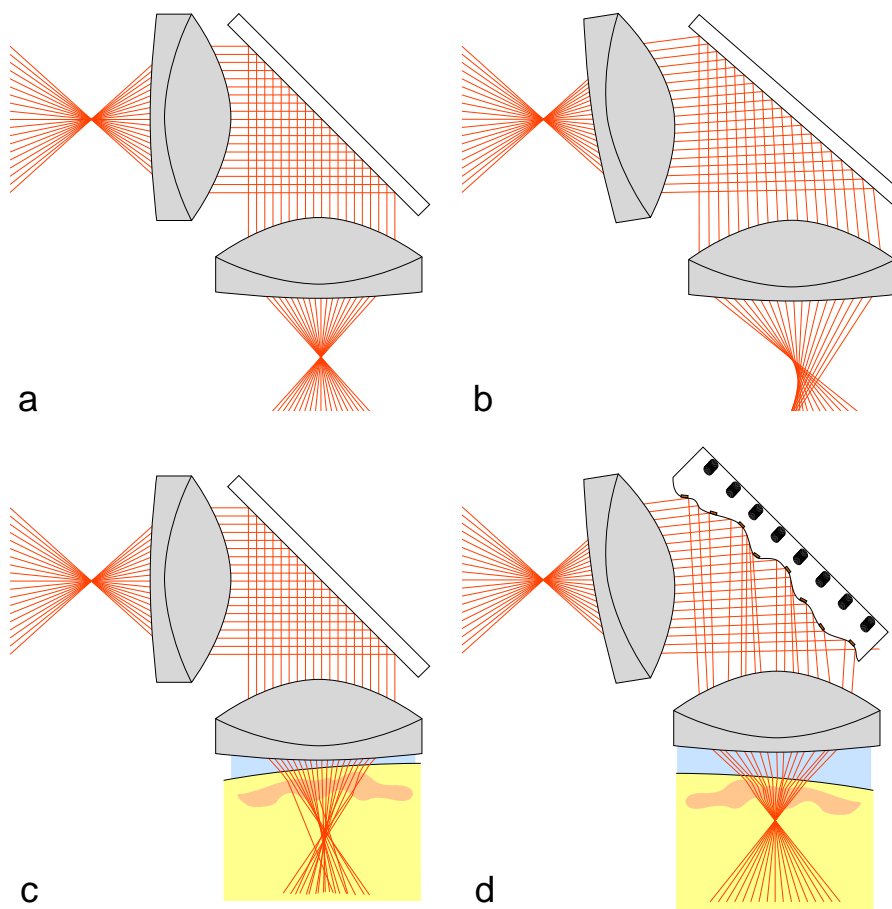
Figure 1-1. a) perfect imaging system, b) misaligned system, c) system with sample-induced aberrations, d) system with aberration correction

1.3   Aberrations can be thought of as a phase term on the wavefront

An aberration-free imaging system in geometric optics approximation would focus the entire signal from one object point onto one point on the detector (Figure 1-1a), corresponding to a spherical wavefront in wave optics leading to a diffraction-limited focus. All deviations of the

particle paths or light rays causing them not to reach their common detector point are considered aberrations. In the wave optics case, this corresponds to deviations of the wavefront from the spherical shape. Since the wavefront is the surface of constant phase of a wave, the aberrations can most simply be expressed as the phase difference between the optimum spherical reference surface and the actual wavefront. This phase term can be used to calculate the point spread function (PSF) of the aberrated system (Sheppard & Cogswell, 1991; Born & Wolf, 1999).

1.4 Many imaging systems can be limited by aberrations

For several hundred years, microscopes and telescopes were limited by imperfections in lens and mirror production. With improving manufacturing techniques, astronomers were the first to acknowledge that eventually their telescopes would be limited by a component out of their control: atmospheric turbulence. The rapid changes in refractive index of the atmosphere due to moving air aberrate the images taken by all ground-based telescopes and limit their achievable resolving power (Hardy, 1998).

In ophthalmology, the imperfections of the human cornea make diffraction-limited imaging of the retina equally difficult (Dreher, et al., 1989; Liang, et al., 1994).

In free space communications, near-earth atmospheric fluctuations limit feasible signal transmission distances, energy efficiency and data rates (Levine, et al., 1998).

In electron microscopy, changing microscope parameters such as beam current and electron landing energy can require a realignment of astigmatism and change the working distance, inducing defocus.

In light microscopy of three-dimensional samples, refractive index fluctuations of superficial sample layers can aberrate images of deeper layers (Figure 1-1c). The exact influence of aberrations depends on the type of microscope and will now be discussed briefly for different systems.

1.4.1 Wide-field microscopy

In classic wide-field microscopy of thick samples, classical aberrations are of little consequence, since blurred, out-of-focus regions dominate the signal degradation. In other words, even if there are no aberrations present, this technique is inherently limited by the lack

of optical sectioning and is therefore, in its standard form, only used for thin sections and moderately thick samples.

3D deconvolution wide-field microscopy aims to remove said out-of-focus light. To do this correctly, it can be important to take the increase of aberrations with depth into account during the deconvolution (Hanser, et al., 2001). The most common example of a spatially variant PSF is a PSF changing with imaging depth; imaging into a sample with refractive index mismatch causes defocus (axial focus shift) and spherical aberration to increase with depth.

Since deconvolution is unavoidable in this system, it is unclear if adding a physical wavefront correction scheme would be a large benefit.

1.4.2   Confocal microscopy

In confocal microscopy, a collimated laser beam is focused into the sample, where it excites fluorophores and/or is partially reflected, or scattered, everywhere along the double cone traversed by the light. For detection, the geometrical focus is imaged onto a small aperture, the confocal pinhole, which blocks the majority of out-of-focus light from the detector while letting most light from the focal region through. If the sample and immersion medium match the specifications of the objective with respect to the refractive index, confocal microscopy allows diffraction-limited imaging and a non-paraxial wave optics theory is needed to describe the imaging properties and possibly even the full vectorial theory at extremely NA (Richards & Wolf, 1959).

Aberrations in the excitation path will decrease the density of excitation light in the focal volume, while aberrations in the detection path will cause light from the geometrical focus to be spread over an area larger than the pinhole. Both effects thus decrease the detection efficiency of the microscope, on top of the resolution decrease caused by the aberrations.

1.4.3   Two-photon microscopy

In two-photon laser scanning microscopy (2PLSM; Denk, et al., 1990), a femtosecond-pulse laser beam is focused into the sample exactly like in confocal fluorescence microscopy, except that the laser is now run at a wavelength suitable for two-photon absorption by the fluorophore, i.e. roughly twice the wavelength of the one-photon absorption spectrum used in a normal confocal microscope. Since the cross-section for two-photon absorption depends

quadratically on the local light density, fluorophore excitation is confined to the vicinity of the focus where sufficient densities are reached during the femtosecond laser pulse. Detection can either collect all light at the emission wavelength of the fluorophore, or spatially filter using a pinhole exactly as in confocal microscopy. While the latter case maximizes resolution at shallow depths, the former is often preferable for deep imaging since it allows detection of photons that were scattered one or several times on their way to the detector.

In non-confocal two-photon microscopy, only aberrations on the excitation path are important for image resolution. Since two-photon microscopy relies on the precise temporal structure of the light pulse, both dispersion and optical aberrations can decrease the signal strength by spreading out the light density in the focal volume temporally (Andegeko, et al., 2009) or spatially (Jacobsen, et al., 1994).

1.4.4 Structured illumination microscopy

In Structured illumination microscopy (SIM), a spatial pattern of light is projected into the sample, which allows separation of focal-plane light from out-of-focus light by demodulating the signal using the illumination structure. Some aberration modes are highly detrimental to the illumination structure and therefore degrade the images very strongly. Other aberration modes modify the PSF in a way that preserves the illumination structure, causing much less degradation to image quality. (Débarre, et al., 2008)

1.4.5 PALM/FPALM/STORM

In (F)PALM/STORM (Betzig, et al., 2006; Hess, et al., 2006; Rust, et al., 2006), the positions of all fluorophores in a sample are mapped out by not exciting them all at the same time, but using switchable or activatable fluorophores which are imaged sequentially, allowing their respective positions to be determined with a precision far beyond the size of their focal spots.

2D PALM/STORM generally only needs to determine the center of mass (COM) of each focal spot. If aberrations blur the focal spot, its COM might be shifted slightly, for example due to coma. However, if the PSF remains spatially invariant this is an inconsequential global shift. As long as different fluorophores which emit simultaneously are far enough apart to be separated, the technique is insensitive to aberrations, except for the decreasing precision in COM position determination.

3D PALM/STORM often determines z-position from the shape of the PSF, making it highly sensitive to PSF-shape-changing aberrations. A counter-example is biplane FPALM (Juette, et al., 2008), which only requires a correct estimate of the axial (i.e. laterally integrated) PSF, greatly reducing the number of aberration parameters that need to be estimated. What's more, biplane FPALM would be directly suitable to implement phase diversity using the images from the two planes.

1.4.6 Stimulated emission depletion

In stimulated emission depletion (STED) microscopy, the excitation beam focus is superimposed with a doughnut-shaped STED laser beam, which depletes the excited fluorophore state by stimulating emission at its particular wavelength (Hell & Wichmann, 1994; Klar, et al., 2000). The signal detected in the rest of the emission spectrum of the fluorophore thus originates only from the very center of the excitation focal volume, where the STED beam intensity is close to zero. The final resolution of the system depends on the steepness of the STED beam intensity gradient around the zero.

Aberrations can decrease the excitation intensity around the central zero of the STED beam, can cause the STED beam zero to become misaligned with the excitation beam and/or distort the STED beam so as to decrease the intensity gradient. The exact effect depends both on the aberration mode, and on the phase profile used for the STED beam (Deng, et al., 2010).

1.4.7 Optical coherence tomography

Optical coherence tomography (OCT) is an imaging technique where backscattered light from different depths is discriminated interferometrically (Fujimoto, et al., 1995; Fercher, 1996; Tearney, et al., 1996). This can be done, for example, by selecting only signal from a fixed depth using a white light source (i.e. short temporal coherence) with a modulation of the reference arm and lock-in detection of the modulated signal. This allows two- and three-dimensional imaging using the local backscattering coefficient as a source of endogenous contrast. In particular for full-field OCT (Beaurepaire, et al., 1998; Dubois, et al., 2002; Vabre, et al., 2002), the microscope objective and the sample constitute one arm of a Linnik interferometer. Lateral resolution is dominated by the resolving power of the objective, while axial resolution can either be dominated by a confocal-like effect (for high numerical aperture (NA) and long coherence length) or by the coherence length (when it is short and the NA is low).

18

In high-NA variants of OCT, some of which are referred to as Optical Coherence Microscopy (OCM; Izatt, et al., 1994), signal strength is sensitive to defocus – in contrast to most other epi-detection microscopes, which are only sensitive to higher aberration modes. When the reference arm length defining the imaging depth does not match the focus depth of the objective, the confocal effect decreases signal and resolution. Higher order aberrations can, in principle, also play a role but are often strongly dominated by defocus.

1.5 Astronomy uses direct wavefront measurement

Several methods have been developed over the years to determine the aberrations present in an optical wavefront. For individual optical components such as lenses, one can analyze their imperfections by passing light from a collimated laser beam or from a point source through the component, causing its aberrations to be imprinted in the beam wavefront. This wavefront can then be analyzed using a Shack-Hartmann-Sensor (Hartmann, 1900; Shack & Platt, 1971), a pyramid sensor (Ragazzoni, 1996), a curvature sensor (Roddier, 1988) or an interferometer such as a Twyman-Green interferometer (Twyman & Green, 1916) or a shearing interferometer (Bates, 1947).
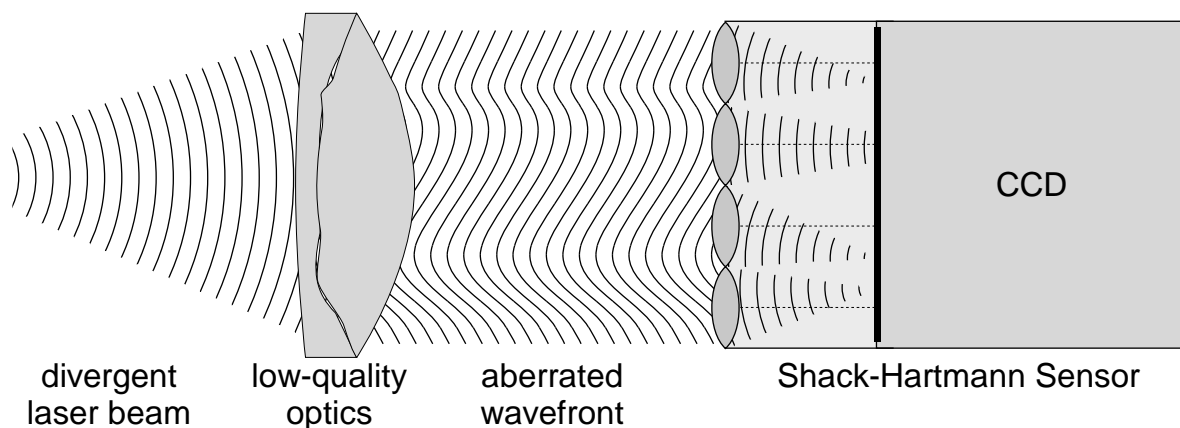
Figure 1-2. The wavefront of a laser beam (far left) is aberrated by a low-quality optical component (center left), which is analyzed using a Shack-Hartmann Sensor (right) consisting of a lenslet array and a CCD.

These methods (except interferometry) are generally also applicable to measuring atmospheric aberrations using the light coming from an individual star of sufficient brightness, or from an artificial guide star created by exciting fluorescence in high atmospheric layers using a strong, focused laser beam (Tyson, 1997). Similarly in ophthalmology, a test beam reflected off of the retina can generate a test beam containing the

aberrations (Prieto, et al., 2000). In fluorescence microscopy it might sometimes be possible to introduce a strongly fluorescent test bead near the region(s) to be imaged and use its fluorescence signal with one of the above methods (Azucena, et al., 2011), but the introduction of beads is certainly not a universally feasible option.

1.5.1 Why direct wavefront sensing is hard in microscopy

Unfortunately, none of these methods seem particularly suited for determining the optimal wavefront for focusing inside three-dimensional biological samples where subsequent optimized imaging at different depths can be required. The root of the problem is that different layers of the sample will generally participate in any wavefront measurement, presenting the wavefront sensor not with one clean wavefront, but with a superposition of a multitude of wavefronts, which cannot be separated and which hinder each other's measurement. While the Shack-Hartmann sensor has been successfully adapted to laterally extended objects for solar adaptive optics (Rimmele & Radick, 1998), dealing with wavefronts from different depths in the sample is not possible with this method.

To separate wavefronts coming from different depths in biological samples, coherence gated wavefront sensing (CGWS) has been developed, where an interferometer illuminated by a broad-band spatially coherent source performs depth discrimination of backscattered light, phase shifting is used to reconstruct the complex field and a virtual Shack-Hartmann sensor is used for phase unwrapping (Feierabend, et al., 2004; Rueckel, et al., 2006). While this technique has proven successful for measurement of aberrations when imaging through the skull of transparent zebrafish, it is relatively complex to implement on an existing microscope. What's more, it requires a scattering sample with a random distribution of scatterers, but scattering must be weak enough for single scattering to still be dominant in the depths where aberrations are to be measured (Binding & Rückel, in preparation).

For deep brain imaging in rodents, the short scattering length seems to place a severe limitation on the usefulness of CGWS. In particular, the speckle size of the coherence-gated electromagnetic field decreases quickly with penetration depth (Markus Rückel and Jinyu Wang, both private communication). Initial tests optimizing two-photon fluorescence signal in the rodent cortex with a deformable mirror by manually optimizing spherical aberration and lowest-order astigmatism did not show significant improvements (Binding, 2008). It was therefore unclear whether optical aberrations do not play a significant role in this system, or whether they are just complicated to measure and to correct.

20

1.6 The sample refractive index sets the scale for aberrations

Microscope objectives used in light microscopy are optimized to be used at a fixed sample refractive index, for example for the refractive index of air (n = 1.0), water (n = 1.33), glycerol (n = 1.47) or oil (n = 1.515). For any sample not matching the refractive index that the objective was designed for, the refractive index mismatch will induce aberrations. For a flat surface orthogonal to the optical axis, only rotationally symmetric aberrations can exist, i.e. defocus and (all orders of) spherical aberrations. For the general case of a non-flat or non-orthogonal surface, other aberrations will also be present.

The aberrations increase in severity with the imaging depth in the sample and with the difference in refractive indices. To estimate in which depths they become a problem, it is therefore important to know the refractive index of the sample. However, *in vivo* measurements of the refractive index *n′* for brain tissue did not previously exist in the literature.

1.7 Our refractive index measurements led us to develop deep-OCM

An OCT-based technique to measure *n′* had been described (Tearney, et al., 1995) which seemed applicable to *in vivo* brain measurements in lab animals. It can provide OCT brain images at the same time as measuring the average refractive index. However, in its existing form, the method used by Tearney and colleagues used low numerical aperture objectives, limiting the attainable measurement precision. From previously published *ex vivo* values for brain refractive index (Table 4-1) we estimated that Tearney's method could only determine the water-brain refractive index mismatch with 30 to 70% error. The theoretical framework was not sufficiently developed to correctly deal with effects of group velocity dispersion or high numerical apertures.

We therefore implemented the OCT-based refractive index measurement on a full-field OCT (ff-OCT) setup using high-NA objectives to improve measurement precision.

Ff-OCT is physically very similar to CGWS and therefore, as a side-effect, allowed us to learn how to maximize the attainable penetration depths in both ff-OCT and CGWS. We combined several depth-improving features in our ff-OCT setup and called the resulting method deep-OCM, which is described in chapter 1.

We found that deep-OCM is capable of visualizing individual myelinated axons in the upper layers of the somatosensory cortex. Using the same setup, the general structure of myelin in

nerve bundles in the peripheral nervous system (PNS) can also be visualized. Myelin imaging in both systems is presented in chapter 1.

Finally, we used this setup to measure the refractive index of the somatosensory cortex of seven rats *in vivo*, taking both dispersion and the high NA into account in data analysis. This work is described in chapter 1.

1.8 Deep rat brain imaging is limited by aberrations

The consequences of the measured refractive index for imaging the rat brain are discussed in chapter 1. Using two-photon imaging as an important example of deep *in vivo* imaging, it is found that imaging depth is severely limited by spherical aberration. Based on this information, we have started to implement a new CGWS-based system to measure aberrations in the rat brain at the Institut Langevin; the project is currently pursued by post-doc Jinyu Wang (Wang, et al., 2012) and will not be discussed in detail here.

1.9 Image analysis allows indirect wavefront measurement

Due to the lack of a generally usable direct wavefront sensing approach for microscopy, and the inherent complexity of the interferometric approach of CGWS, considerable interest has been focused on indirect methods for determining the wavefront.

The general principle is to use the effects of aberrations on the images to determine the best possible aberration correction. Using an active element in the beam path, known aberrations are deliberately added before recording each image. The analysis then concentrates on how these additional known aberrations, called test aberrations, modify the images. The same active optical element is generally used for creating the test aberrations and for aberration correction, so often no other hardware modifications are needed in the system. This is in sharp contrast to direct wavefront measurement which invariably adds extra hardware, such as an extra light path for a Shack-Hartmann sensor (SHS) or an interferometer.

Currently existing methods of wavefront measurement through image analysis can be classified into one of four categories: imaging-model-agnostic methods, metric-based modal wavefront sensing, pupil segmentation, and phase diversity.

1.9.1 Metric-based, imaging-model-agnostic methods

In some cases, an imaging system is not well understood and there is no theoretical model describing how aberrations will affect the imaging process. However, a metric can be defined

which quantifies image quality and which takes its maximum for aberration-free images. For example, image contrast and image sharpness are two common metrics. In such cases, metric-based but imaging-model-agnostic methods have been demonstrated to improve image quality, such as hill climbing (Marsh, et al., 2003), genetic search (Sherman, et al., 2002) or simulated annealing (Zommer, et al., 2006).

The downside of these methods is that they can be rather slow to converge to a solution, and there is no way to verify whether a solution they found is truly optimal or whether the algorithm is stuck in some local maximum. In fact, the lack of a model can prevent any theoretical analysis of the range of convergence. Conversely, if a model does exist, using a metric-based imaging-model-agnostic approach discards information which can be used to speed up convergence, as will be described below.

1.9.2 Metric-based modal wavefront sensing

An imaging-model-based approach developed by the Wilson group is called modal wavefront sensing (Debarre, et al., 2007) (Neil, et al., 2000; Débarre, et al., 2008; Débarre, et al., 2009) and is described briefly in the appendix (chapter 9.4). It is also metric-based, reducing each test image acquired with given test aberrations to one metric value, as above. However, in contrast to the imaging-model-agnostic methods, the imaging model is used to determine an orthogonal set of test aberration modes which act independently on said metric, allowing the determination of the optimum aberration correction from only three test images per mode as long as aberrations are small enough (Figure 1-3). The orthogonality ensures that each parameter is determined independently of the other parameters, leading to non-iterative (one-step) convergence.

While such an approach allows a simple and stable implementation of the aberration correction scheme once the set of test aberration modes has been determined, it still throws away some information due to the use of one single metric, which is chosen heuristically amongst a large number of possible choices, many of which could yield additional complementary information.
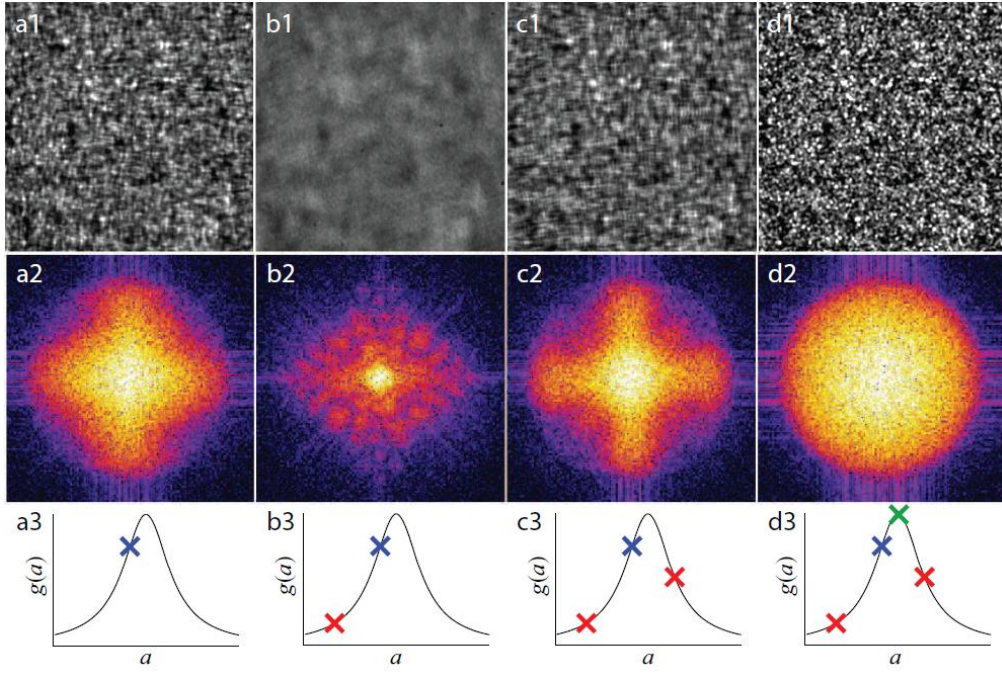
Figure 1-3. General procedure of modal wavefront sensing for one mode. Three test images of the speckle pattern (a1, b1, c1) taken while modifying one specific aberration mode are the Fourier transformed (a2, b2, c2) to calculate their respective metric values (a3, b3, c3). The knowledge of the shape of the metric curve (solid line) allows the determination of the optimal value for that mode (d1, d2, d3). This figure was taken from (Debarre, et al., 2007), reprinted by permission from Optical Society of America: Optics Express, copyright 2007.

1.9.3 Pupil segmentation

A radically different approach has been proposed under the name of pupil segmentation (Ji, et al., 2009). Here, the test aberration used in the pupil plane of the microscope objective is not a phase modulation, but a spatial amplitude modulation. By exciting fluorescence not through the full pupil, but through different subregions of it (using small beamlets instead of the full laser beam) and acquiring a separate two-photon image with each beamlets, laterally shifted low-resolution images can be acquired (Figure 1-4). The exact amount of lateral shift for each subregion is determined through image cross-correlation and gives an estimate for the average wavefront tilt on that region. In a sense, this method can be described as an inverse Hartmann test, where it is not an aberrated outgoing wavefront which is spatially subdivided to determine local wavefront tilts, but rather the unaberrated incoming excitation laser beam. One disadvantage of this approach is that the reduced excitation NA requires a high laser power and significantly decreases the sectioning ability of the microscope, making it prone to

cross-talk from bright fluorescent objects in planes close to the desired focus (Heintzmann, 2010).
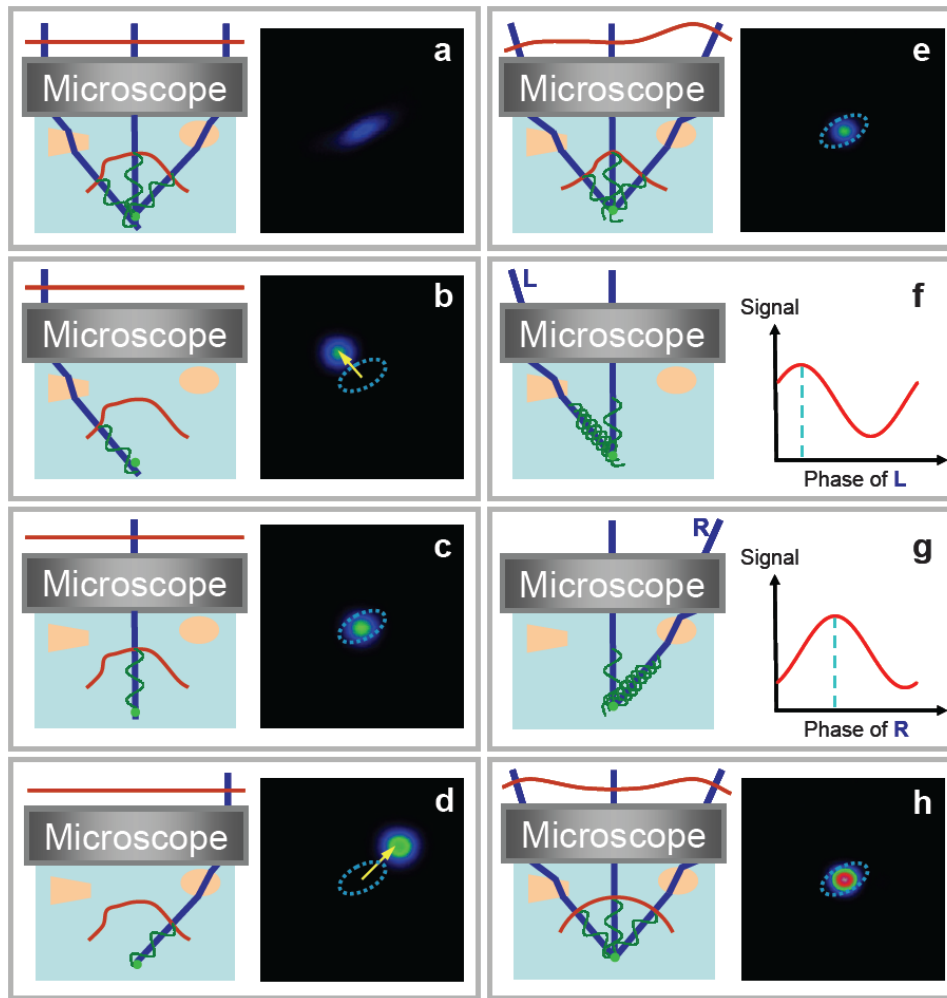
Figure 1-4. Sketches illustrating pupil segmentation adaptive optics using three independent subregions, creating three beamlets (blue rays). (a) Aberrated wavefront (red) due to refractive index inhomogeneities (orange) leads to an aberrated image of a reference bead. (b, c, d) Images acquired with the left, center, and right subregions, respectively, permit the tilt of each beamlet to be measured from the displacement of the bead. (e) Beamlets intersect at a common point, after appropriate compensatory tilts are applied at the SLM. (f) Interference of left beamlet with central reference beamlet, at several phase offsets (green sinusoids) applied to the former, determines the optimal phase offset (dashed aqua line); (g) Same procedure applied to the right beamlet. (h) Final corrected wavefront (red) and recovered diffraction-limited focus. This figure was taken from (Ji, et al., 2009), reprinted by permission from Macmillan Publishers Ltd: Nature Methods, copyright 2009.

While the relative shift of the individual low-resolution images clearly gives the dominant and most-easily-analyzed information about the aberrations present in the images, it seems that, for example, the relative sharpness of the different images could also contain some information about higher order aberrations. A theoretical investigation of the information efficiency of pupil segmentation is still lacking, but it seems clear that not all available information is being used.

A more recent method called pupil-segmentation with full-pupil illumination (Milkie, et al., 2011) is actually a metric-based, zonal approach where they reverted from amplitude modulation to the more common phase modulation. It uses total image intensity as its metric and performs sequential 2D tip-tilt scans of different segments of the wavefront to determine the optimal tip/tilt in each region. While this mitigates the reduced excitation NA of their previous approach, a huge number of small-area test images needs to be taken, for example more than 3000 when using 32 pupil segments and testing 14x14 tip-tilt combinations for each pupil segment, as in one of their examples. As before, the choice of one single metric is bound to neglect a certain amount of information present, and there is no evidence that the heuristic choice of test aberrations made here is in any way superior to the test aberrations derived in modal wavefront sensing.

1.9.4 Phase diversity

While in principle most of the above methods are phase diversity techniques in that they record several images with test aberrations that only change in phase, the term is commonly used in a more limited sense.

The general principle of phase diversity is simple: given a small set of test images containing different (usually phase-only) test aberrations, determine the actual aberrations which are coherent with all test images at once. In other words, images are not reduced to metric values for further data analysis, but the full information content of different images is combined to find the most likely form of all aberration modes.

The exact implementation of phase diversity differs, with many heuristic approaches in microscopy over the years, for example in electron microscopy (Ogasawara, et al., 1998; Ong, et al., 1998; Baba, et al., 2001) and wide-field light microscopy (Hanser, et al., 2003; Hanser, et al., 2004).

For astronomical applications, a maximum likelihood (ML) approach had already been proposed much earlier (Gonsalves, 1982; Paxman, et al., 1992), but until now had little impact on aberration estimation in microscopy, possibly due to its increased mathematical complexity and the lack of interaction between the fields.

Compared to heuristic approaches, the maximum likelihood approach has the advantage of making best use of the available data. This is important, for example, for the biological brain samples analyzed in SBEM (Brickman et al), which mandate the lowest dose of electrons per area possible. For low-NA imaging of two-dimensional objects the work by Paxman and colleagues is, in principle, directly applicable to microscopy.

To demonstrate the power of the concept, we have implemented phase diversity on our scanning electron microscope, experimental results of which will be discussed in chapter 1. However, the computational burden of Paxman's algorithm and in particular the number of Fourier transforms required makes the use of large images routinely acquired in electron microscopy with sizes of 512 x 512 pixels and above prohibitively slow. Using the fact that the electron optics can be described geometrically and only defocus and astigmatism can be corrected, we were able to considerably speed up the algorithm and decrease the number of Fourier transforms necessary to a bare minimum. We call this modified algorithm Maximum A Posterior Focus and Stigmation (MAPFoSt) and show its ability to use extremely large, low-dose test images for defocus and astigmatism determination, while keeping the processing time reasonable. As the name suggests, we also investigated how the algorithm can use prior knowledge about aberrations and/or the object to improve the estimates, leading to a maximum-a-posteriori instead of maximum-likelihood method. Such prior knowledge could consist of upper bounds on aberration coefficients, based either on properties of the microscope or of the sample. It could also reflect the knowledge of the general distribution of aberration values and/or object structure from previous experiments.

2 Deep-OCM[2]

We developed deep-OCM from a combination of several improvements to full-field OCT (Beaurepaire, et al., 1998; Dubois, et al., 2002; Vabre, et al., 2002) which optimized the system both for *in vivo* refractive index measurements and high-resolution imaging at high depths. To reduce scattering, near infrared instead of visible light was used, requiring an InGaAs-based camera as a detector (Sacchet, et al., 2008). The camera was also chosen for its high full well capacity and for its fast image repetition rate. To improve lateral resolution (Dubois, et al., 2002) and improve refractive index measurement precision (see Chapter 4 or Binding, et al., 2011), high NA objectives (NA = 0.8) were used. Both the sample and the objective were motorized to allow our custom-written software algorithm to automatically correct defocus as described below. To minimize motion artifacts in the images, animals were only held by a metal plate glued to their skull directly surrounding the imaging region, while resting loosely on a heating blanket.

2.1 Details of the setup

The microscope (Figure 2-1) consisted of a low coherence light source (250W halogen lamp), with the standard Köhler microscope illumination, a Linnik interferometer (i.e. a Michelson interferometer with an objective in each arm), a tube lens and an InGaAs camera. The water immersion objectives used were Zeiss IR-Achroplan 40×/0.8W. The effective spectral bandwidth of the optical system, including the spectrum of the light source, the optical components (as well as water used for immersion) and the detector was centered on $\lambda = 1100$ nm and had a full width at half maximum (FWHM) of around 170 nm. For dispersion correction, a cover slip identical to that protecting the rat's cortex (see below) was placed in the reference arm of the interferometer. To avoid the reflection caused by this coverslip hitting the camera, the coverslip was tilted slightly. A 50cm doublet was used as a tube lens to image the sample and the reference arm mirror onto the InGaAs camera (Xeva-1.7-320,

---

[2] Large parts of this chapter are taken almost verbatim from BINDING, J., BEN AROUS, J., LÉGER, J.-F., GIGAN, S., BOCCARA, C. & BOURDIEU, L. (2011). Brain refractive index measured in vivo with high-NA defocus-corrected full-field OCT and consequences for two-photon microscopy. Opt. Express **19**(6), 4833-4847.

Xenics Infrared Solutions, Leuven, Belgium). The sensor chip had 320x256 pixels and was operated at its maximum frequency of 66 Hz, triggered by a NI 6722 digital I/O board (National Instruments, Austin, Texas) and controlled by the software, LightCT (LLTech, Paris). Both the sample z-position and the relative arm length could be changed with two motorized linear stages (M-VP-25XA, Newport). A synchronized rectangular 33 Hz signal drove the Piezo Linear Stage Actuator (PI P-753.11C, Physik Instrumente [PI] GmbH, Karlsruhe) onto which the reference arm mirror was mounted. The amplitude of the piezo actuator position change was adapted to $\lambda/4$, producing a change in reference arm length of $\lambda/2$. Taking the difference of subsequent camera images would therefore separate the interference signal (more exactly: the projection of the interfering electromagnetic field onto the real axis) from the background light, implementing a two-step phase stepping protocol. LightCT running on a standard PC allowed real-time display of these OCT images at 33 Hz.

For some experiments for myelin imaging with increased field of view, Olympus UMPlanF $10\times/0.3$ W objectives and a silicon camera (Pantera 1M60, Dalsa,Waterloo, Canada) were used. The effective spectrum in this case was centered on 775 nm and had a FWHM of 150 nm. This configuration is referred to as "deep red deep-OCM", in contrast to the "IR deep-OCM" mode using the InGaAs camera.

2.2 Animal preparation and treatment

All animal manipulation and surgical procedures were in accordance with the European Community guidelines on the care and use of animals (86/609/CEE, CE official journal L358, 18th December 1986), French legislation (décret no. 97/748, 19th October 1987, J. O. République française, 20th October 1987), and the recommendations of the CNRS.

Three 3-week-old (P20-21; weight ~80g), two 6-week-old (P45-46; weight ~250g) and two 12-week-old (P86-87; weight ~400g) male Wistar rats were included in this study. Rats were anesthetized by urethane injection (1.5 g/kg). Supplementary doses of urethane were applied when necessary. The body temperature of the animal was held at 38°C by a heating blanket during the surgery and the imaging. Animals were maintained in a stereotaxic frame during the surgical procedure. A craniotomy (~3 mm in diameter) centered over the somatosensory cortex was performed on the rat's left hemisphere and the dura mater was removed. The craniotomy was sealed with a 5mm diameter coverslip, which was glued onto the thinned skull surrounding the hole. Thinning was performed to bring the coverslip in close contact with the brain of the animal, in order to prevent movement of the brain during the imaging

procedure. For ff-OCT imaging, the animal was stabilized with a metal holder glued to its skull (Figure 2-1). At the end of the experiments, rats were injected with a lethal dose of urethane.
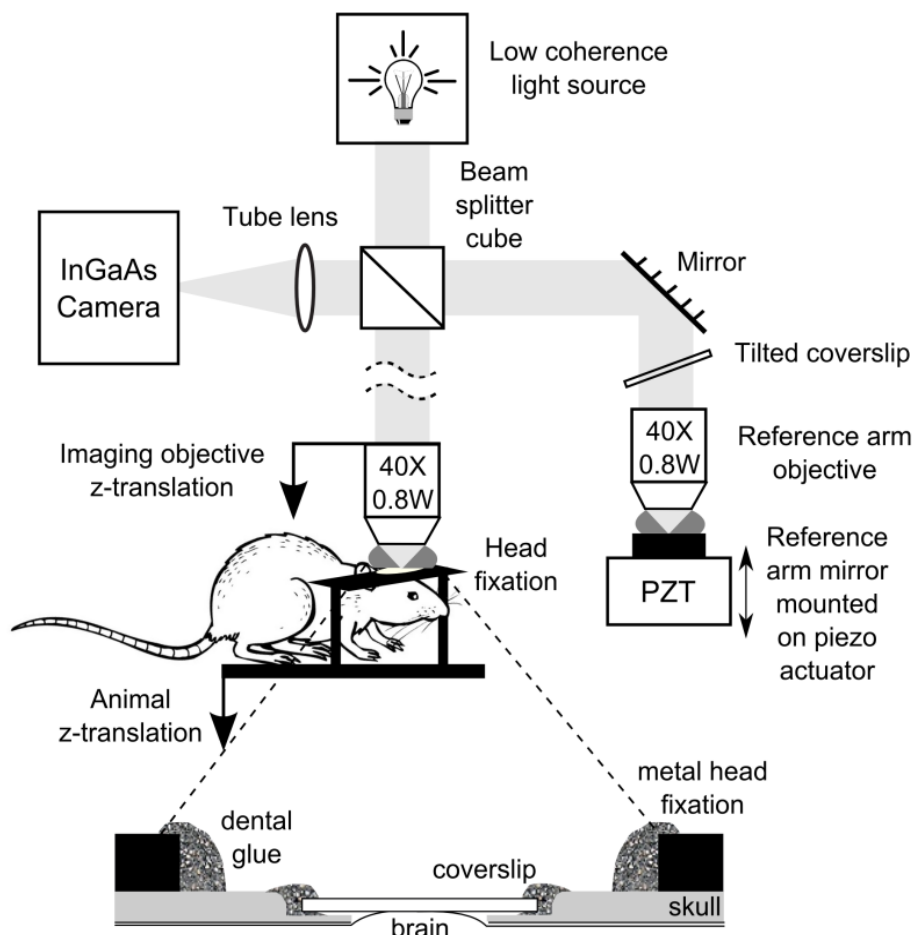
Figure 2-1. Ff-OCT setup and sample preparation. Light from a low-coherence source enters a Linnik interferometer. The sample arm consists of a microscope objective and of the sample, both of which are translatable along the optical axis by two motorized linear translation stages. The animal is held by a metal head fixation plate glued to its skull around the craniotomy, which consists of a cover slip glued onto the thinned bone around the actual opening, where the brain tissue comes into direct contact with the cover slip. The reference arm consists of a folding mirror, a cover slip to compensate for dispersion from the cover slip on the rat brain, an objective identical to the sample objective and a reference mirror mounted on a piezo actuator for phase-stepping. The focal planes of both objectives are imaged using a lens doublet serving as tube lens onto an InGaAs camera. The piezo, camera and both motorized stages are controlled by a standard PC running Light-CT software.

2.3 High-speed *in vivo* rat brain imaging shows blood flow

The camera in our system was fast enough to take the two images needed for optical sectioning before the respiration and heartbeat caused the cortex to move more than a small fraction of a wavelength. Even the movement of individual red blood cells in thin veins as well as the movement of leukocytes on the surface of larger vessels at the brain surface could be observed in real time with our OCT imaging frequency of 33 Hz (Figure 2-2 as well as Movie 1 & Movie 2).
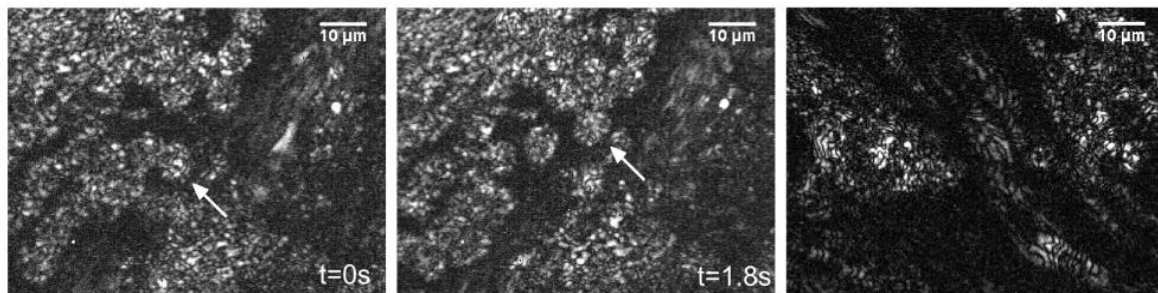
Figure 2-2. Single-frame excerpts from ff-OCT video recordings of surface blood vessels in rat cortex. (Left/Center, Movie 1) large vessel of a p46 rat; 6.6 Hz frame rate; produced from a 33 Hz video by averaging 5 ff-OCT images each to increase signal to noise. In the upper left hand corner the tissue surrounding the vessel can be seen; passing from lower left to upper center individual leukocytes can be seen moving slowly along the vessel wall (one of them is marked with a white arrow). The right half of the field of view shows the interior of the vessel where objects move too rapidly to be resolved individually. In the lower center of the field of view, the vessel wall descends into the coherence volume so that leukocytes can be seen as if through a semi-transparent wall. (Right, Movie 2) junction of two blood vessels joining in the cortex of a p21 rat. 33Hz frame rate, taken without any averaging. In the upper vessel, an individual object can be seen which moves much slower than the surrounding blood, possibly due to interactions with the blood vessel wall.

2.4 Importance of defocus correction for high-NA OCT and OCM

Most scanning OCT systems are inherently limited to extremely low NA objectives, since their axial scan range is limited by the depth of field of the objective. In ff-OCT the sample is moved relative to the objective for z-scanning, so the scan range is only limited by the working distance of the objective and not by its NA. Higher NA can be used to increase the lateral resolution, so we chose objectives with an NA of 0.8. Even higher NAs are in principle usable, but a pair of identical objectives with larger NA and sufficiently long working distance was not available to us.

As explained in more detail below, a new problem arises with medium and high NA objective ff-OCT systems when the refractive index of the sample does not perfectly match the refractive index of the immersion medium. When imaging deeper layers, the additional optical path difference causes the coherence volume to move out of the depth of field of the objective; this defocus considerably decreases OCT signal (an effect also called "confocal effect of OCT", see Sheppard, et al., 2004) and limits imaging depth when uncorrected. To remove defocus, we implemented an automatic reference arm length scan which kept the imaging plane fixed inside the sample while moving the coherence volume. The optimal reference arm length was taken to be the one maximizing the total OCT signal.

Without defocus correction (i.e. at fixed reference arm length optimized on the cover glass), only 10% of the signal above background remains at around 120µm imaging depth (Figure 2-3, black dashed line). However, optimizing the reference arm length to compensate defocus at 200 µm imaging depth, we were able to recover signal more than twice as strong (Figure 2-3, gray solid line). Optimizing at 300 and 400 µm imaging depth (Figure 2-3, gray dashed and dotted lines), we found new optimal reference arm lengths which again boost signal strength by more than a factor of two. As expected, these reference arm lengths were only optimal in the vicinity of the depths where they were determined and cause low signal levels when used for imaging near the surface.

During the refractive index measurement we found that optimal reference arm length actually varied linearly with depth inside tissue (see chapter 1). This implied that defocus-corrected imaging at arbitrary depths could be achieved without re-optimizing defocus at every single depth. With open-loop defocus correction based on the measured defocus slope, OCT signal falls off a lot more slowly (Figure 2-3, black solid line); the 10% level is reached at about a 300µm depth, indicating a 2.5-fold increase in imaging depth compared to imaging without defocus correction.

In summary, signal level and penetration depth in ff-OCT imaging with high-NA objectives benefit greatly from defocus correction, underlining the importance of the automated correction integrated in deep-OCM.
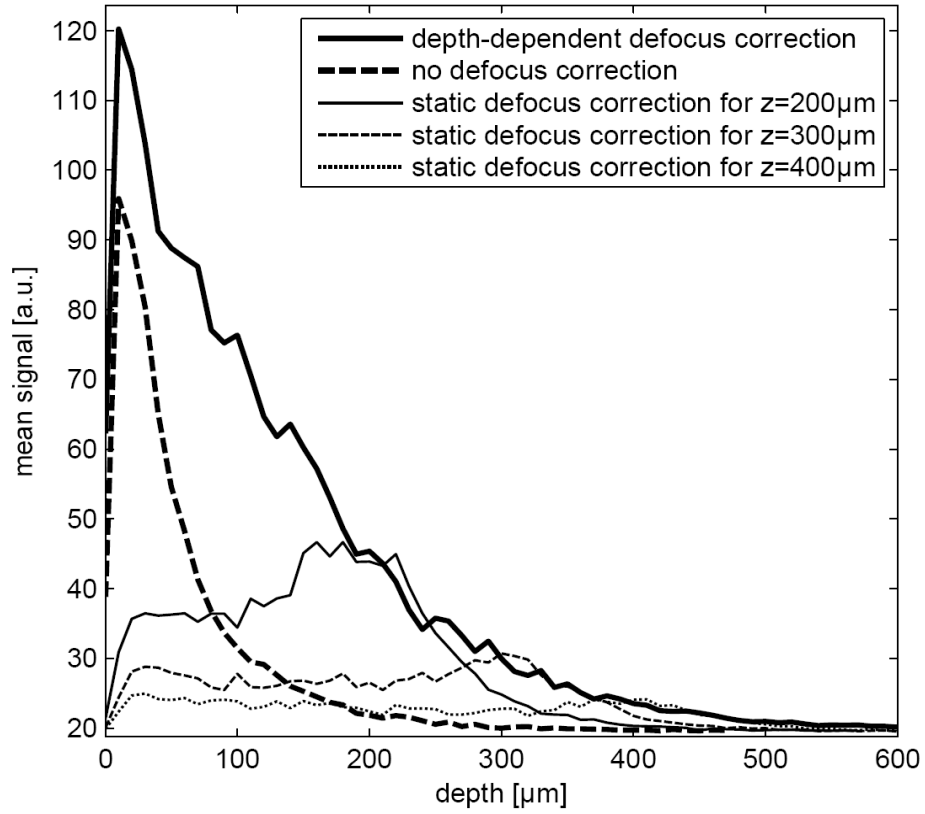
Figure 2-3. Mean OCT signal as a function of imaging depth for different reference arm configurations: no defocus correction (thick dashed curve) and fixed reference arm length optimized for imaging at depths of 200, 300 and 400 µm, respectively (thin curves) as well as depth-dependent defocus correction (deep-OCM mode; thick solid line). The sample was the upper cortical layers of a young rat, imaged in vivo with ff-OCT at 33 Hz. Each data point corresponds to the mean signal of four image frames taken at the same depth, corresponding to 120 ms acquisition time. Axial scanning was performed with a 10 µm step size.

3   Myelin imaging with deep-OCM[3]

Myelin is the electrical insulation which allows, at a given axon diameter, faster signaling in the nervous system of vertebrates. It is produced by glial cells which wrap tightly around axons of neurons in the central nervous system to use several layers of their cell membrane for insulation. Myelin also appears in the peripheral nervous system where fast signal transmission to and from the brain is important. Diseases such as leukodystrophies, multiple sclerosis, Charcot-Marie-Tooth disease and other peripheral nervous system neuropathies all involve destruction or a dysfunction of production of myelin (Baumann & Pham-Dinh, 2001; Scherer & Wrabetz, 2008). White matter in the brain consists mainly of myelinated axons, while grey matter is a mix of axons (some of which are myelinated), cell bodies, dendrites and non-neuron cells. Large-scale imaging techniques such as magnetic resonance imaging are able to visualize white matter in the living brain and track myelination patterns on a global level. However, to visualize individual myelinated axons located in grey matter or to perform detailed observations of the changes in myelination, more sensitive techniques are needed.

Coherent Anti-Stokes Raman Scattering microscopy (CARS; Cheng, et al., 2002) is able to image individual fibers (Wang, et al., 2005), even *in vivo* (Huff & Cheng, 2007; Fu, et al., 2008), but has inherently low penetration depth (Figure 3-1) since the signal is generated predominantly in the forward direction and detection happens in the backward direction. Indeed, currently reported imaging depths for myelin are on the order of 30 μm. CARS requires two pulsed laser sources and is, therefore, a relatively complicated and expensive technique.

Recently, third harmonic generation (THG) has been used for visualization of myelin as deep as 50 μm into the mouse spinal cord (Farrar, et al., 2010; Farrar, et al., 2011). This method also requires an expensive laser and operation in the cortex has not been shown.
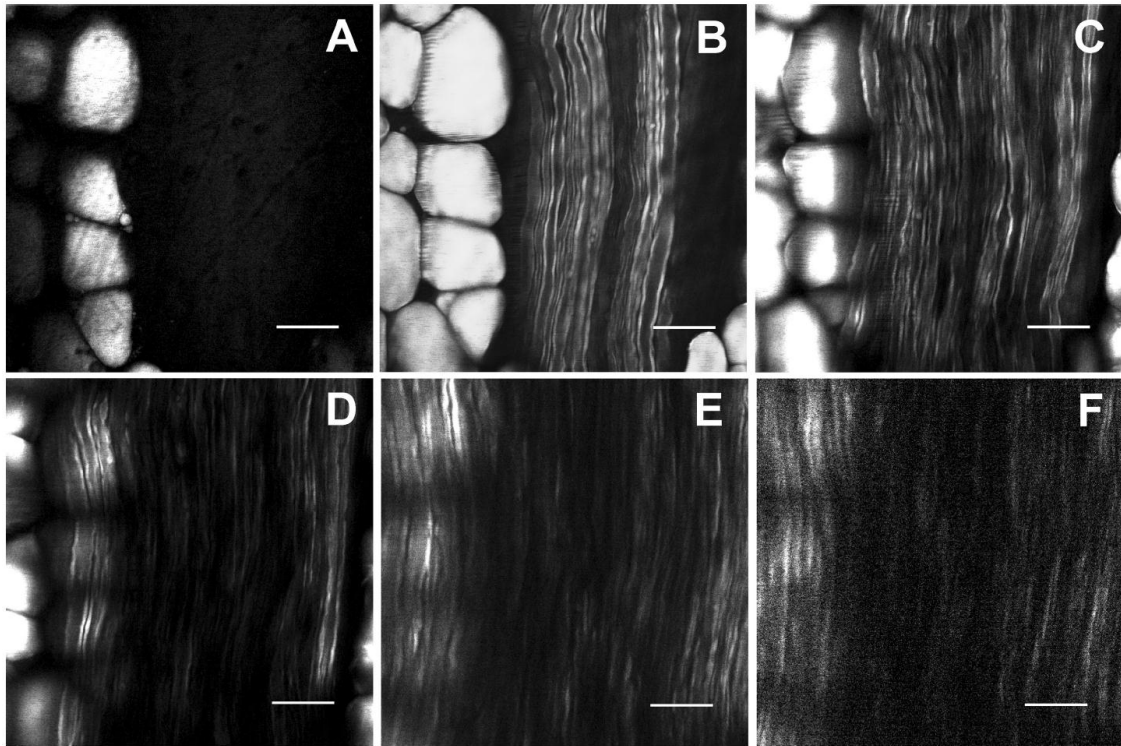
Figure 3-1. Sciatic nerve imaged using E-CARS (A) 0 µm, (B) 10 µm, (C) 20 µm, (D) 30 µm, (E) 40 µm and (F) 50 µm below the surface. Scale bar 20 µm. This figure was taken from (Huff & Cheng, 2007), reprinted by permission from John Wiley and Sons: Journal of Microscopy, copyright 2007.

In this chapter we will present our finding (Ben Arous, et al., 2011) that deep-OCM is capable of visualizing individual myelinated axons *in vivo* in depths considerably larger than currently possible with CARS or THG at a greatly reduced cost and with a much simpler experimental setup.

3.1 Deep-OCM shows myelin

Using our deep-OCM setup (Chapter 1, Figure 2-1) with automatic defocus correction for *in vivo* imaging of the rat somatosensory cortex, we found that cortical tissue generally had a relatively homogenous baseline reflectivity, which was only interrupted by three types of structures. Dark, roughly spherical regions with below-baseline reflectivity probably signify cell bodies. Blood cells in horizontally-oriented blood vessels usually reflected well (Figure 2-2), while blood vessels orthogonal to the imaging plane were usually only visible as dark circles and could be differentiated from cell bodies only by their long axial extent (when recording z stacks) and more variable diameter. The third structural element found was thin, bright fibers whose thickness was near the diffraction limit of our microscope of around 0.56

μm (Figure 3-2a). A high numerical aperture is critical for the visibility of these fibers: while they are still visible at an NA of 0.3, they cannot be discerned using ff-OCT at an NA of 0.1 (Claude Boccara and LLTech the Inc., private communication).

To confirm that these fibers corresponded to myelin, we performed several control experiments, which were coordinated by post-doc Juliette Ben Arous at ENS Paris. Using brain slices from genetically modified mice expressing enhanced green fluorescent protein (EGFP) under the cyclic nucleotide phosphodiesterase (CNP) promoter (Yuan, et al., 2002), we compared confocal fluorescence images to deep-OCM images. CNP-EGFP is expressed specifically in oligodendrocytes. In CNP-EGFP fluorescence images of the corpus callosum with a pixel size of 1.12 μm and a field of view of 594x672 μm, oligodendrocyte cell bodies and bundles of myelin fibers are visible (Figure 3-2b, left). The structures visible in deep-OCM of the same region of the sample correspond directly to the myelin fiber bundles visible in the fluorescence images (Figure 3-2b, right). Note that the cell bodies are not visible, so deep-OCM is not specific to oligodendrocytes, but to the strong local refractive index gradients of the myelin sheath, which scatter the incident light much more strongly than the surrounding tissue.

We also wanted to show that the hypothesis of deep-OCM showing myelinated fibers was consistent with the density of myelinated axons in the cortex. We therefore compared confocal images of immuno-fluorescently stained myelin basic protein (MBP) in one rat brain slice with deep-OCM images of an adjacent slice (Figure 3-3) and quantified the fiber density in both. Use of the same slice was not possible since the treatment for fluorescence staining destroyed the OCM contrast (not shown). For 12-week-old rats, sparse networks of the fibers were visible with both techniques. For three-week-old rats, deep-OCM images did not reveal any fibers. In contrast, immunofluorescence imaging showed small islands of fibers, whose average distance was larger than the field of view of the deep-OCM images. It is therefore possible that deep-OCM imaging missed these fibers due to the smaller field of view. Another reason could be that all fibrous islands originated in the depth corresponding to the slice used for immunostaining (150 μm below the surface) and none in the depth of the slice used for deep-OCM (250 μm below the surface).
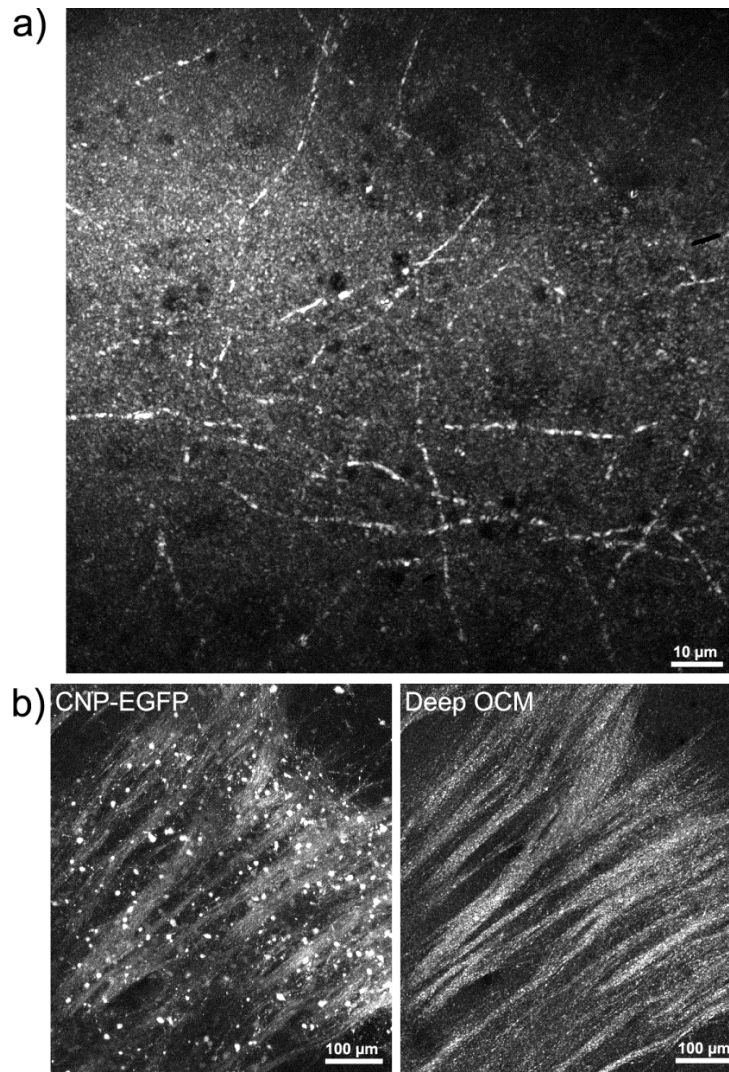
Figure 3-2. Deep-OCM myelin imaging. (a) Maximum projection of a 40× deep-red deep-OCM image stack in a cortex slice (80 images taken in 0.4μm z steps, z=250μm below the brain surface, total exposure time 84 seconds) (b) Comparison of confocal fluorescence images (left; maximum z projection of 32 images, 4 minutes 30 seconds acquisition time) and stitched 10× IR deep-OCM images (right; maximum z projection of 3x2 stitch in 100 depths i.e. 600 images, 9 minutes exposure time) of the same slice of corpus callosum of a CNP-EGFP mouse.

Quantification of the total length of all fibers per volume in both imaging modalities gave results around 4 m per cubic millimeter for the 12-week-old animals. The estimates for both techniques agreed within their error bounds, again consistent with the hypothesis that both show the same structure (Figure 3-3c).
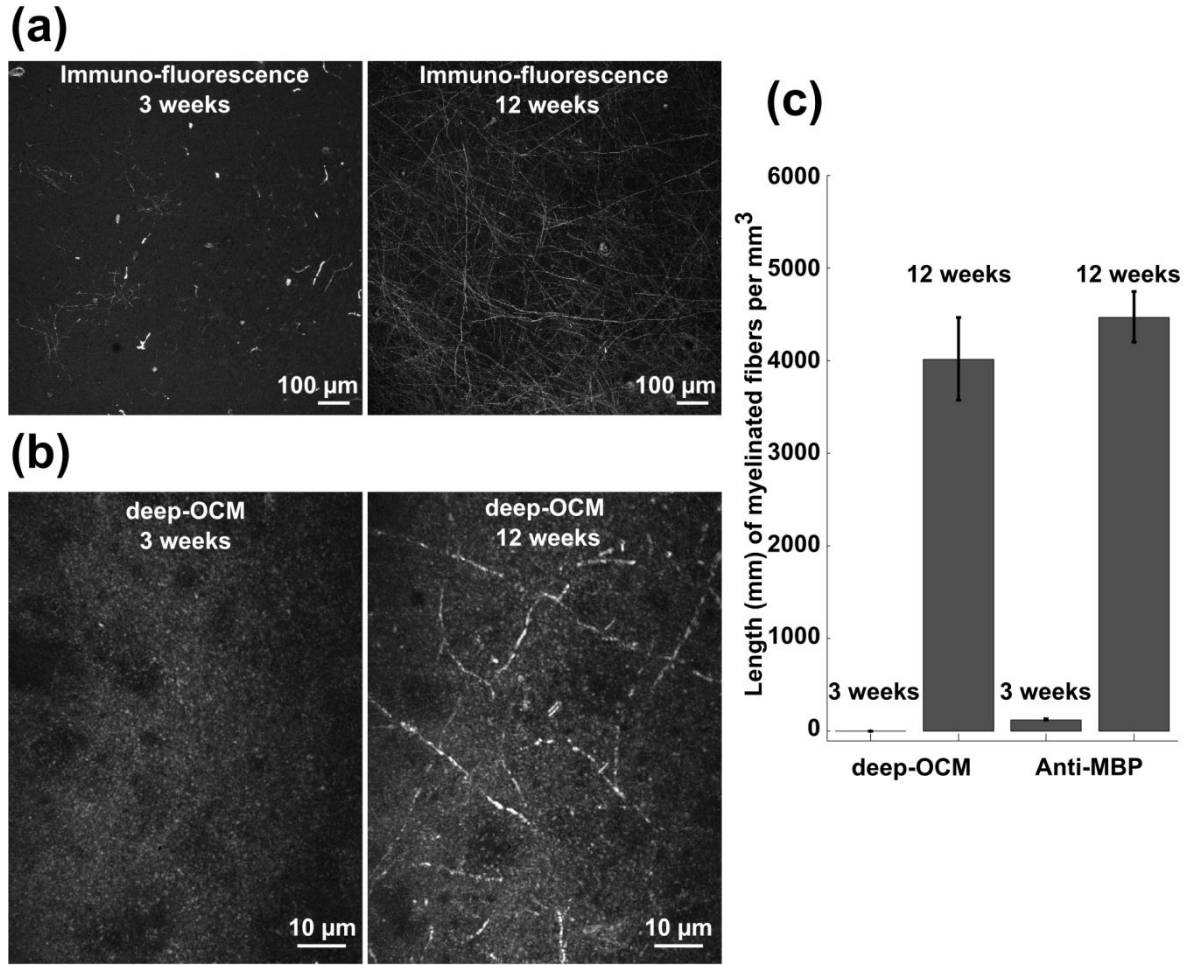
Figure 3-3. In vitro deep-OCM imaging in the rat somato-sensory cortex. (a) Maximum projection of confocal images (fluorescent anti-MBP) of tangential slices of rat somato-sensory cortex taken using 10× objective (1mm x 1mm x 60μm, z=150μm below the brain surface; 32 images, total acquisition time around 4 minutes) from a P19 and a P85 rat. (b) Maximum projections of 40× deep-red deep-OCM image stacks in adjacent cortex slices (z=250μm) from the same animals as in (a) (70μm x 90μm x 60μm; 150 images, total exposure time around 3 minutes). (c) Fiber length density measured in vitro in tangential slices of rat somato-sensory cortex, by 40× deep-red deep-OCM and by confocal immuno-fluorescence, for 3-week-old and 12-week-old animals. Error bars indicate plus or minus one standard error of the estimated mean (s.e.m.).

A third and last argument in favor of deep-OCM showing myelin is the localization and structure of signal in a large-field-of-view high-resolution image of the cerebellum. The prototype of a commercial full field OCT system (LLTech, France) was used to acquire 15 x 19 individual overlapping OCT images to cover the full area of the cerebellum slice, which were then stitched to form one large image (Figure 3-4a). Comparing with the low-resolution

bright field image of said slice (Figure 3-4b), deep-OCM provided strongest signal in the areas known to contain white matter, i.e. high concentrations of myelinated fibers. Looking more closely, different cell layers could be differentiated (Figure 3-4c) and even individual fibers were discernible (Figure 3-4d and Movie 3).In summary, we are convinced that the fibers visible in deep-OCM correspond to myelinated axons.
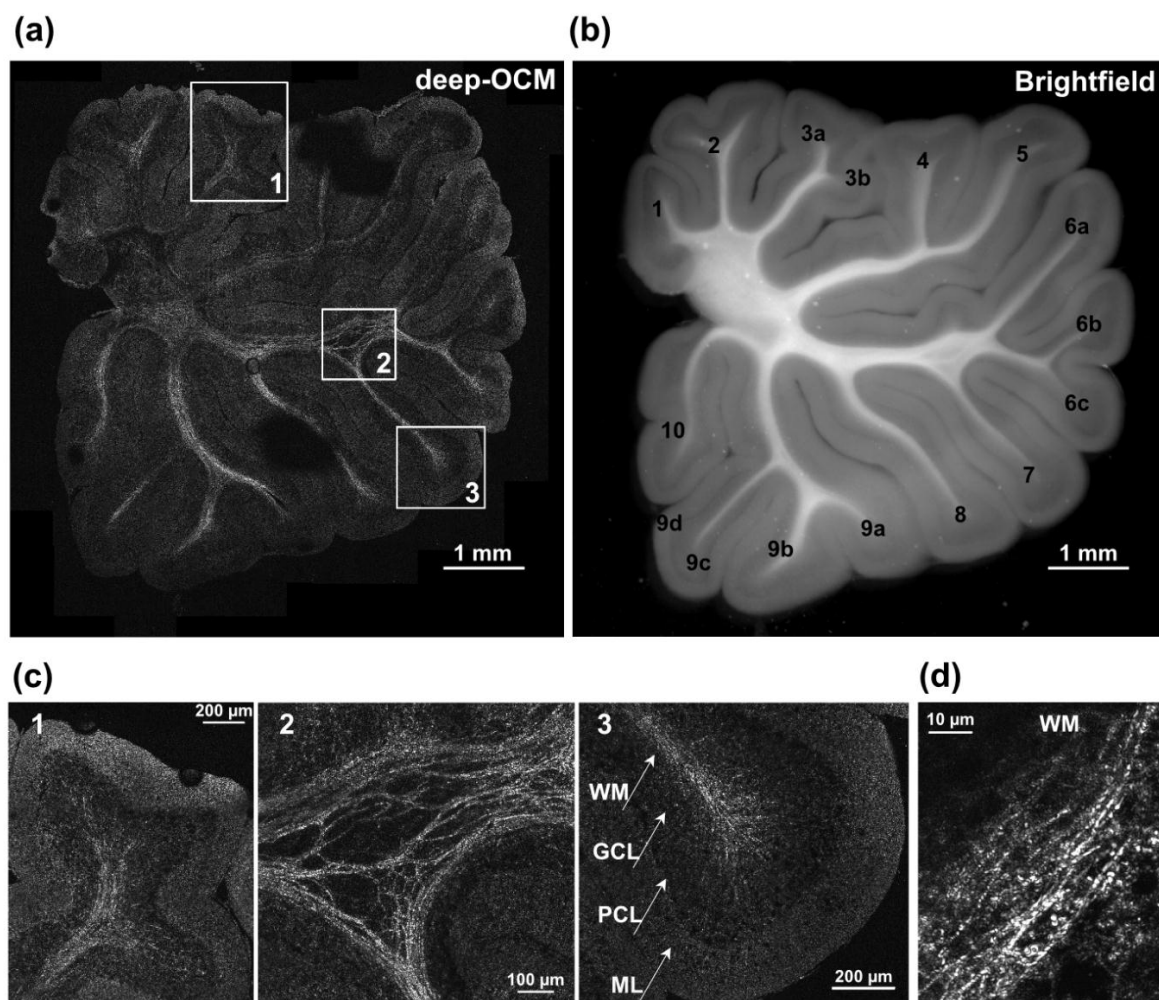
Figure 3-4. High-resolution deep-OCM imaging of rat cerebellar slices. (a) 10× IR deep-OCM image of a fixed sagittal slice of a 3-week-old rat; stitch of 15x19=285 images, total exposure time 11 minutes 24 seconds. (b) Bright field low-resolution image with indication of the different cerebellar lobules. (c) Detail of the 3 regions delimited in (a). WM: white matter; GCL: granule cell layer; PCL: Purkinje cell layer; ML: molecular layer. (d) 40× deep-red deep-OCM image of cerebellar white matter (maximum z projection over 6 images taken in 1 μm steps, total exposure time 6.3 seconds, corresponding to part of the volume shown in Movie 3).

3.1.1 Sensitivity to fiber orientation

Due to the en face imaging mode of full field OCT, fibers oriented parallel to the imaging plane are much more easily spotted. Slightly tilted fibers can be traced through sufficiently fine z-stacks, but strongly tilted fibers are difficult to identify due to the speckled nature of OCT images. A second problem which might render strongly tilted fibers less visible is the directionality of their light scattering. Presumably, the strong scattering everywhere along their length causes them to act like one-dimensional "mirrors", which emit the light from each incoming ray into a cone with an opening half-angle equal to the angle between the incoming ray and the fiber. Only when the fiber is more or less orthogonal to the incident light, part of this cone falls into the acceptance angle of the microscope objective.

3.2 Imaging myelin fibers *in vivo* in cortex

Myelin imaging using deep-OCM was not only possible in slices, but also *in vivo* in the rat cortex. By visual inspection of several image stacks from different animals, we found that fibers had their highest concentration in depths of up to 150 µm, consistent with previous studies found on http://brainmaps.org/ajax-viewer.php?datid=148&sname=07 (Mikula, et al., 2007; Trotts, et al., 2007).

Since fiber density was depth dependent, we took the maximum image intensity per slice as a measure of signal decrease with depth. To reduce the influence of individual pixels, spatial filtering with a Gaussian kernel the size of the diffraction limited PSF was performed before taking the maximum. The signal level reached the constant noise level at a depth of 400 µm (Figure 3-5b), consistent with the visual finding of individual fibers down to 340 µm (Figure 3-5a).
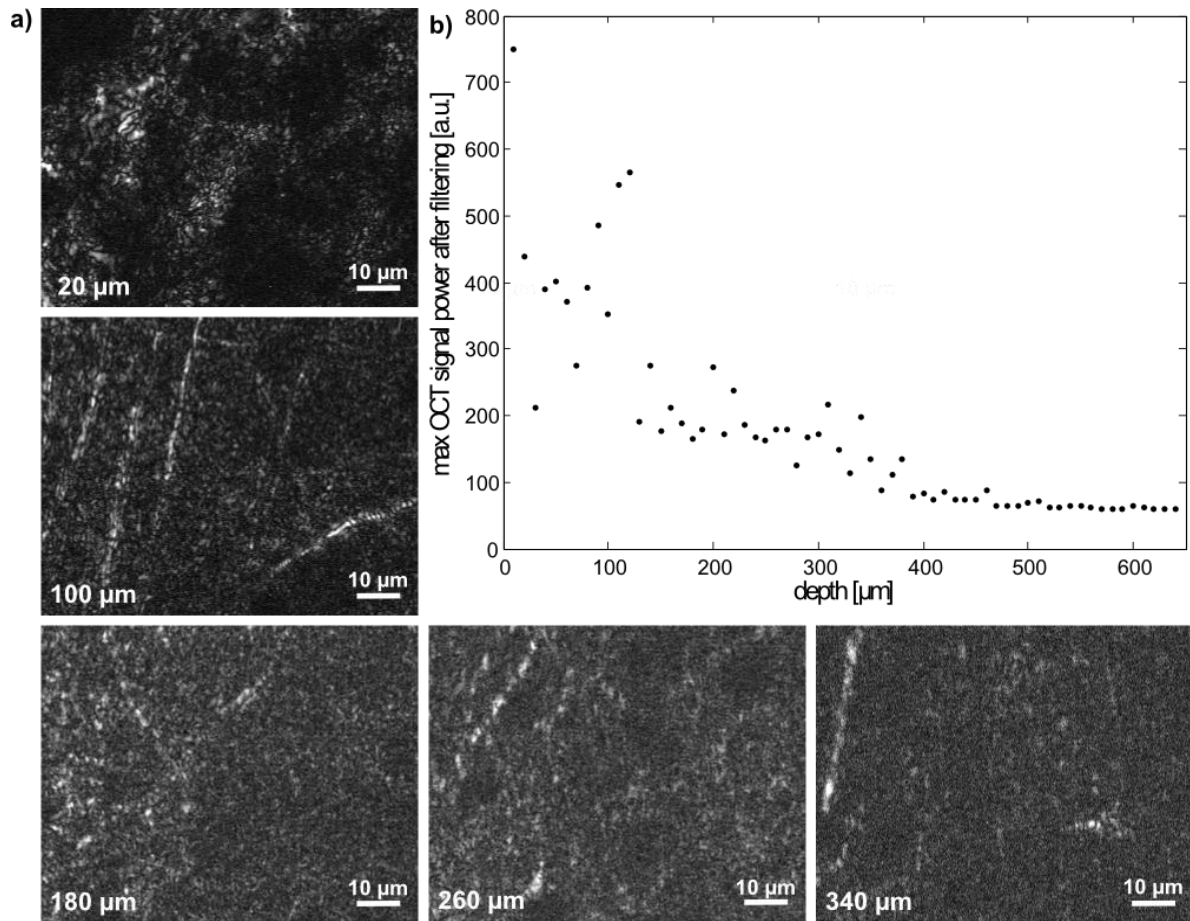
Figure 3-5. In vivo deep-OCM myelin imaging in the rat somato-sensory cortex. (a) Normalized in vivo 40× IR deep-OCM images of the somato-sensory cortex of a 12-week-old rat, with the dura removed, at different depths (20μm, 100μm, 180μm, 260μm and 340μm); exposure time per depth was 120 milliseconds. b) z-profile of the maximum intensity of the stack (65 images, total exposure time 7.8 seconds) from which the images shown in a) were selected.

We performed deep-OCM imaging on rats of three different ages: three weeks, six weeks and 12 weeks old. While blood vessels and the below-baseline-intensity structures mentioned above were visible in animals of all ages, fibrous structures were only found in rats at least six weeks old (Figure 3-6). This is consistent with our own in vitro experiment (Figure 3-3) and with the fact that most of the myelin in the rat cortex develops postnatally.
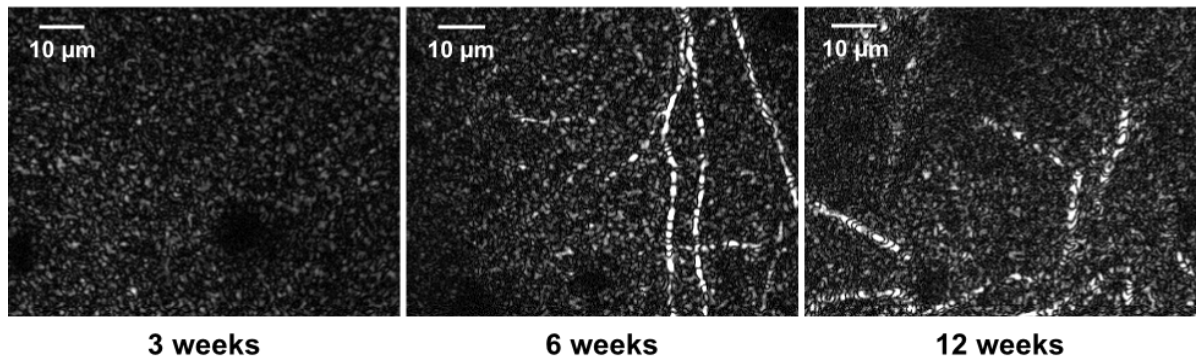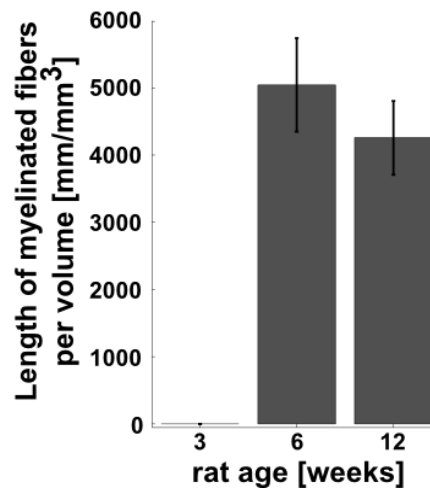
Figure 3-6. Developmental profile of myelinated fibers in the cortex. (a) In vivo 40× IR deep-OCM images of the somato-sensory cortex of 3-week-old (left, z=120μm), 6-week-old (middle, z=120μm) and 12-week-old (right, z=150μm) rats (dura mater was removed in all three cases; no averaging, i.e. 30ms exposure time each). (b) Developmental profile of the fiber length density in the cortex. Error bars indicate plus or minus one standard error of the estimated mean.

3.3 Myelin imaging in the peripheral nervous system

To investigate the applicability of deep-OCM for diagnostic purposes of degenerative diseases of the PNS, we imaged excised sciatic nerves from two mice: a wild type mouse with intact myelination patterns and a Krox20 mutant mouse (Topilko, et al., 1994; Coulpier, et al., 2010) where myelin formation is severely hindered. Using the same microscope described above, we were able to image several tens of micrometers into the sciatic nerve of the wild type mouse, visualizing individual fibers (Figure 3-7 and Movie 4).

(a)

(b)
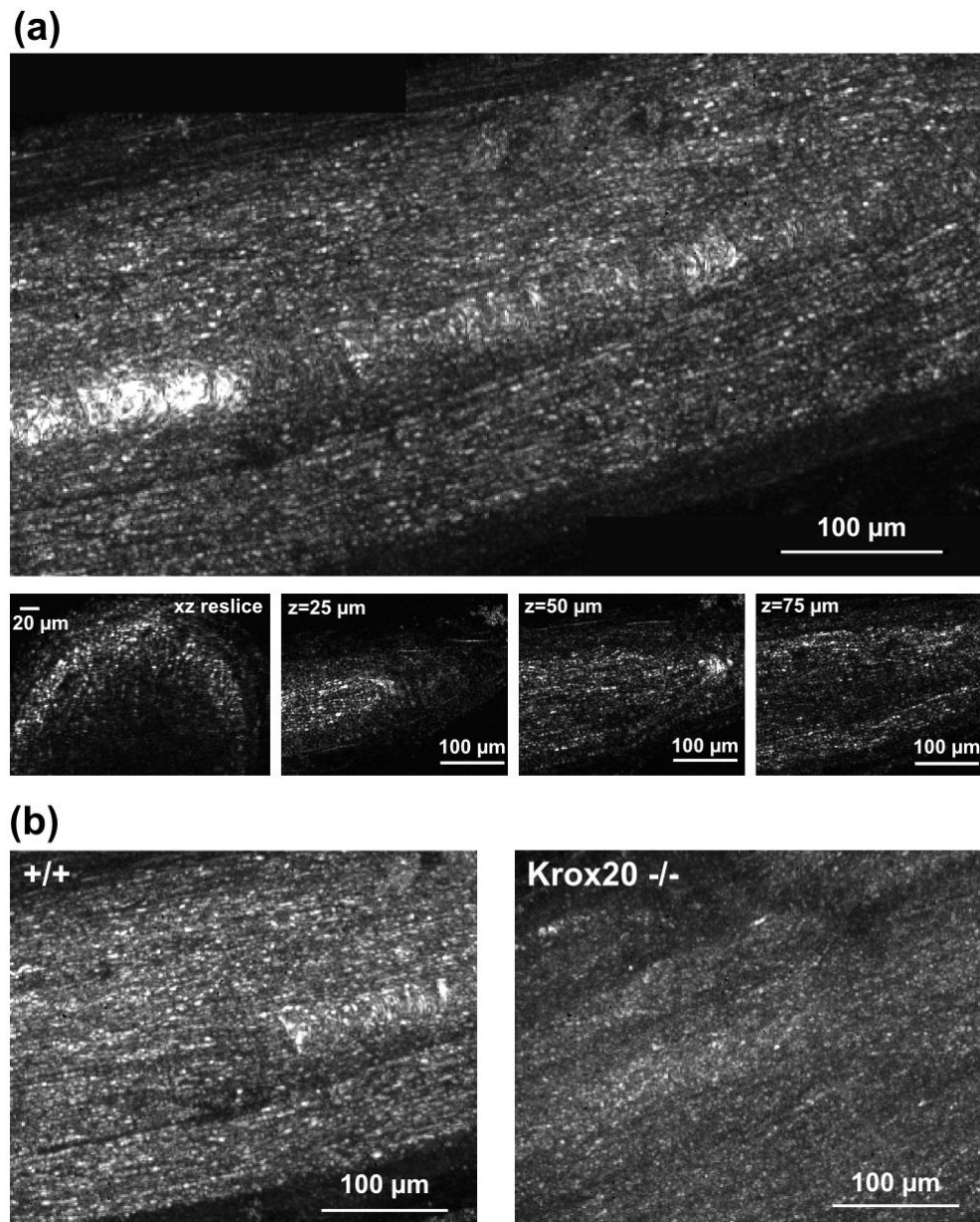
Figure 3-7. In vitro mouse sciatic nerve imaging. (a) $10\times$ IR deep-OCM image of an acute mouse sciatic nerve. Stitch of the maximum projections of two vertical stacks (2x200 images taken in 1μm steps, total exposure time 6 minutes); the bright zone on the left corresponds to a strong reflection on the upper surface of the nerve. Inserts from left to right: x-z reslice of the stack, individual images 25 μm, 50μm and 75μm deep into the nerve. (b) Comparison of a wild type mouse nerve (left) and a Krox20 -/- mutant nerve (right). In both cases, maximum projection of a vertical stack of $10\times$ IR deep-OCM images (500 images taken in 0.4μm steps, total exposure time 15 minutes).

In contrast to the wild type mouse's nerve, the excised nerve of a Krox20 -/- mouse produced much lower signal in deep-OCM imaging and mostly lacked the fibrous structure present in the wild type (Figure 3-7).

Finally, we imaged the sciatic nerve of a wild type mouse *in vivo* using minimal surgery. While the acquisition of a whole z stack was hindered by insufficient stabilization of the nerve, two-dimensional deep-OCM images (Figure 3-8) were of comparable quality to those of the excised sciatic nerve (Figure 3-7a, third inset).
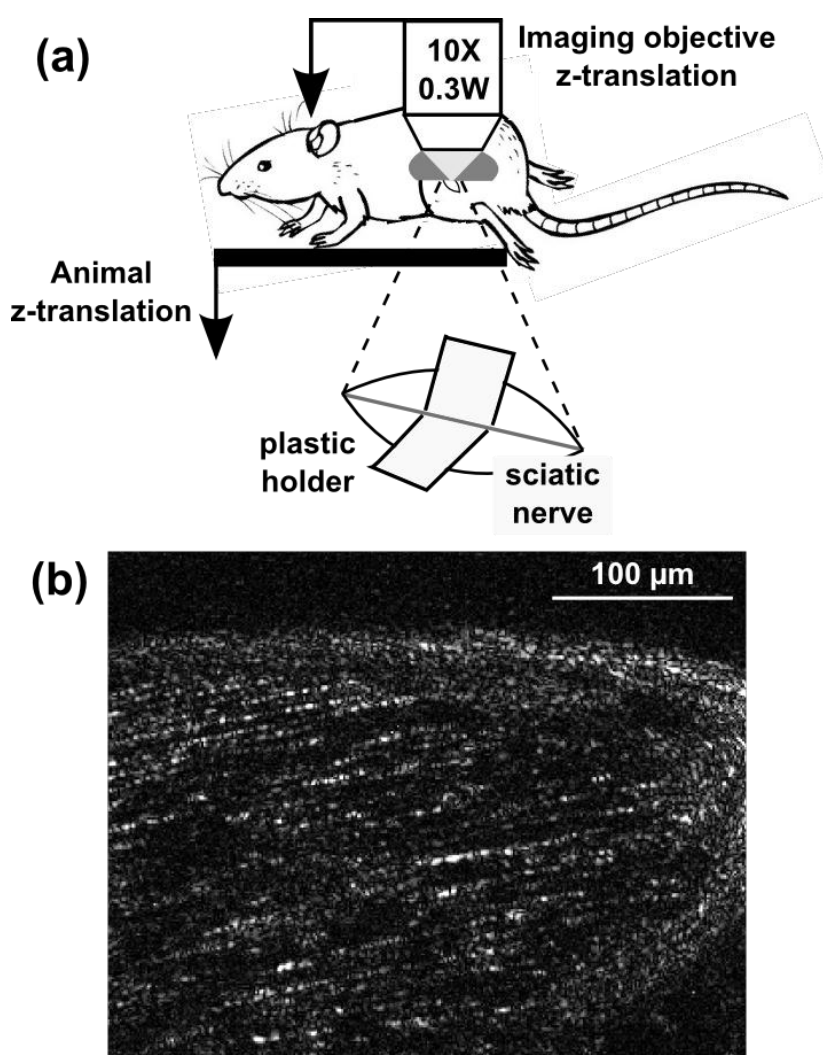
Figure 3-8. (a) Animal preparation for in vivo deep-OCM imaging in the mouse sciatic nerve. (b) In vivo image of the sciatic nerve of a wild type mouse (z=50μm below the surface; no averaging – exposure time 30 milliseconds).

3.4 Discussion

In this chapter, we have shown that deep-OCM imaging of the unstained rat and mouse nervous systems reveals high-signal fiber-like structures. Through localization and density comparison, these fibers have been linked to both genetically labeled oligodendrocytes and immunohistochemically labeled MBP, proving that deep-OCM principally visualizes myelinated structures.

This should come as no surprise, since myelin is the principal constituent of white matter which derives its name from its high scattering coefficient, and OCM and OCT detect backscattered light.

Deep-OCM will certainly be less specific for myelin than genetic or antibody-fluorescence-staining-based methods. However, the ability to assess the state of myelin both in the peripheral nervous system and in the cortex using only mildly invasive techniques and without the need for any staining will likely be a strong advantage for studying and diagnosing autoimmune diseases. In particular, it can be an important tool for correlative studies where a genetically modified fluorescent mouse can be used in a combined OCT-confocal or OCT-2P microscope to correlate the distributions of the genetically fluorescence-marked target with the distribution of the myelin. This avoids the need for doubly fluorescence-marked mice for this type of correlative study.

For fundamental research, *in vivo* myelin imaging with a resolution of individual fibers opens up the possibility to perform larger-scale studies with lab animals due to the time saved by obviating the need for staining protocols which can often take several days to carry out. Secondly, the preparation method used for imaging cortical myelin fibers through a craniotomy in the skull seems to be a good candidate for combination with implementation of a chronic imaging window[4]. This would allow the same animals to be used in longitudinal studies, visualizing either the increase in myelination during development, or the de- and re-myelination processes associated with the models for certain neuropathies. Current research in this area, particularly when concerned with the sparse myelin fiber system in the cortex, is

---

[4] A new Ph.D. student will be employed at ENS to work on this project.

severely hampered by the need to sacrifice animals at different ages and to perform post-mortem imagery on brain slices in order to build up a temporal profile. Deep-OCM could possibly provide an inexpensive and simple imaging modality for this line of research. In particular, the progression of multiple sclerosis might be more quickly observable on the level of individual fibers than on a global level.

A recent study, submitted only three weeks after the publication of the results presented in this chapter, demonstrates myelin imaging using a Fourier domain OCM microscope with a center wavelength of 1310 nm and a 170 nm spectrum, reaching imaging depths of up to 1.3 mm (Srinivasan, et al., 2012).

4 Rat brain refractive index[5]

4.1 Introduction

As discussed in the general introduction, microscope objectives in light microscopy are only available for a limited number of refractive indices. Imaging into a sample with refractive index for which the objective was not designed produces optical aberrations, which become more severe as the refractive index mismatch and/or the imaging depth increase (Hell, et al., 1993; Török, et al., 1995). Consequently, it is important to know the precise refractive index of a sample to determine in which depth aberrations will become a problem.

The refractive index of brain tissue has previously been measured in vitro (Table 4-1), but no precise *in vivo* measurement was found in the literature. Both fixed tissue and acute slices are expected to have modified optical properties due to changes in the mechanical and chemical environments compared to *in vivo* tissue, and are therefore not optimal for measuring the refractive index.

In this chapter, *in vivo* refractive index measurements of the rat somatosensory cortex using defocus optimization (Tearney, et al., 1995; Labiau, et al., 2009) in full-field optical coherence tomography (Dubois, et al., 2002; Vabre, et al., 2002) are presented. As one of the rare epi-configuration microscopy systems which is sensitive to defocus, OCT is perfectly suited for refractive index measurements in the living cortex, where a transmission measurement is not possible.

---

[5] Large parts of this chapter are based directly on the text and figures of BINDING, J., BEN AROUS, J., LÉGER, J.-F., GIGAN, S., BOCCARA, C. & BOURDIEU, L. (2011). Brain refractive index measured in vivo with high-NA defocus-corrected full-field OCT and consequences for two-photon microscopy. Opt. Express **19**(6), 4833-4847.

Table 4-1

Sample	Refractive index n'	Measurement Wavelength [nm]	Source
Human brain, gray matter	1.36 ±0.02 (std. dev.)	456/514/630/675/1064	(Gottschalk, 1993)
Rabbit brain, gray matter	1.36 ±0.02 (std. dev.)	456/514/630/675/1064	(Gottschalk, 1993)
Rat cortex, fresh 400μm slice	1.37	Unspecified; probably 830 nm or 1280 nm	(Roper, et al., 1998)
Cell body of mouse cortical neurons in culture (two individual cells)	1.3751 ±0.0003 1.3847 ±0.0003	658 nm	(Rappaz, et al., 2005)
Mouse brain slice (5μm, fixed)	1.368 ±0.007	633 nm	(Lue, et al., 2007)

4.2 Measuring refractive index using high-NA OCT

4.2.1 OCT signal strength is sensitive to refractive-index-induced defocus

For the measurement of the refractive index of the sample, the sensitivity of high-NA OCT to defocus aberration was exploited (Figure 4-1). When imaging with a correctly aligned system at the surface of a biological sample, the focal plane of the microscope objective coincides with the center of the coherence volume defining the sectioning volume of the OCT system, leading to good imaging quality, limited only by diffraction and speckle (Figure 4-1a). The relative arm length δ is defined to be zero in this case. When imaging deeper into a sample with a phase refractive index n' larger than that of the immersion medium n, refraction at the surface causes the actual focus z_A of the objective to be enlarged and shifted deeper into the sample with respect to the nominal focus z_N (Figure 4-1b). At the same time, the coherence volume penetrates the tissue slower than the nominal focus due to the increased group refractive index n'_g (defined as $n'_g = c/v'_g$ with c being the vacuum speed of light and v'_g the group velocity in the sample) (Figure 4-1b). This discrepancy between the plane imaged with OCT, defined by the position of the coherence volume (CV), and the actual focus results in a reduction of interference contrast (i.e. in a loss in OCT signal). This signal loss is therefore related to the optical properties of the sample and for a proper analysis of this effect, we have to take n' and its dispersion into account and differentiate between n' and n'_g of the sample.
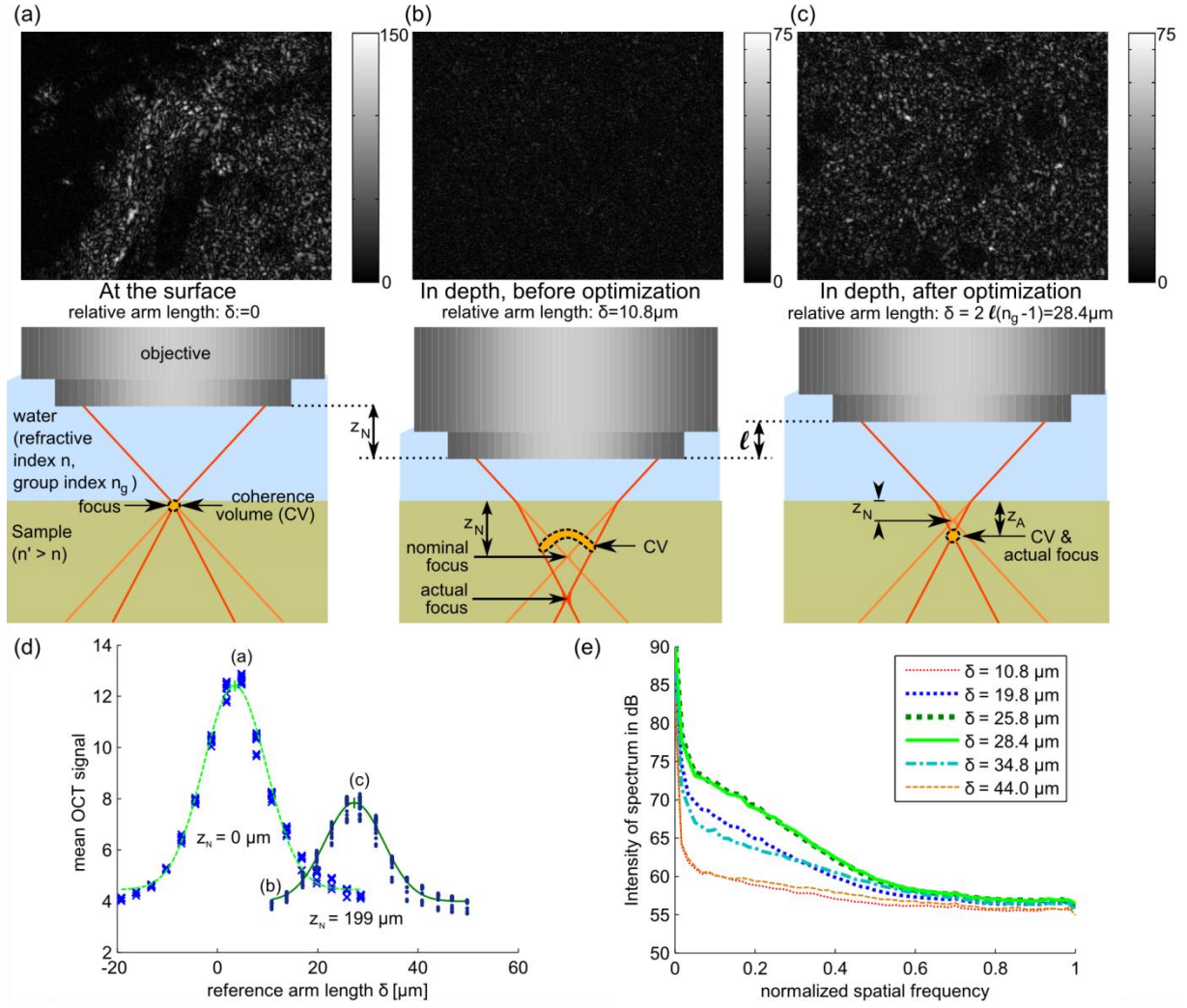
Figure 4-1. Defocus caused by refractive index mismatch in high-NA OCT imaging and defocus correction. (a) OCT image of brain surface; the coherence volume coincides with the focus of the objective. (b) Imaging at a nominal depth z_N of 205µm below the tissue surface, non-optimized relative arm length $\delta = 10.8µm$. (c) Moving the objective by a distance ℓ and simultaneously changing the reference arm length by $\delta = 2 \ell (n_g - 1)$ allows the actual focus z_A to be brought into coincidence with the coherence volume, decreasing the nominal imaging depth by ℓ to $z_N = 199µm$. (d) OCT signal vs. reference arm length δ at nominal imaging depths $z_N = 0µm$ and $z_N = 199µm$. The data points corresponding to the images shown in a-c are indicated by the corresponding letters. A Gaussian with a baseline is fitted to the data. (e) Spatial frequency content of images for different reference arm lengths δ.

To compensate for this signal loss and to maximize the OCT signal, it has been proposed to change the reference arm length to move the coherence volume into the position of the actual focus (Tearney, et al., 1995), but this maximization scheme changes the depth of the imaged

plane inside the sample. Such an optimization is, therefore, biased by the exponential signal decay with imaging depth, and by the sample structure. To avoid these sources of bias, it is preferable to keep the coherence volume at a constant depth inside the sample and move the actual focus into this same position (Labiau, et al., 2009) (Figure 4-1c). If dry objectives were being used, this could be achieved by moving only the sample objective and keeping reference arm and sample fixed. Due to the water immersion (group index n_g), a movement $\boldsymbol{\ell}$ of the sample objective away from the sample increases the (paraxial) optical path in water by $2\,n_g\,\boldsymbol{\ell}$, while the optical path in air only decreases by $2\,\boldsymbol{\ell}$. To keep the coherence volume in the same position inside the tissue, displacement $\boldsymbol{\ell}$ of the sample objective should be associated by a displacement $d(\boldsymbol{\ell})$ of the reference arm, corresponding to an increase of the reference arm length $\delta(\boldsymbol{\ell}) = 2d(\boldsymbol{\ell}) = 2\,(n_g{-}1)\,\boldsymbol{\ell}$.

In summary, a concerted movement of the sample objective by $\boldsymbol{\ell}$ and the reference arm by $d(\boldsymbol{\ell})$ leads to an optimization scheme where the imaged plane remains fixed inside the sample, while the actual focus of the objective scans through different depths. Experimentally, images were taken in successive associated positions $(\boldsymbol{\ell},\, d(\boldsymbol{\ell}))$ and an image-based metric (see below) was used to experimentally determine which positions $(\boldsymbol{\ell},\, d(\boldsymbol{\ell}))$ centered the actual focus on the coherence volume (Figure 4-1d) by fitting a Gaussian with offset to the metric values. In the following, optimal positions $(\boldsymbol{\ell},\, d(\boldsymbol{\ell}))$ will simply be referred to as the optimal reference arm position d (or optimal reference arm length $\delta = 2d$). Note that different motor placement configurations are possible for the scheme discussed here; for details, see section 9.1.

4.2.2 Dispersion and high NA complicate the refractive index measurement

From the nominal focus z_N and the optimal reference arm length δ, the refractive index n' of the sample can, in principle, be inferred. Previous calculations of the relationship between n' and δ at a given z_N have focused on paraxial or marginal ray analysis and were only used in conjunction with low NA (i.e. below 0.2). Even though some papers presented formulae differentiating between n' and n'$_g$, calculations were always performed assuming zero dispersion in all media involved (i.e. n = n_g, n' = n'$_g$). (Tearney, et al., 1995; Knuettel & Boehlau-Godau, 2000; Alexandrov, et al., 2003; Zvyagin, et al., 2003)

While these approximations greatly simplify the calculations, they are certainly inadequate for the NA 0.8 objectives used in this work. The use of high-NA objectives increases the defocus aberration and, therefore, the sensitivity to the refractive index, at the expense of a more

complicated calculation. Even monochromatically, the point of best focus in presence of a refractive index mismatch is no longer described correctly by the paraxial theory in the case of high NA objectives. Since the immersion water, which has a significant level of dispersion in the near infrared wavelength region, served as a reference medium, we felt it necessary to revisit the issue of the influence of dispersion on the refractive index determination. The experimental precision of our data goes beyond the 1-2% limit presented in previous work (Tearney, et al., 1995; Knuettel & Boehlau-Godau, 2000; Alexandrov, et al., 2003; Zvyagin, et al., 2003; Labiau, et al., 2009), which means dispersion can no longer be neglected.

In principle, the sample should be described as a volume with a certain mean refractive index n', a given amount of dispersion n'(λ) and a random homogeneous distribution of scatterers. The light of all different wavelengths and incident angles is focused by the microscope objective into this volume, where each scatterer produces secondary spherical waves whose amplitudes and phases depend on the amplitude and phase of the incoming waves at the position of the scatterer. These secondary waves will re-enter the microscope objective and ultimately be transmitted to the detector, where each wave interferes with the corresponding wave from the reference arm. The intensity measured by the detector is the absolute square of the sum of all of these waves.

Without a refractive index mismatch, a scatterer at the geometric focus will produce secondary waves which are perfectly in phase with the waves in the reference arm, independent of angle and wavelength, maximizing constructive interference. Any effect which causes a dephasing for some of the waves will decrease interference and, thereby, OCT signal.

When treating a refractive index mismatch in the paraxial approximation, the main dephasing comes from the dispersion. Since all waves travel in essentially the same direction, linear dispersion can be described by a group velocity, i.e. the medium group refractive index enters as a new independent variable (Knuettel & Boehlau-Godau, 2000). In contrast, when dispersion in both media can be neglected, the main dephasing effect comes from the fact that marginal rays travel a longer distance through the index-mismatched medium, causing their optical path length to be different from the more paraxial rays. In this case, the dephasing depends on the wave's incident and reflecting angle, which can be described by a generalized wavefront $\psi(\alpha_{in}, \alpha_{out})$ (see below).

4.2.3 Modeling the image formation process in high-NA OCT

When both NA and dispersion become important, the concept of group velocity is not helpful anymore since wave components with different wavelengths will not only propagate with different speeds, but will also be refracted by different angles. The only rigorous solution is to examine directly the total intensity I on a given pixel of the detector after integrating the amplitude of the electromagnetic field E over all possible wavelengths and incident and reflection angles and summing over both interferometer arms:

$$I = \left| E_{SMP} + E_{REF} \right|^2 = \left| E_{SMP} \right|^2 + \left| E_{REF} \right|^2 + 2\operatorname{Re}(E_{SMP}^* E_{REF})$$

Eq. 4-1

where the first two terms correspond to the incoherent background intensity from the sample and reference arms, which are essentially constant, and the third term, which can be separated out from the background by phase shifting (Malacara, 1992), is (twice) the real part of

$$E_{SMP}^* E_{REF} = \int d\lambda \int 2\pi\alpha_{in} d\alpha_{in} \int 2\pi\alpha_{out} d\alpha_{out} K(\lambda, \alpha_{in}, \alpha_{out})$$

Eq. 4-2

and is a function of sample refractive index $n'(\lambda)$ and reference arm length δ through $K(\lambda, \alpha_{in}, \alpha_{out})$. The asterisk (*) signifies complex conjugation.

In principle, for an exact expression for Eq. 4-2, one would even need to sum over all scatterers in the sample and average over all possible realizations of random scatterer configurations. However, since we are only interested in the case where the OCT signal is maximal, these summation and averaging operations can be replaced by a properly placed single scatterer. Due to symmetry it must sit on the optical axis, while its axial position z_A is optimized numerically to maximize OCT signal.
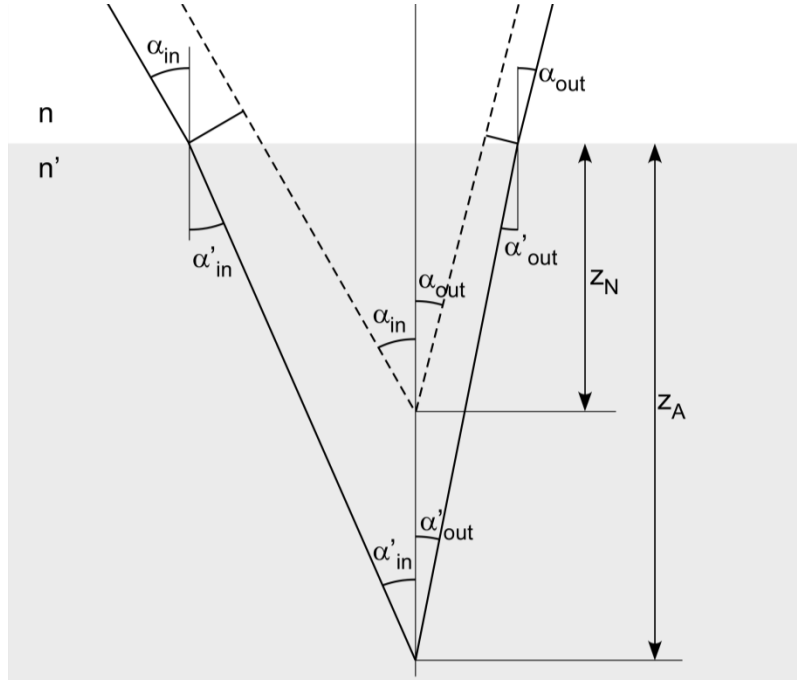
Figure 4-2. Schematic drawing showing refraction at the brain surface of light traveling to and from a single scatterer.

The term $K(\lambda,\alpha_{in},\alpha_{out})$ describes the product $E^{*}_{SMP}.E_{REF}$ for a given wavelength, incidence angle α_{in} and reflection angle α_{out} (Figure 4-2). Since phase effects will largely dominate any amplitude effects in the triple integral, we will neglect the reflectivity of the reference arm mirror, the scattering cross section and anisotropy of the scatterers as well as any amplitude effects caused by propagation. This is particularly true since we are only interested in the position of the maximum with respect to $n'(\lambda)$ and δ, not in the actual value of the integral. We are therefore left with

$$K(\lambda,\alpha_{in},\alpha_{out}) = E^{*}_{SMP}E_{REF} = e^{-i\frac{2\pi}{\lambda}[\delta_0+\Psi(\lambda,\alpha_{in},\alpha_{out})]} e^{+i\frac{2\pi}{\lambda}[\delta_0+\delta]} = e^{-i\frac{2\pi}{\lambda}[\Psi(\lambda,\alpha_{in},\alpha_{out})-\delta]}$$

Eq. 4-3

where δ_0 is the total optical path for light reflected back from the focus in one arm of the interferometer when the focus is at the sample surface and δ is the additional length added to the reference arm to maximize the OCT signal. The generalized wavefront $\psi(\lambda,\alpha_{in},\alpha_{out})$ describes the additional optical path in the sample arm due to refractive index mismatch when the nominal imaging depth inside the sample is z_N and the scatterer is in depth z_A below the

sample surface. It can be expressed as the sum of two identical terms for the incoming and scattered light paths

$$\Psi(\lambda, \alpha_{in}, \alpha_{out}) = \Psi(\lambda, \alpha_{in}) + \Psi(\lambda, \alpha_{out})$$

Eq. 4-4

where α_{in} and α_{out} are the angles of the incoming and outgoing light rays in water, measured with respect to the optical axis. Both terms can be described by (Török, et al., 1995)

$$\Psi(\lambda, \alpha) = z_N n(\lambda) \cos(\alpha) - z_A n'(\lambda) \cos(\alpha') = z_N n(\lambda) \cos(\alpha) - z_A \sqrt{n'(\lambda)^2 - n(\lambda)^2 \sin^2(\alpha)}$$

Eq. 4-5

where unprimed angles are in water and primed angles in the tissue and the second equation follows from Snell's law of refraction. Combining Eq. 4-4 with Eq. 4-5 gives

$$
\begin{aligned}
\Psi(\lambda, \alpha_{in}, \alpha_{out}) &= \Psi(\lambda, \alpha_{in}) + \Psi(\lambda, \alpha_{out}) \\
&= z_N n(\lambda) \big(\cos(\alpha_{in}) - \cos(\alpha_{out})\big) \\
&\quad - z_A \left(\sqrt{n'(\lambda)^2 - n(\lambda)^2 \sin^2(\alpha_{in})} - \sqrt{n'(\lambda)^2 - n(\lambda)^2 \sin^2(\alpha_{out})} \right)
\end{aligned}
$$

Eq. 4-6

This form of the wavefront assumes that the sample surface is flat and orthogonal to the optical axis.

4.2.4 Assuming a dispersion function allows calculation of the refractive index

For each nominal focus z_N, an optimal reference arm length $\delta = 2d$ is experimentally determined. For this pair of values (z_N, δ), we can, in principle, determine the corresponding refractive index n' from Eq. 4-2 by maximizing the integral with respect to n' and z_A. However, n' depends not directly on δ and z_N but only on their ratio δ/z_N (with an error of around 10^{-3} in the range needed here; see theory curves for n' = 1.33/1.34/… in Figure 4-3, which are virtually straight). This simplifies the analysis in that a constant slope in a z_N vs. δ plot implies a depth-independent refractive index. The value of n' can, in this case, be determined from the slope $s = \delta/z_N$ of a linear least squares fit to the data from all available depths by optimizing Eq. 4-2 at an arbitrary nominal depth, e.g. $z_N = 500$ µm, $\delta = s\, z_N$.

Since n' is a function of wavelength, an assumption about the dispersion (i.e. about the form of the function n'(λ)) needs to be made to be able to use Eq. 4-2. In contrast to the existing literature, our formalism is very flexible with respect to this assumption. While previous papers always assumed n'(λ) = const, we worked with the assumption

n'(λ) = n(λ)+Δn.

Eq. 4-7

That is to say, we consider that the dispersion of the tissue will match that of water and that the refractive index is increased by a wavelength-independent quantity Δn. If the exact refractive index n'$_0$ of the tissue at a given wavelength λ_0 were known, the OCT defocus measurement could alternatively be used to determine dispersion by setting

$$n'(\lambda) = n'_0 + (\lambda - \lambda_0)\frac{dn'}{d\lambda}$$

Eq. 4-8

and optimizing the integral in Eq. 4-2 for z_A and $\frac{dn'}{d\lambda}$.

4.2.5 Choosing a suitable metric increases penetration depth

The optimal position where coherence volume and actual focus coincide can be determined by using one of several image-based metrics in ff-OCT. While Tearney, Brezinski et al. (1995) used total signal intensity as a metric, Labiau, David et al. (2009) applied the optimization of low spatial frequency content of normalized images as proposed by Debarre, Booth et al. (2007) to ff-OCT. The latter method is useful in systems where aberrations degrade image quality without affecting signal strength, or when the sensitivity range of the metric needs to be tuned to a certain scale of aberrations. While the low and medium spatial frequency content of the images is sensitive to aberrations (Figure 4-1e), we found that optimization of total OCT signal had superior signal to noise ratio. The refractive index values calculated with both metrics agreed within the measurement error (data not shown). Therefore, we used total intensity as the metric best suited for high-NA OCT defocus optimization, which also simplified the theoretical analysis presented above.

The intensity metric was usable even at depths where no structure could be discerned in the images and where, in consequence, spatial frequency content-based metrics failed to find an optimum (data not shown). While imaging is not possible at such depths, the defocus value found can still be used to determine the refractive index. It is likely that at these depths the image is blurred by the presence of multiply scattered photons. In this case one can expect that the ballistic part of the signal can be maximized while the multiply-scattered one is insensitive to focusing.

4.3 Results

4.3.1 Rat brain refractive index as a function of rat age

To calculate the mean refractive index of the tissue, reference arm optimizations were performed at different nominal depths in 19 different lateral positions (fields of view) in the somatosensory cortex of 7 rats. Between two successive optimizations at different depths, an optimization at a fixed reference depth just below the tissue surface was performed. This allowed us to compensate for drifts (probably caused by temperature changes), which resulted in a change of optimal reference arm length.

In order to determine if the refractive index of the brain depends on the age of the animal, we used animals of different ages (3, 6 and 12 weeks old). In 3 weeks old rats, depths up to 900 µm were accessible to refractive index measurements, while older animals allowed measurements only up to 600 µm deep.

In order to calculate the refractive index of the rat brain, the optimal reference arm length δ for different nominal depths z_N below the reference depth was plotted (Figure 4-3). The optimal reference arm length δ changed linearly with depth z_N in all animals and lateral positions. One consequence of this good linearity is that the refractive index of the tissue is the same at different depths below the surface. An abrupt change of the refractive index would be indicated by a kink in the curves.
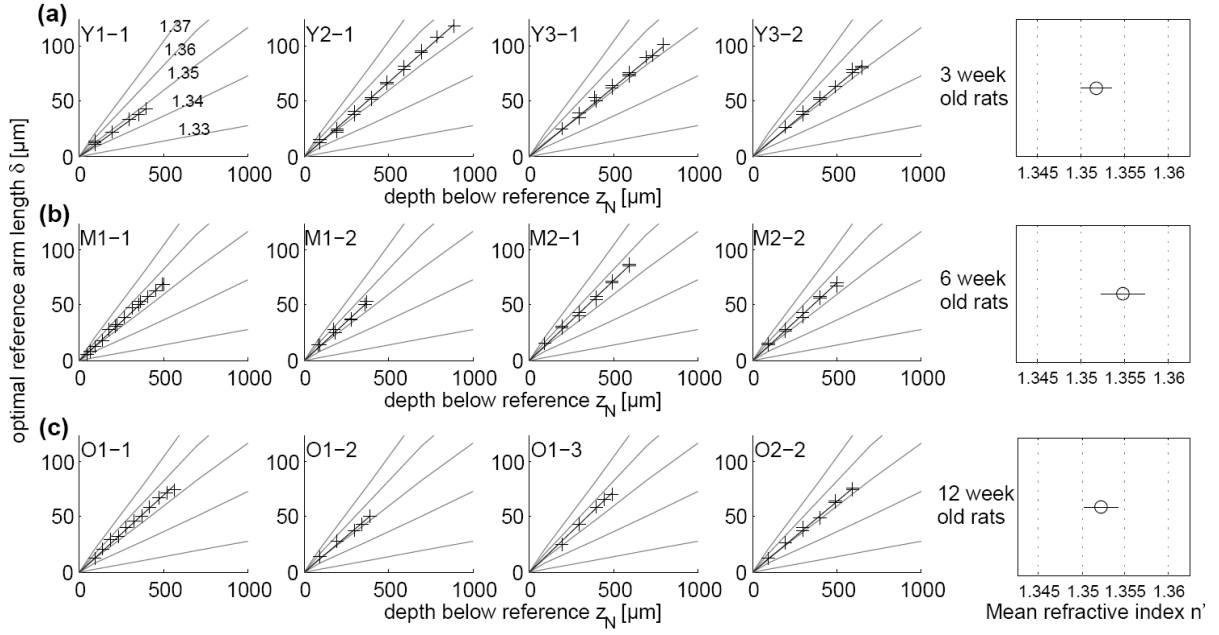
Figure 4-3. For three 3-week-old (a), two 6-week-old (b) and two 12-week-old (c) rats, the optimal reference arm length δ (see Figure 4-1d) is plotted as a function of nominal imaging depth z_N. Each plot corresponds to one lateral position in one rat, e.g. plot "M1-2" corresponds to the second lateral position in the first 6-week-old rat. For reference, the theoretical curves corresponding to fixed refractive index values from 1.33 to 1.37 are shown in all plots; the values are given in the upper left hand plot. From each plot, the mean slope δ/z_N was determined by least squares fitting and the refractive index n' was calculated. All values for different positions in animals of the same age were averaged to give the mean refractive index for animals of that age, shown in the right panel.

A depth-averaged value for the refractive index was then calculated for each field of view in each rat from the slope of the plots in Figure 4-3. A one-way ANOVA was performed to compare the groups of rats of different ages (3-week-old vs. 6-week-old vs. 12-week-old animals). It showed no significant correlation between the age of the animal and the refractive index of the cortex (Figure 4-3). The uncertainty of the depth-averaged refractive index measurements was generally smaller than the lateral variations from one field of view to another, which were, in turn, comparable to differences between animals.

Finally, we computed the mean refractive index over all positions and all rats of all ages, which was found to be n' = 1.3526 ± 0.0029 (std.dev.), ± 0.0007 (s.e.m.) for the wavelength range λ = 1.1 ± 0.1 μm. It is important to note that the refractive index of water varies from n = 1.3222 to n = 1.3252 in this wavelength range (Daimon & Masumura, 2007). To make this

easy to remember, the speed of light is roughly 2% lower in the rat cortex than in purified water.

4.3.2 Importance of dispersion and high NA

Our result for n' depends on the assumption that the dispersion in tissue equals the known dispersion of water. If we had neglected dispersion of both water and tissue, as has been done in previous work (Tearney, et al., 1995; Knuettel & Boehlau-Godau, 2000; Alexandrov, et al., 2003; Zvyagin, et al., 2003; Labiau, et al., 2009), while still taking into account the NA (i.e. removed the integration over λ from Eq. 4-2 and worked with fixed water refractive index n = 1.3237 corresponding to the center wavelength) our n' estimate would have been 0.0058 lower (underestimating the refractive index mismatch between tissue and water by 20%).

If, as well as neglecting dispersion, a paraxial approximation had been used (Labiau, et al., 2009), the refractive index would have been systematically overestimated by 0.0031 compared to our result, implying that the effect of dispersion and NA go in opposite directions in our case, with the effect of the NA being stronger.

Comparison with marginal ray calculation

The marginal ray calculation performed by Tearney et al. (Tearney, et al., 1995) assumes that the OCT signal is dominated by the light traveling at the highest angle. However, due to the coherent summation, it is rather the contribution from the area or areas of stationary phase that will dominate the integral in Eq. 4-2. Furthermore, their calculation assumes z_A to be fixed in relation to z_N based on the refraction of marginal rays; this need not necessarily be the case.

In their experiments, the low NA (0.175) used implied a deviation from paraxial theory of only 0.5%, well below their experimental uncertainty. Had their formula been applied at the NA of 0.8 used in this work, it would have caused a significant systematic error.

Generalizing their formula (2) to the case with water immersion

$$n'_{marginal}\sin\left\{\arctan\left[\frac{n'_{marginal}z_N\tan\left(\arcsin\frac{NA}{n}\right)}{nz_N+\delta/2}\right]\right\}=NA$$

Eq. 4-9

we can calculate a "marginal ray refractive index". For our mean defocus slope $\delta/z_N=0.064886$, this would lead to n'=1.3486, which is an underestimation by 0.004 or almost six times the s.e.m. compared to the value found with our model.

4.4 Discussion

4.4.1 A model of defocus in OCT taking high NA and dispersion into account

A high-precision refractive index measurement was achieved using large-NA objectives, which enhanced the sensitivity of the setup to small refractive index mismatches. In order to correctly analyze the data, both dispersion and NA must be taken into account, which our model does.

It was shown that the choice of assumptions about dispersion is important when the third and fourth digits after the decimal point of the refractive index are to be determined correctly. Paraxial or marginal ray approximations are equally invalid at a NA of 0.8, justifying the use of a new model adapted to high-NA objectives and to broadband light sources.

4.4.2 Value and (non-)dependence of brain refractive index

Using our model, we have obtained a very accurate estimate of the phase refractive index of the rat brain cortex n' = 1.3526 ± 0.0029 (std.dev.), ± 0.0007 (s.e.m.) for the wavelength range $\lambda = 1.1 \pm 0.1$ μm. This value sets a lower bound for aberrations encountered in biological tissues. Independently of the absolute value, the lack of refractive index variation with age seems surprising. Apparently structural changes during development such as vascularization and myelination of axonal fibers are not reflected in systematic changes of the refractive index in this age range. Others have found a change in the scattering mean free path with age (Oheim, et al., 2001) which implies an increase in local refractive index inhomogeneities. Since we do not see a change in the average index, these inhomogeneities might affect only a

volumetric fraction too small to be detectable with our method. The age-dependent myelin insulation comes to mind, which creates strong scattering on the few fibers found in grey matter, and is therefore a possible cause for the change in mean free path (Srinivasan, et al., 2012).

Apart from the age independence, the lack of variation with depth inside the cortex is peculiar, given the lateral and inter-animal variability (±0.0029, see results). In particular, there seemed to be no difference in the refractive index of different cortical layers. It should be kept in mind that our spatial resolution for the refractive index measurement is determined laterally by the field of view of the microscope and the opening angle of the objective, while the axial sampling is determined by the distance between two measuring depths (usually 100µm). It could be that our measurements are not sufficiently spatially resolved to show existing changes with depth. On the other hand, the lateral variations of the refractive index imply that a beam focused at some depth will encounter different refractive indices at different positions on the surface where it penetrates. This implies that other aberration modes such as astigmatism and coma will also play a role.

In two of the 3-week-old rats, refractive index measurements were possible in depths considerably greater than in the older animals. It is unclear whether this is purely due to inter-individual and inter-positional variations or whether it is caused by increased scattering in the older animals (Oheim, et al., 2001), without at the same time affecting the refractive index.

In general, the refractive index measured here of 1.3526 ± 0.0007 (s.e.m.) was lower than most values found in the literature (Table 4-1). None of these values were measured *in vivo*, so it is possible that preparation issues such as loss of water or tissue degradation could have influenced these results. For example, slices of defined thickness were obtained using cryotomes (i.e. freezing the tissue) in some studies (Gottschalk, 1993; Lue, et al., 2007) and sometimes the tissue was slightly compressed to obtain a flat surface (Gottschalk, 1993). The cell bodies of neurons in culture are not necessarily a good comparison for the average refractive index of *in vivo* brain tissue. One other reason for the discrepancy could be that our measurements were performed in the near infrared. Near infrared was chosen for improved ff-OCT and 2PLSM penetration depth (Sacchet, et al., 2008; Kobat, et al., 2009). At $\lambda=1.1\mu m$, the refractive index of water (at 24°C) is already down to 1.3237 from the commonly cited value of 1.33 (which is valid around $\lambda=700nm$), and since tissue consists mainly of water, its index will more or less follow this trend. From the dispersion of water (Daimon & Masumura,

2007) and human skin dermis (Ding & et al., 2006), we estimate the refractive index of the brain at $\lambda=1.1\mu m$ to be about 0.007 to 0.01 lower than at $\lambda=0.65$ μm. Therefore, our measurement is on the lower bound of the published data, even considering dispersion. The variations of the refractive index from field of view to field of view, which were of the order of the inter-animal variations shows that a very accurate estimate of the refractive index requires its *in situ* measurement, which is now made possible by our *in vivo* approach.

4.4.3 Limits to the measuring precision

The precision of the refractive index measurement is limited by the determination of the optimal reference arm length for a given imaging depth. Increasing the numerical aperture from 0.8 towards the theoretical limit of 1.33 could help narrow the optimization curves.

A second problem for the precision is the mechanical drift in the microscope. Since both arms of the interferometer had a length of approximately 15 cm and the mechanical levers due to the mounting of the sample on a motorized stage had a length of up to 40 cm, mechanical drifts on the order of a few micrometers per hour were unavoidable. Even though we compensated for this by taking a reference measurement of optimal arm length at the sample surface after each in-depth optimization of reference arm length, nonlinearities in this drift could still have a small effect.

4.4.4 Potential systematic errors

There are several potential sources of systematic error that could affect our refractive index measurement. The most notable source is probably the assumption that has to be made about the dispersion in the brain tissue. If it turns out to be larger than dispersion in water, its effect will bias our estimate for the mean refractive index. A second problem can in principle be caused by the absolute scaling of the linear movement performed by the two motorized stages under the objective and under the sample. However, since only the ratio of these movements enters our calculation and two identical motors were used, it is unlikely that the motor scaling had any notable effect.

4.4.5 Comparison with recent measurements

Using acute rat brain tissue slices, it was recently shown that the refractive index changes non-linearly with tissue compression (Sun, et al., 2012). The absolute value found in that study was slightly larger than our value. This could either indicate that in our experiments the

refractive index was reduced due to tissue swelling, or alternatively that the preparation of their acute slices caused an artificial increase.

In a second study, a slight hint for a change in refractive index between different cortical layers was found, but it was not statistically significant (Srinivasan, et al., 2012). For the different layers they determined values between n=1.345 and n=1.355 at a center wavelength of 1310 nm, which is in very good agreement with our own results.

5 Consequences of brain refractive index mismatch for two-photon microscopy[6]

Due to the refractive index mismatch between the immersion water and the brain, paraxial rays have a shorter path to focus than marginal rays, leading to an aberrated (enlarged) point spread function. Since two-photon excitation efficiency depends quadratically on the local light intensity, the aberrations lead to signal loss, which can be quantified by describing the aberrations as a phase function (wavefront) in the objective pupil and then calculating the focal intensity distribution (Egner & Hell, 1999).

Using the measured value for the refractive index, we estimated the loss in resolution and signal in 2PLSM. We assumed an objective with a NA of 1.0, fulfilling the sine condition, and a two-photon excitation wavelength of 1100nm. We assumed further that the objective is corrected for use with a coverslip so that the latter does not need to be taken into account in the calculation. Using the concept of high-NA defocus (Botcherby, et al., 2007) under a refractive index mismatch (Binding, 2008), the wavefront corresponding to focusing at a given depth inside the sample was calculated. For the sample, a homogeneous refractive index with the experimentally determined value was used and a perfectly flat surface orthogonal to the optical axis was assumed, knowing that experimental conditions with tilted and non-flat surfaces will further increase the aberrations. Using the non-paraxial Debye approximation (Born & Wolf, 1999), the two-photon excitation point spread function (PSF) was calculated for said wavefront. Since typical two-photon lasers have a much smaller wavelength bandwidth (around 15nm FWHM) than the source used in our OCT experiments (~170mm FWMM), dispersion has been neglected for this calculation.

In calculating this PSF at different depths, the theoretical loss in lateral and axial resolution as well as the loss in two-photon excitation was determined – for a single fluorophore, for a fluorescent plane and for a uniformly stained sample (Figure 5-1).

There is a steep drop in fluorescence excitation probability between the depths of 100 and 400μm, before reaching a plateau, where the decrease with depth is much smaller. At 400μm, an axially thin object such as a single fluorophore or a fluorescent membrane is excited with only 22% efficiency compared to the surface, due to a refractive index mismatch-induced spherical aberration, while fluorescence from an object larger than the aberrated focus is still excited with 57% efficiency.
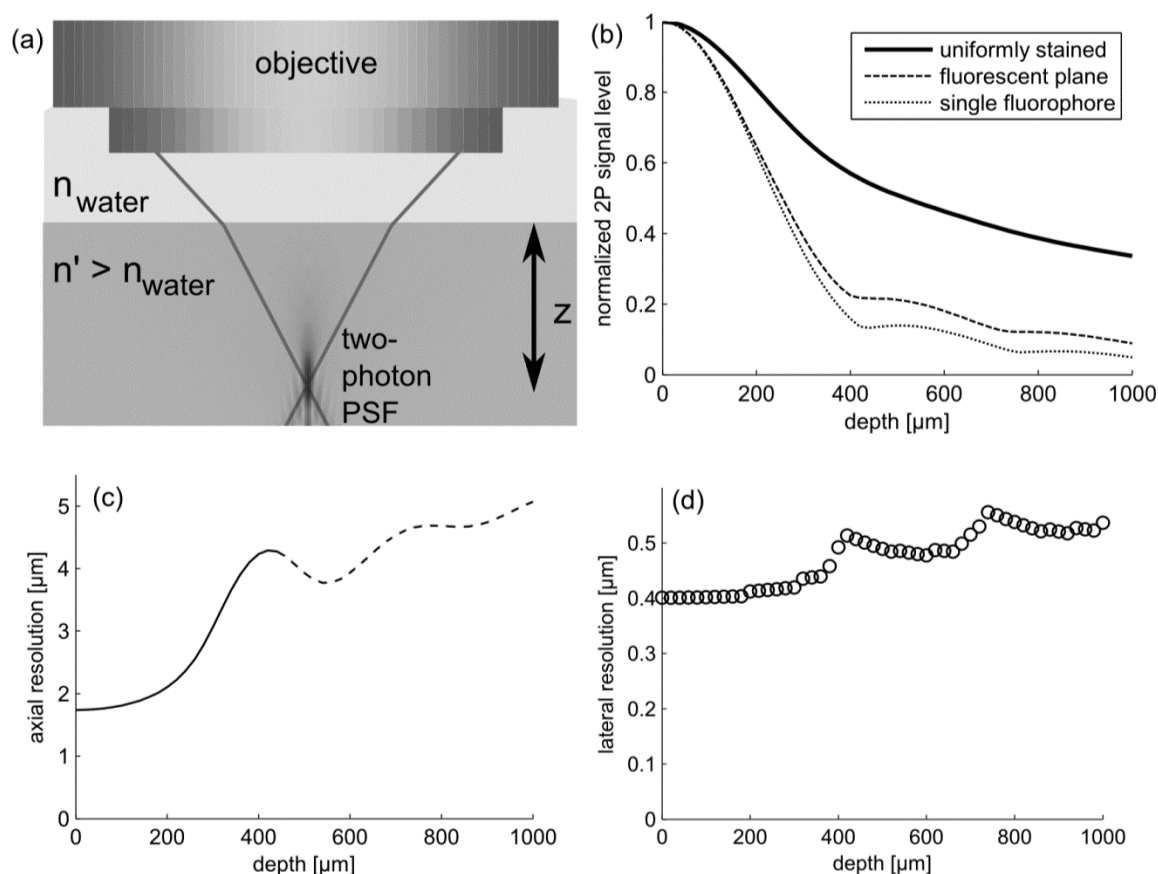
Figure 5-1. Consequences of refractive index mismatch for 2PLSM. (a) Schematic drawing of the situation being simulated: a water immersion objective is used to focus a laser beam into a sample with refractive index n' which is larger than the refractive index n of the immersion medium. The aberrated two-photon excitation PSF for imaging at different depths z is calculated and analyzed. (b) Two-photon excitation loss caused by depth aberrations: for a single fluorophore (i.e. maximum of PSF), a fluorescent sheet (brightest xy plane of the PSF) and uniformly stained sample (3D integral of PSF). (c) Loss in axial resolution in 2PLSM (FWHM of response to fluorescent sheet, determined from a Gaussian fit to the simulated PSF). (d) Loss in lateral resolution in 2PLSM (FWHM of response to single fluorophore, determined from a Gaussian fit to the simulated PSF)

To estimate the lateral resolution, a 1D-section through the calculated PSF was fitted with a Gaussian function, while the axial resolution was determined from fitting a Gaussian to the axial response to a fluorescent plane. The axial resolution is decreased by a factor of 2.5 in 400µm depth, while the lateral resolution decreases only by 20%. Due to the complicated form of the PSF beyond 400µm depth, it is rather meaningless to describe it with a single value for axial resolution.

5.1 Discussion

The simulations presented here show that even though the refractive index of the rat brain is only slightly greater than that of water, the refractive index mismatch implies a considerable signal and resolution loss in 2PLSM due to optical aberrations, in particular at the large imaging depths possible with modern powerful laser systems (Theer & Denk, 2006). Even in the most favorable case, where the refractive index is assumed to be homogeneous and the brain surface perfectly flat, our calculations show that diffraction-limited imaging is not possible beyond the first 200 µm of tissue and the PSF is severely deteriorated beyond 400 µm depth. 2PLSM in the living brain should therefore benefit from aberration correction using adaptive optics or even just a predefined, depth-dependent correction of the spherical aberration if no higher order aberrations exist.

Of course aberration correction should always be attempted starting from the most favorable circumstances. Currently available microscope objectives tend to be corrected for visible light. Therefore the assumption of a perfect objective is not valid at wavelengths in the near-infrared, and the intensity calculations performed here would only be valid after full correction of these system aberrations.

Apart from wavelength, the immersion medium is also important. For a water-based sample such as biological tissue, a water immersion lens should be used, whereas the use of glycerin embedded samples require the use of a glycerin immersion objective. To be able to make best use of high-NA oil immersion lenses, care must be taken to match perfectly the refractive index of the embedding medium of the fixed sample to the refractive index of the immersion oil. While several publications exist about correcting aberrations arising from violating this basic rule, only little work has been carried out to correct true sample-induced aberrations in 2PLSM caused by the small refractive index mismatch between water and tissue (Rueckel, et al., 2006; Débarre, et al., 2009; Ji, et al., 2009). In some of these latter cases, aberrations due to the shape of the sample surface were dominant. In 2PLSM of the brain, a coverslip is

generally used to protect the tissue. If the bone around the craniotomy is appropriately thinned, the coverslip can be brought in direct contact with the brain tissue, ensuring a flat sample surface and removing surface-shape-associated aberrations.

Our results now show that even in this best possible configuration with a water immersion objective, flat brain surface and assuming a homogeneous brain refractive index, correction of sample induced spherical aberration could drastically improve 2PLSM in the animal brain, making adaptive optics an interesting route to follow.

Recently, pupil segmentation was used to determine both the total level of aberrations *in vivo* in the mouse brain as a function of depth between 70 and 400 μm, and the axial FHWM of 2 μm beads at these depths when correcting only system aberrations, using an NA 0.8 20× water immersion objective and an excitation wavelength of 900 nm (Ji, et al., 2012). These experiments found an increase in axial FWHM from 4 to 6 μm in the depth range studied; the signal loss could not be well quantified from their measurements, since the data was too noisy. Due to the lower NA used in their experiments compared to our simulations and the large size of the fluorescent beads, it seems reasonable that their initial axial FWHM should be larger, and that its increase with depth should be slower.

Much smaller beads (200 nm) were used for experiments with cortical slices at 725 nm excitation wavelength with an NA 0.9 60× water immersion objective (Chaigneau, et al., 2011). They observed an increase in axial FWHM from 1.9 μm to 3.3 μm when imaging through 150 μm thick tangential cortical slices. Unfortunately, their system did not allow to completely fill the back aperture of the objective, and apparently no independent measurement of the fill factor was available. They resorted to calculating an effective NA from their two-photon PSF, which makes comparison of their results with theoretical expectations difficult, since an absolute scale is lacking. However, the fact that their PSF increases by a much larger factor over the first 150 μm than calculated in our simulations suggests that the aberrations caused by their sample are not dominated by spherical aberration, but instead contain also other aberration modes.

6 Maximum-A-Posteriori Focus and Stigmation (MAPFoSt)[7]

6.1 Introduction

In electron microscopy (EM), the image sharpness is typically optimized by adjusting the focal length of the objective lens (often called the "working distance") and the strength of two stigmation elements. This corresponds to correcting the second-order aberrations defocus and astigmatism of the incoming electron wave. The automatic focus-and-stigmation routines built into most commercial scanning electron microscopes (SEMs) typically involve repeatedly scanning a small sample area at high magnification and presumably use metric-based optimization schemes, whether based on image sharpness or other parameters. Metric-based approaches are still being actively researched (Rudnaya, et al., 2009; Rudnaya, et al., 2011a; Rudnaya, et al., 2011b). For samples that are affected strongly by exposure to the incident electron beam, such as plastic-embedded biological tissue, performing even a single focusing-and-stigmation cycle, whether manually or automatically, leaves a visibly damaged area, thereby compromising subsequent imaging. Often a "sacrificial" area outside the region to be imaged is, therefore, used to find the correct focus and stigmation parameters (Briggman, et al., 2011). A sacrificial area is not always available, for example because the entire sample area needs to be imaged (often the case for serial block-face imaging), or because the sample cannot be translated to and from the sacrificial area quickly or reproducibly enough. In such cases, an area within the region to be imaged needs to be used for focusing and stigmation. It is this situation for which our algorithm is intended.

As discussed briefly in the general introduction, heuristically choosing a metric to compare and evaluate different test images inherently limits the information being extracted from each test image. Aberrations have a different effect on different spatial frequencies in the image, which cannot be reflected by a single metric. To mitigate, one could imagine defining one metric for each spatial frequency, some of which will be redundant while others will provide complementary information. This leads to the question how the information from these

---

[7] This chapter has been submitted for publication under the title "Low-dosage Maximum-A-Posteriori Focusing and Stigmation (MAPFoSt)" by Jonas Binding, Shawn Mikula and Winfried Denk.

different metrics should be combined to achieve the best possible wavefront estimation given certain data.

For astronomical applications a wavefront sensing technique called "phase diversity" has been described (Gonsalves, 1982) and used, in particular, for solar imaging (Löfdahl & Scharmer, 1994) and for the determination of static aberrations (Blanc, et al., 2003; Sauvage, et al., 2007). Phase diversity requires just two test images to determine all aberration parameters. One weakness of existing implementations for electron microscopy (Nicolls, et al., 1997; Ogasawara, et al., 1998; Baba, et al., 2001) is that they use the *ratio* of the Fourier spectra of the two test images for parameter estimation. While this was an improvement over implementations based on comparing thresholded Fourier spectra (Ong, et al., 1998), this, as does any ratio-based approach, amplifies noise in regions with weak signal and is therefore ill-suited for low-dose imaging.

The need for ratios can be avoided by using a statistical approach. In particular, a maximum-likelihood (ML) estimator has been thoroughly investigated for incoherent imaging systems in general (Paxman, et al., 1992). The idea is that a model for image formation including noise model can be exploited to determine the likelihood function of different measurements (data) given certain underlying aberrations; this likelihood can now be maximized with respect to the aberration parameters for the known measurements. Their work provides a solid framework for dealing with any parameterization of the aberration function and has spurred a number of studies in astronomy (for example Löfdahl & Scharmer, 1994; Meynadier, et al., 1999; Scharmer, et al., 1999; Dean & Bowers, 2003; Dolne, et al., 2003; Sauvage, et al., 2007) and light microscopy (Hanser, et al., 2003). Unfortunately the generality of Paxman's solution comes at the expense of a considerable computational burden in the form of repeated Fourier transforms during the search for the likelihood maximum (Scharmer, et al., 1999).

In this chapter we describe a phase-diversity-based algorithm, which we call Maximum-a-Posteriori Focusing and Stigmation (MAPFoSt) and which is much more computationally efficient, using only mild assumptions. We analyzed how the estimation precision depends on the signal-to-noise ratio and on the magnitude of the aberration change between the test images. We also compared MAPFoSt with the built-in autofocus of the electron microscope, as well as with a heuristic algorithm used routinely (Briggman, et al., 2011) for SBEM (Denk & Horstmann, 2004). We present preliminary results from using MAPFoSt while block-face scanning a cross section through a whole brain.

6.2 Materials and methods

6.2.1 The MAPFoSt algorithm

Why changing defocus allows for determining astigmatism

A scanning electron microscope focuses electrons emitted from a point-like source using a number of electrostatic and electromagnetic lenses. To achieve a high resolution, the focal spot on the sample surface needs to be as small as possible. Deviations from rotational symmetry of the electron-optical column lead to aberrations such as astigmatism and are caused, for example, by manufacturing tolerances, irregular surface contamination, and stray magnetic fields. The voltages and currents applied to different parts of the column change whenever key parameters of the SEM are changed, such as the electron landing energy, the working distance or the beam current. This can have a strong impact on the strength and orientation of astigmatism, making static, permanent correction impossible. To allow the compensation of astigmatism at runtime, addressable magnetic or electrostatic stigmators are integrated into the column.

Aberrations affect the modulation transfer function, which blurs the image as some or all of the high spatial frequencies are attenuated. While blurring can indicate the presence of aberrations, it is impossible to quantitatively estimate even the degree of defocus, let alone both defocus and astigmatism, from a single image. Isotropic blurring can, for example (Figure 6-1b), be caused by the lack of any fine structure in the object, by defocus, or by astigmatism (if the object is, in fact, in focus). However, if a second image of the same object taken at a different focus setting is available, these cases can be distinguished. Astigmatism will, for example, lead to pronounced changes in the sharpness anisotropy as the focus setting is changed (Figure 6-1c). In the next section we will show how we can estimate the size of the aberrations present during the acquisition of both images using the Fourier transforms of these two images and the knowledge of how the modulation transfer function depends on the aberrations.
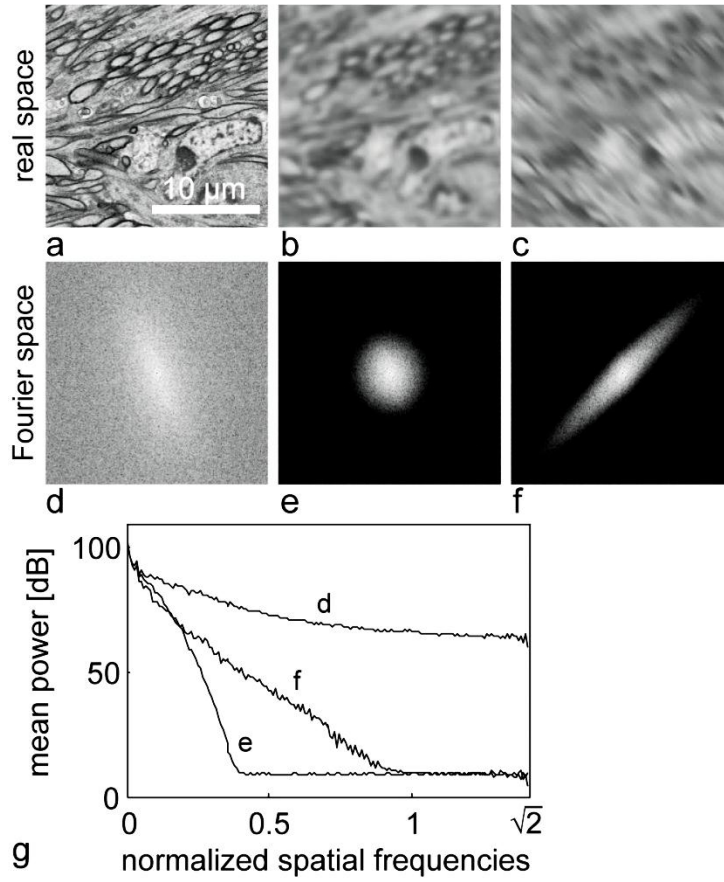
Figure 6-1. The effect of aberrations on images and spatial-frequency spectra. a) Average of 4 identical, well-focused SEM images of a microtome-smoothed cross-section through an epoxy-embedded, osmium-stained mouse brain block surface coated with ~5 nm platinum-carbon. The images were acquired with a landing energy of 5 keV and a beam current of 1.0 nA using secondary-electron detection, and sampled at 80 nm pixel size and 1.6 μs dwell time. Simulated images with b) 90 μm of astigmatism and c) 90 μm of astigmatism plus 120 μm of defocus using the image in (a) as the object. Scale bar 10 μm in a) is valid for a)-c). d)-f). Fourier transforms of a)-c) respectively, with zero frequency at the center and a logarithmic gray scale. g) Angularly averaged power spectra with and without aberrations, with spatial frequencies given in terms of the Nyquist frequency (1/160 nm^{-1}).

The imaging process

We assume translation invariance, i.e. the electron beam's shape does not change as it is scanned; we further assume the absence of field curvature, and additive Gaussian noise as an approximation to shot noise. We also use ray optics as opposed to wave optics, because the pixel sizes used (5-80 nm) are well above the diffraction limit ($\lambda / NA / 2$, in our case 1.7 nm). In contrast to light microscopes with confocal detection, the PSF of the SEM is based

entirely on the scanned incident beam; the detection system does not play a role for the PSF due to its low spatial selectivity. Our imaging model is thus

$$I_r(x,y) = \iint O_r(x-x', y-y') PSF(x', y', \mathbf{A}) dx' dy' + n_r(x,y)$$

Eq. 6-1,

where $I_r(x,y)$ is the intensity of the image pixel at coordinates *(x,y)*, $O_r(x,y)$ is the object intensity at the corresponding coordinates and $PSF(x,y,\mathbf{A})$ is the point spread function of the microscope. $n_r(x,y)$ is the noise; the subscript "*r*" indicates real space. The *PSF* depends on the aberration vector $\mathbf{A}=(z, a_{on\text{-}axis}, a_{diag})$, where z is the defocus and $a_{on\text{-}axis}$, a_{diag} are the coefficients for the on-axis and diagonal astigmatism modes. We consider only these three aberrations explicitly here but a generalization to higher modes should be easily possible. The double integral over *dx'* and *dy'* corresponds to a convolution of object and point-spread function. The model can be more easily described in Fourier space:

$$I(k_x, k_y) = O(k_x, k_y) MTF(k_x, k_y, \mathbf{A}) + n(k_x, k_y)$$

Eq. 6-2,

where $I(k_x, k_y)$, $O(k_x, k_y)$ and $n(k_x, k_y)$ are the Fourier transforms of $I_r(x,y)$, $O_r(x,y)$ and $n_r(x,y)$, respectively, *MTF* is the modulation transfer function, i.e. the Fourier transform of the *PSF*, and k_x, k_y are the components of the spatial wave vector. Note that in general, $I(k_x, k_y)$, $O(k_x, k_y)$ and $n(k_x, k_y)$ are complex quantities, while the *MTF* is real as long as the *PSF* is symmetric with respect to inversion, $PSF(x,y,\mathbf{A})=PSF(-x,-y,\mathbf{A})$.

The modulation transfer function (MTF)

We assume that the intensity of the electron beam is constant across the aperture, i.e. the intensity profile is top-hat shaped. The beam is focused onto the sample by a generally astigmatic lens system. The width of the beam in any plane depends on the numerical aperture (*NA*) of the electron beam and on the distance z of the plane from the focus. When astigmatism ($a_{on\text{-}axis}$, a_{diag}) is present, the beam has two orthogonal line foci, at $z_{line} = \pm\sqrt{a_{on\text{-}axis}^2 + a_{diag}^2}$ above and below the nominal focal plane ($z=0$), and is circular at z=0 as long as |$\mathbf{A}$| is small compared to the working distance. The shape of the beam and hence the *PSF* in any plane is an ellipse. Since the *MTF* is the Fourier transform of the *PSF*, it can be

expressed (see section 9.2 for the derivation) in terms of the first Bessel function of the first kind J_1 with the help of

$$\rho \equiv NA\sqrt{2a_{on-axis}(k_x^2 - k_y^2)z - a_{diag}k_x k_y z + (k_x^2 + k_y^2)(a_{on-axis}^2 + a_{diag}^2 + z^2)}$$

Eq. 6-3

As

$$MTF(k_x, k_y, \mathbf{A}) = \frac{2J_1(\rho)}{\rho}$$

Eq. 6-4,

which we will call a "Bessel-*MTF*" and where *NA* (assuming sin(*NA*)=*NA*) is half the opening angle of the converging electron beam. Because the *z* is always small compared to the focal length, we can assume *NA* to be independent of *z*.

For simplicity and computational speed, we used a different *MTF* in simulations and some initial experiments as noted below. It corresponds to a Gaussian radial intensity profile of the *PSF* instead of the hard cut-off of a physical aperture and results in

$$MTF(k_x, k_y, \mathbf{A}) = \exp\left(-\frac{1}{8}\rho^2\right)$$

Eq. 6-5,

this will be referred to as the "Gaussian *MTF*". The scaling factor 1/8 ensures that the Bessel-*MTF* and the Gaussian *MTF* agree for small aberrations and/or small spatial wave vectors (k_x, k_y).

We define the depth of field Δ of the imaging system as that defocus where the *PSF* radius matches the pixel size, *p*, i.e. $\Delta = p / NA$. For a one-dimensional system, z=Δ would mean the *MTF* is exactly 0 at the Nyquist frequency, but in the 2D case discussed here the first zero is at a slightly larger defocus.

The approach used by Paxman et al. (Paxman, et al., 1992) starts from the generalized pupil function and requires a Fourier transform for each evaluation of the *MTF*, while our *MTF* can be expressed directly in terms of the aberration parameters.

The Fourier transforms (Figure 6-1e/f) of the two images $I_1(k_x, k_y)$ and $I_2(k_x, k_y)$ (Figure 6-1b/c) are

$$I_1(k_x, k_y) = O(k_x, k_y) MTF(k_x, k_y, \tilde{\mathbf{A}} + \mathbf{T}_1) + n_1(k_x, k_y)$$

Eq. 6-6

and

$$I_2(k_x, k_y) = O(k_x, k_y) MTF(k_x, k_y, \tilde{\mathbf{A}} + \mathbf{T}_2) + n_2(k_x, k_y)$$

Eq. 6-7,

which are the products of the Fourier transform (Figure 6-1d) of the object O (Figure 6-1a) with the *MTF*s for $\tilde{\mathbf{A}} + \mathbf{T}_1$ and $\tilde{\mathbf{A}} + \mathbf{T}_2$, respectively. $\tilde{\mathbf{A}}$ is the aberration to be determined and $\mathbf{T}_1$ and $\mathbf{T}_2$ are the test aberrations.

MAPFoSt using only a single wave vector

To illustrate the MAPFoSt concept we first consider the case of a single wave vector $\mathbf{k}'$ and one aberration mode (e.g. $\tilde{\mathbf{A}} = (\tilde{A}, 0, 0)$, $\mathbf{T_i}=(T_i, 0, 0)$), i.e. from two test images (Figure 6-2a) we only analyze a single scalar (but complex-valued) Fourier component $I_1 = I_1(\mathbf{k}')$, $I_2 = I_2(\mathbf{k}')$ which can be expressed as

$$I_1 = O\, MTF(\mathbf{k}', \tilde{\mathbf{A}} + T_1) + n_1$$

Eq. 6-8

and

$$I_2 = O\, MTF(\mathbf{k}', \tilde{\mathbf{A}} + T_2) + n_2$$

Eq. 6-9.

Let us first assume that there is no noise, i.e. $n_1=n_2=0$. Since we know the test aberrations T_1 and T_2 imposed when acquiring the two images I_1 and I_2, respectively, we can determine O and $\tilde{A}$ using Eq. 6-8 and Eq. 6-9. This corresponds to finding (A, O) for which both

$$O(A) = \frac{I_1}{MTF(A+T_1)}$$

Eq. 6-10

and

$$O(A) = \frac{I_2}{MTF(A+T_2)}$$

Eq. 6-11

are true. For a Gaussian *MTF* these curves are U-shaped and have a unique intersection (Figure 6-2b). For a Bessel *MTF*, there are additional U-shaped curve segments (one between each pair of zero-crossings of the *MTF*), so there are multiple intersections. This ambiguity can be resolved by combining data from different wave vectors (see below).

If some noise is present, these equations are still approximately true, but they become probabilistic: (A, O) pairs, which approximately obey Eq. 6-10 and Eq. 6-11 are more likely than other (A, O) pairs. In other words, the joint probability distribution for A and O given one of the images has a ridge along the curve defined by the corresponding equation, and is smeared out due to noise. The joint probability distribution given both images corresponds to the product of the individual distributions and has its peak, indicating the most likely values, near the actual A and O.

For Gaussian noise, with standard deviation of σ, we can calculate these probability distributions by starting from the forward model, i.e. how likely certain image values I_1, I_2 are, given the aberration $\tilde{A}$ and the object amplitude O:

$$p(I_1 \mid \tilde{A}, O) = \frac{1}{2\pi\sigma^2} \exp\left(-\frac{\left| I_1 - O\, MTF(\tilde{A}+T_1) \right|^2}{2\sigma^2} \right)$$

Eq. 6-12,

76

$$p(I_2 \mid \tilde{A}, O) = \frac{1}{2\pi\sigma^2} \exp\left(-\frac{\left| I_2 - O\,MTF(\tilde{A} + T_2) \right|^2}{2\sigma^2} \right)$$

Eq. 6-13,

where $p(I_1 \mid \tilde{A}, O)$ is called the likelihood and can be read as "the probability of measuring I_1 given $\tilde{A}$ and O".

Using Bayes' theorem, we can "invert" this and calculate the posterior probability for (A, O) given images I_1, I_2:

$$p(A, O \mid I_1, I_2) = \frac{p(A, O)}{p(I_1, I_2)} p(I_1, I_2 \mid A, O) = \frac{p(A)p(O)}{p(I_1, I_2)} \prod_{i=1}^{2} p(I_i \mid A, O)$$

Eq. 6-14

We have to choose priors for A and O, for example

$$p(A) = \begin{cases} \dfrac{1}{2A_{max}} & |A| \le A_{max} \\ 0 & otherwise \end{cases}$$

Eq. 6-15

and

$$p(O) = \begin{cases} \dfrac{1}{4O_{max}^2} & \max(|\mathrm{Re}(O)|, |\mathrm{Im}(O)|) \le O_{max} \\ 0 & otherwise \end{cases}$$

Eq. 6-16,

which we will refer to as top-hat priors, where $\mathrm{Re}(O)$ and $\mathrm{Im}(O)$ are the real and imaginary parts of O, respectively, and A_{max} and O_{max} are the maximum values for A and O, respectively. Given the Fourier components I_1, I_2 from two images for some $\mathbf{k}' = \mathbf{k}_1$ and assuming top-hat priors, we can use Eq. 6-14 to calculate a posterior using only I_1 (Figure 6-2c/d top, red), only I_2 (Figure 6-2c/d top, green) or both (Figure 6-2c/d top, yellow).
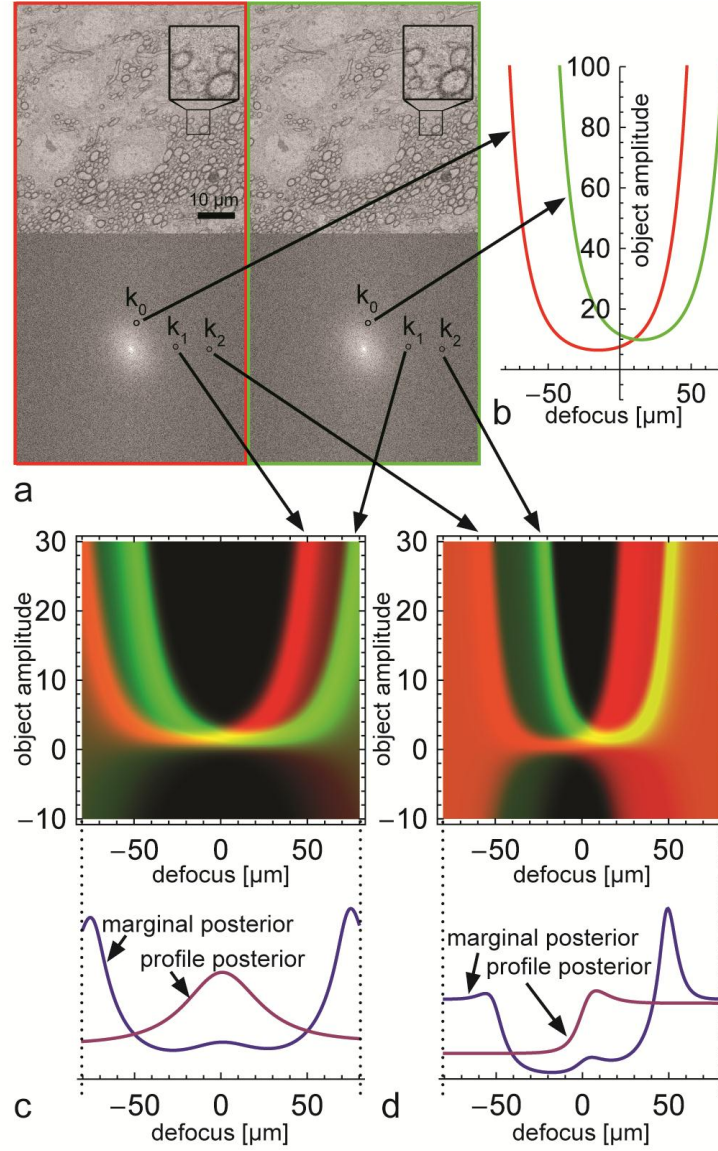
Figure 6-2. Aberration estimation using just one Fourier component, assuming a Gaussian MTF. a) A pair of images and their Fourier transforms at an unknown initial aberration plus test aberration $T_1 = -15$ μm (green) and $T_2 = +15$ μm (red). NA is 5 mrad, pixel size 80 nm. b) Ignoring noise in the images, (A,O) pairs consistent with the Fourier component $\mathbf{k}' = \mathbf{k}_0$ from the "green" (Eq. 6-10) and "red" (Eq. 6-11) images. c) Top: the 2D posteriors (Eq. 6-14) for wave vector $\mathbf{k}' = \mathbf{k}_1$ ($|\mathbf{k}_1| = 15$ rad/μm), based on $\mathrm{Re}[I_1(\mathbf{k}_1)] = 1.44$ (red density) and $\mathrm{Re}[I_2(\mathbf{k}_1)] = 1.49$ (green density). Top-hat prior with $|A| \leq 80$ μm, $|O| \leq 30$. Bottom: marginal posterior (blue curve) and profile posterior (purple curve) derived from the above 2D posterior by integrating out the object or taking the maximum over all possible objects, respectively. d) Like (c) but for a higher spatial frequency ($|\mathbf{k}_2| = 26.25$ rad/μm) where signal in the left image is below noise level ($\mathrm{Re}[I_1(\mathbf{k}_2)] = 0.55$).

Since our goal is to estimate *A,* not *O,* we need to eliminate *O*. This is possible by integrating over *O* to find the marginal posterior *p(A/I₁,I₂)*. However, because the posterior *p(A,O/I₁,I₂)* does not drop off quickly enough for large aberration values, the marginal distribution often diverges relatively quickly for large aberration values (Fig 2c bottom, blue curve), even when the two-dimensional posterior *p(A,O/I₁,I₂)* shows a clear peak (Fig 2c top, yellow region). In fact, outside the "U"-shaped regions the posterior never goes to zero, but approaches a fixed value. The reason for this behavior is that a given data pair *(I₁,I₂)* is consistent with any arbitrarily large aberration *A* where $O \, MTF(A) \approx 0$ and *I₁=n₁, I₂=n₂*, i.e. any image pair can be explained as pure noise and aberrations strong enough to completely suppress the influence of the object *O*. This is a problem when no sufficient prior knowledge about the object is available and a conservatively large upper bound for *O* has to be chosen.

For this reason, we decided to not integrate out the object *O*, but rather perform a maximum-a-posteriori co-estimation of *A* and *O*, i.e. finding the *(A,O)* pair that maximizes *p(A,O/I₁,I₂)* (brightest yellow peak in Figure 6-2c). For speed reasons, which will be discussed in detail below, we performed the maximization in two steps (Paxman, et al., 1992): first we found the maximum with respect to *O* for all values of *A*,

$$p(A \,|\, O = O_{MAP}, I_1, I_2) = \max_{O} \, p(A, O \,|\, I_1, I_2)$$

Eq. 6-17.

This function, which only depends on *A*, will be called the profile posterior distribution, since it represents the maximum projection, or silhouette, of *p(A,O/I₁,I₂)*.

The profile posterior distribution typically has a well-defined, albeit rather wide maximum; for our example (Figure 6-2c bottom, purple curve) it is well approximated by a Gaussian centered at *A=0* μm with *σ=30* μm.

To understand the behavior of the posterior better, it is instructive to look at a third spatial wave vector, $\mathbf{k}' = \mathbf{k}_2$, from the same image (Figure 6-2d), for which the data in the first image has a value below noise level (Fig 2d top, red). In that case the data is consistent with any *(A,O)* pair for which $O \, MTF(A + T_1) \approx 0$, so instead of one thin "U"-shaped region the whole *A-O*-plane outside two "U" shapes has substantial probability.

The peak of the profile posterior (Fig 2d, bottom, purple curve) is nevertheless well defined, lying in our example near A=7 μm, while the high shoulders show that arbitrarily large aberrations are nearly as likely, if we only look at this one k.

Fast calculation of the profile posterior

In the previous section, the posterior was calculated everywhere on an *A-O*-grid, for didactic purposes. The profile posterior was then determined by numerical maximum projection. It is much faster to calculate the profile posterior directly, where possible. For this, we need to find the maximum-a-posteriori object O_{MAP}, i.e. the object for which $p(A,O/I_1,I_2)$ is maximal for a fixed *A*.

Necessary conditions for O_{MAP} are

$$\left.\frac{\partial p(A,O\,|\,I_1,I_2)}{\partial \operatorname{Re}(O)}\right|_{O=O_{MAP}} \overset{!}{=} 0$$

Eq. 6-18

and

$$\left.\frac{\partial p(A,O\,|\,I_1,I_2)}{\partial \operatorname{Im}(O)}\right|_{O=O_{MAP}} \overset{!}{=} 0$$

Eq. 6-19.

Whether this can be solved explicitly depends essentially on the prior p(O) chosen. In particular, an explicit solution exists for three important special cases, namely the top-hat prior, Gaussian prior and the limiting case of a completely flat prior.

Using Eq. 6-12, Eq. 6-13, Eq. 6-14 and the top-hat prior for *O* (Eq. 6-16) we get

$$O_{MAP} = \operatorname{Re}(O_{MAP}) + i \operatorname{Im}(O_{MAP})$$

Eq. 6-20

with *i* the imaginary unit and

$$\text{Re}(O_{MAP}) = \begin{cases} \dfrac{\text{Re}(I_1)MTF(A+T_1) + \text{Re}(I_2)MTF(A+T_2)}{MTF(A+T_1)^2 + MTF(A+T_2)^2} & \left| \dfrac{\text{Re}(I_1)MTF(A+T_1) + \text{Re}(I_2)MTF(A+T_2)}{MTF(A+T_1)^2 + MTF(A+T_2)^2} \right| \leq O_{max} \\[4mm] O_{max}\,\text{sgn}\left[\text{Re}(I_1)MTF(A+T_1) + \text{Re}(I_2)MTF(A+T_2) \right] & \left| \dfrac{\text{Re}(I_1)MTF(A+T_1) + \text{Re}(I_2)MTF(A+T_2)}{MTF(A+T_1)^2 + MTF(A+T_2)^2} \right| > O_{max} \end{cases}$$

Eq. 6-21

$$\text{Im}(O_{MAP}) = \begin{cases} \dfrac{\text{Im}(I_1)MTF(A+T_1) + \text{Im}(I_2)MTF(A+T_2)}{MTF(A+T_1)^2 + MTF(A+T_2)^2} & \left| \dfrac{\text{Im}(I_1)MTF(A+T_1) + \text{Im}(I_2)MTF(A+T_2)}{MTF(A+T_1)^2 + MTF(A+T_2)^2} \right| \leq O_{max} \\[4mm] O_{max}\,\text{sgn}\left[\text{Im}(I_1)MTF(A+T_1) + \text{Im}(I_2)MTF(A+T_2) \right] & \left| \dfrac{\text{Im}(I_1)MTF(A+T_1) + \text{Im}(I_2)MTF(A+T_2)}{MTF(A+T_1)^2 + MTF(A+T_2)^2} \right| > O_{max} \end{cases}$$

Eq. 6-22,

where sgn() is the signum function.

Alternatively, for a Gaussian prior for O with variance $\sigma_O{}^2$,

$$p(O) = \frac{1}{2\pi\sigma_O{}^2} \exp\left(-\frac{|O|^2}{2\sigma_O{}^2} \right)$$

Eq. 6-23.

we get

$$O_{MAP} = \frac{\sigma_O{}^2 \left[I_1 MTF(A+T_1) + I_2 MTF(A+T_2) \right]}{\sigma^2 + \sigma_O{}^2 \left[MTF(A+T_1)^2 + MTF(A+T_2)^2 \right]}$$

Eq. 6-24.

In the limiting cases $O_{max} \to \infty$ (for a top-hat prior) and $\dfrac{\sigma_O}{\sigma} \to \infty$ (for a Gaussian prior), which both correspond to the completely flat prior, O_{MAP} simplifies to

$$O_{MAP} = \frac{I_1 MTF(A+T_1) + I_2 MTF(A+T_2)}{MTF(A+T_1)^2 + MTF(A+T_2)^2}$$

Eq. 6-25.

Any of these expressions for O_{MAP} can now be plugged into the posterior (Eq. 6-14) to yield the profile posterior. For the completely flat prior, the profile posterior is

$$p(A \mid O = O_{MAP}, I_1, I_2) = \frac{p(A)}{p(I_1, I_2)} \frac{1}{4\pi^2\sigma^4} \exp\left(-\frac{|I_2 MTF(A+T_1) - I_1 MTF(A+T_2)|^2}{2\sigma^2\left[MTF(A+T_1)^2 + MTF(A+T_2)^2\right]}\right)$$

Eq. 6-26.

Note that if the prior on *A*, p(*A*), is also chosen to be completely flat, our MAP formalism is equivalent to a maximum-likelihood approach.

MAPFoSt using multiple wave vectors

Until now, we have investigated in detail how to estimate aberrations using image data from only a single Fourier component (wave vector) at a time. To use all the information present in the images, we now need to combine the estimates from different wave vectors. To do this we can calculate the high-dimensional joint likelihood $p(\mathbf{I}_1, \mathbf{I}_2 \mid \mathbf{A}, \mathbf{O})$ and apply Bayes theorem, before again determining the profile posterior. Note that bold print is used for vectors; **O** and **I$_i$** are vectors containing all Fourier components of the object and image respectively.

However, since the object and image amplitudes for each wave vector are completely independent from the amplitudes for all other wave vectors, both the joint likelihood and the full prior $p(\mathbf{O}) \equiv p(O(k_1))p(O(k_2)) \dots p(O(k_R))$ factorize completely. Thus, the results from the previous section apply directly and we can simply calculate the combined profile posterior as the product of the profile posteriors for each wave vector. We only have to make sure to include the prior on **A** only once, resulting in

$$p(\mathbf{A} \mid \mathbf{O} = \mathbf{O}_{MAP}, \mathbf{I}_1, \mathbf{I}_2) = \frac{p(\mathbf{A})}{p(\mathbf{I}_1, \mathbf{I}_2)} \frac{1}{\left(4\pi^2\sigma^4\right)^R}$$

$$\times \prod_{k_x, k_y} \exp\left(-\frac{\left[I_2(k_x, k_y)MTF(k_x, k_y, \mathbf{A}+\mathbf{T}_1) - I_1(k_x, k_y)MTF(k_x, k_y, \mathbf{A}+\mathbf{T}_2)\right]^2}{2\sigma^2\left[MTF(k_x, k_y, \mathbf{A}+\mathbf{T}_1)^2 + MTF(k_x, k_y, \mathbf{A}+\mathbf{T}_2)^2\right]}\right)$$

Eq. 6-27,

where $O(k_x, k_y)$, $I_i(k_x, k_y)$ refer to values for a single wave vector. $p(\mathbf{I_1}, \mathbf{I_2})$ is the prior probability of the data, which normalizes the probability but does not depend on **A** or **O** and therefore does not affect the location of the maximum. *R* is the number of wave vectors used.

The number of coefficients that can be estimated depends on how many wave vectors (typically a large number) we can use. For example, we routinely used R=768² wave vectors for 3 aberration modes. The earlier example was restricted to a single aberration parameter simply because two measurements (the amplitudes of one spatial frequency in two test images) only allow the estimation of at most two unknowns, the object amplitude and one aberration parameter.

Applying Eq. 6-27 to an image pair from our SEM (Figure 6-2a) results in an extremely sharply peaked profile posterior (Figure 6-3).
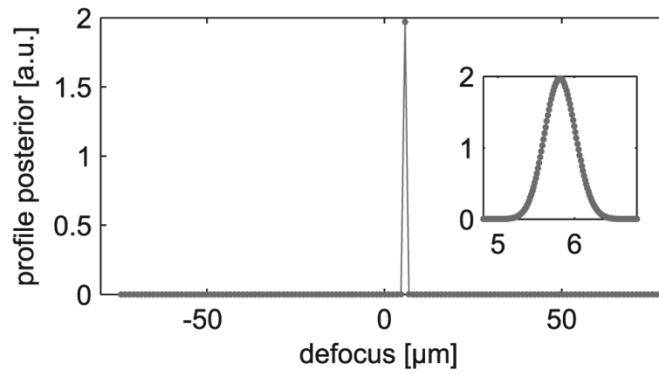
Figure 6-3. Product of the profile posteriors from all spatial frequencies in Figure 6-2. The inset shows a zoom onto the peak.

The peak position $z = (5.8 \pm 0.3)$ µm found in our example implies that the two test images were recorded at $z + T_1 = 20.8$ µm and $z - T_1 = 9.2$ µm defocus, respectively.

More than two test images

Two images taken at different focal settings are sufficient to determine defocus and both astigmatism components. However, we can include information from additional images $\mathbf{I_i}$ of the same object (Paxman, et al., 1992) by generalizing Eq. 6-14:

$$p(\mathbf{A}, \mathbf{O} \mid \mathbf{I_1}, \mathbf{I_2}, \cdots, \mathbf{I_n}) = p(\mathbf{A}) p(\mathbf{O}) \frac{\displaystyle\prod_{k_x, k_y, i} p(I_i(k_x, k_y) \mid \mathbf{A}, O(k_x, k_y))}{p(\mathbf{I_1}, \mathbf{I_2}, \cdots, \mathbf{I_n})}$$

$$= p(\mathbf{A}) p(\mathbf{O}) \frac{\displaystyle\prod_{k_x, k_y, i} \frac{1}{2\pi\sigma^2} \exp\left(-\frac{\left| I_i(k_x, k_y) - O(k_x, k_y)\, MTF(k_x, k_y, \mathbf{A} + \mathbf{T_i}) \right|^2}{2\sigma^2} \right)}{p(\mathbf{I_1}, \mathbf{I_2}, \cdots, \mathbf{I_n})}$$

Eq. 6-28

6.2.2 Data analysis

To find the MAP value for **A** one needs to find the maximum of the profile posterior (Eq. 6-27). In order to determine **A**$_{\textbf{MAP}}$ we used the Matlab function minimize.m (Rasmussen, 2006), which implements a local gradient search to minimize the expression $-\ln\left[p(\mathbf{A} \mid \mathbf{O}=\mathbf{O_{MAP}}, \mathbf{I_1}, \mathbf{I_2}) \right]$.

To estimate the uncertainty $\boldsymbol{\sigma}_{\textbf{est}}$ of **A**$_{\textbf{MAP}}$, we originally intended to approximate the posterior by a multidimensional Gaussian distribution. In this case the uncertainties of the components of A are determined by the diagonal elements of the inverse of the Hessian matrix (matrix of second derivatives of $p(\mathbf{A} \mid \mathbf{O}=\mathbf{O_{MAP}}, \mathbf{I_1}, \mathbf{I_2})$ with respect to the components of **A**) at (**A**,**O**)=(**A**$_{\textbf{MAP}}$,**O**$_{\textbf{MAP}}$):

$$\boldsymbol{\sigma}_{\textbf{est}} = 1 \Bigg/ \sqrt{-diag\left[inv\left(\frac{\partial^2 p(\mathbf{A},\mathbf{O} \mid \mathbf{I_1},\mathbf{I_2})}{\partial(\mathbf{A},\mathbf{O})^2} \right) \right]}$$

Eq. 6-29

However, since the Hessian has one row and one column for each component of **A** and **O**, it is impractical to calculate its inverse given the large number of values in **O**. We, therefore, made the additional assumption that the uncertainties on the components of **A** do not correlate with any component of **O**. This allows using the Hessian of the profile posterior instead of the posterior, leading to the approximation

$$\boldsymbol{\sigma}_{\textbf{est}} = 1 \Bigg/ \sqrt{-diag\left[inv\left(\frac{\partial^2 p(\mathbf{A} \mid \mathbf{O}=\mathbf{O_{MAP}}, \mathbf{I_1},\mathbf{I_2})}{\partial \mathbf{A}^2} \right) \right]}$$

Eq. 6-30

Since this expression neglects correlations of the uncertainty in the estimated parameters with those in the dimensions that are profiled out, σ_{est} is only a lower bound for the uncertainty of the aberration coefficients. See below for a comparison between our uncertainty estimate σ_{est} and the actual standard deviation σ_{act} of aberration estimates for simulated image pairs.

Algebraic manipulations were aided by Mathematica 6 (Wolfram Research). In particular, the profile posterior and its first derivative, as well as the first derivative of the *MTF*s, all needed

for minimize.m, were calculated using Mathematica (see the appendix, chapter 9.2). For the Gaussian *MTF*, the results were then hand-coded into a C routine, and compiled into a .mex dynamic link library (DLL) for use in MATLAB R2010a (MathWorks). To speed up the calculation of profile posterior (Eq. 6-27) and its derivative when using the Gaussian *MTF* (Eq. 6-5) the SSE2 processor instruction set was used for fast calculation of exponential functions (Pommier, 2008). For the Bessel-*MTF*, the equations were directly exported from Mathematica to MATLAB .m code. For simplicity and speed, the Gaussian *MTF* model (Eq. 6-5) was used during the creation and analysis of all simulated image pairs. Experimental image pairs were analyzed using the Gaussian *MTF* or Bessel-*MTF* (Eq. 6-4) as described in the Results section.

To avoid problems caused by lateral shifts between the images of an experimental image pair, images were registered to a precision of 0.01 pixels by cross-correlation (Guizar-Sicairos, et al., 2008; Guizar, 2008). To account for the non-periodicity of the imaged region, the images were then Hann-filtered (Blackman & Tukey, 1959) before being fed into the posterior maximization algorithm.

6.2.3 Experiments

All SEM images were taken using a FE-SEM (Merlin, Carl Zeiss) at 5 keV landing energy, a beam current of either 1 nA or 190 pA and a working distance of 10 mm or 3 mm, which resulted in *NA* values of around 5 and 6.8 mrad, respectively. The biological sample was a cross-sectional surface through a full mouse brain, smoothed on a microtome, and coated with about 2 nm of carbon-platinum to make it conductive. The sample was prepared according to (Mikula et al., in preparation). The biological sample was typically imaged with 80 nm pixel size, a 1024x768 pixel field of view, and 400 ns pixel dwell time. For high-resolution imaging, resolution test specimens by Agar Scientific (Essex, England) were used. The gold-on-carbon sample S168 contains particles ranging from roughly 5 to 150 nm in diameter and was used for imaging at 20 and 5 nm pixel sizes, while the tin-on-carbon sample S1937 contained tin spheres from <10 nm to ~50 μm in diameter and was used for imaging at 80 nm or 20 nm pixel size.

Unless otherwise noted, 768x768 pixel (px) regions from each image were Fourier transformed, and only spatial wave vectors $|\mathbf{k}|<0.8$ rad/px (i.e. below 25% of the 1D Nyquist frequency) were used for the analysis.

6.2.4 Simulating image pairs

The high-quality image used as the "object" for all simulations was acquired as follows. After optimizing defocus and astigmatism by using 8 iterations of MAPFoSt, a series of 4 images with 1.6 µs pixel dwell time was acquired using the same field of view and averaged, corresponding to a total pixel dwell time of 6.4 µs (Figure 6-1a). The radially averaged Fourier spectrum of this image shows that even the highest image frequencies were not dominated by noise (Figure 6-1g).

Using this image as the object, **O**, sample image pairs with a range of different aberrations and different amounts of added Gaussian white noise were generated, using Eq. 6-5, Eq. 6-8 and Eq. 6-9. These simulated images allowed us to test MAPFoSt's performance under conditions where the *MTF* is known exactly and the noise on each pixel had been sampled from a Gaussian distribution.

6.3   Results

Our goal was to estimate the correct focus and astigmatism parameters while minimizing the exposure of the sample to incident radiation. The need to combine all available information suggests the use of a Bayesian or maximum-likelihood framework. We therefore based MAPFoSt on the phase-diversity concept (Gonsalves, 1982; Paxman, et al., 1992). We found that at least in the limit of ray optics and when only defocus and astigmatism need to be estimated, such as in a scanning electron microscope (SEM), a computationally very efficient implementation is possible because then the modulation transfer function (*MTF*) can be expressed explicitly in terms of the aberration parameters. Unlike the original implementation of phase diversity (Gonsalves, 1982; Paxman, et al., 1992), which requires four Fourier transforms (FT) per image at each step of the maximization procedure (Paxman, et al., 1992), our implementation (Eq. 6-4 or Eq. 6-5 and Eq. 6-27) requires only one FT per image for the whole maximization procedure. For example, for the image pair in Figure 6-2a, 2 FTs were used, followed by 64 linear-time maximization steps, while their implementation would have required 512 FTs.

The high-dimensional posterior is numerically intractable, but can be maximized analytically with respect to the many dimensions corresponding to the spatial frequencies of the object, as long as the object prior has a suitable form. The resulting posterior profile is a function of

defocus and astigmatism. As a function of the defocus at the optimal astigmatism values, the posterior profile for our example shows a narrow and smooth peak (Figure 6-3).

6.3.1 Simulations show bias-free aberration estimation

For all simulations we used the same virtually-noise-free SEM image as the object and changed it by simulating the effect of aberrations and added Gaussian noise. To generate an image pair that could then be fed to MAPFoSt, the desired aberrations in all three modes (focus and both astigmatism directions) were imposed onto the object together with the positive or negative defocus used as test aberration, before adding noise to each image.

We evaluated the performance of MAPFoSt, by first varying defocus while keeping the astigmatism constant (Figure 6-4a), and then by varying astigmatism at zero defocus (Figure 6-4b). In both cases the MAPFoSt produced estimates with no noticeable bias but decreasing precision as aberrations got larger.

The estimation error depends inversely on total dose

Electron-microscope images are typically dominated by shot noise, which follows a Poisson distribution. If the contrast is limited (as is common for biological samples) and the number of electrons per pixel is not too small, a Gaussian noise model can be used, with the noise variance proportional to the average number of detected electrons per pixel. Simulations for different signal-to-noise ratios (SNR) were, therefore, performed to understand how the performance of MAPFoSt behaves as the dose per pixel is varied.

To quantify the aberration estimation error, a set of 30 image pairs with a fixed SNR of 0.87 and a size of 256x256 pixels was generated by simulation and fed to MAPFoSt. Each image pair contained aberrations in all three modes, drawn from a uniform distribution in the range of ±15 µm. The resulting aberration estimates varied around the true values by 3.6 µm (standard deviation, σ_{act}), the same amount for each mode, but showed no bias (Figure 6-5a). At SNRs of 2.2 (Figure 6-5b) and 220 (Figure 6-5c) σ_{act} was smaller by factors of 8.3 and 248, respectively. Further simulations with different SNRs, in the range from 0.1 to 220, revealed that σ_{act} varied in inverse proportion to the SNR for SNRs larger than 5.5 (Figure 6-5d, open circles). For SNRs between 1.0 and 5.5, the simulation error starts to increase more quickly than the noise (Figure 6-5d).
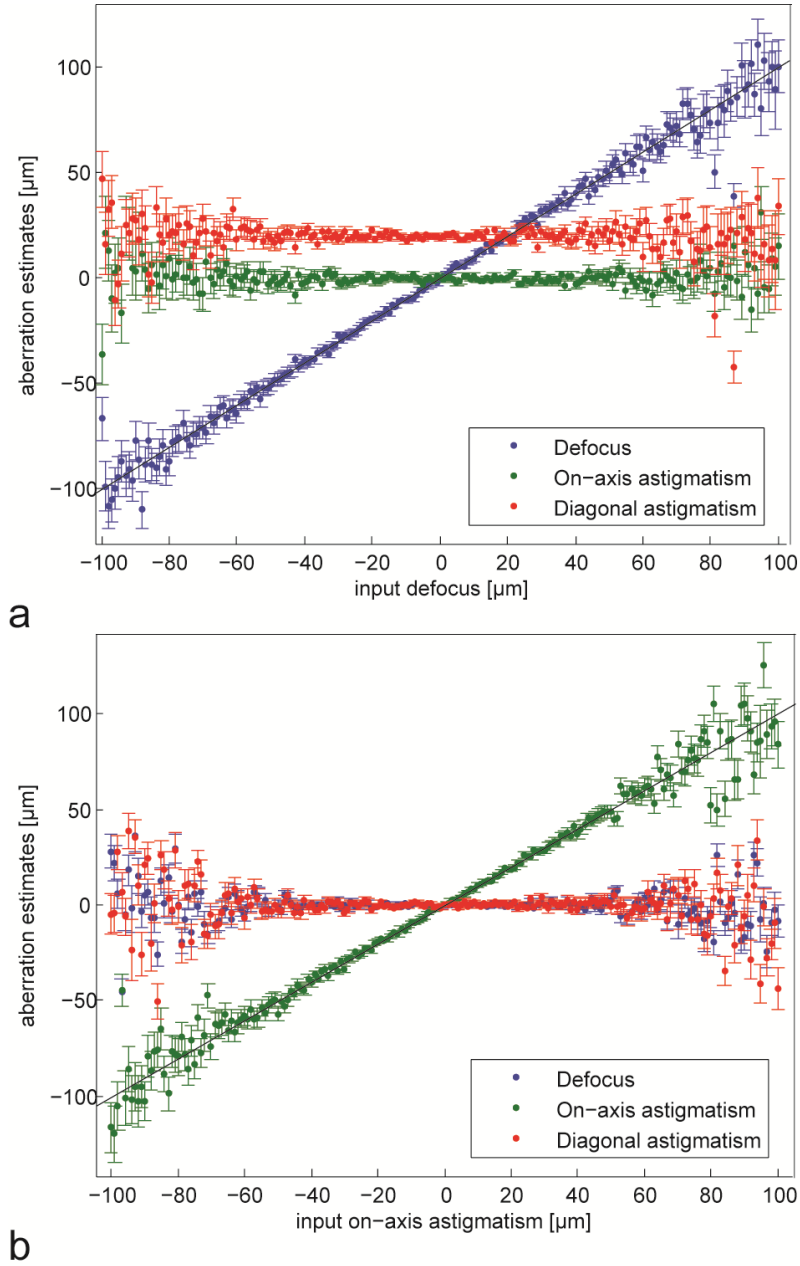
Figure 6-4. MAPFoSt aberration estimates for simulated image pairs. a) Focus is varied at constant astigmatism and b) on-axis astigmatism is varied at constant defocus and constant diagonal astigmatism.

We also calculated the predicted error based on the curvature of the profile posterior (Eq. 6-30, Figure 6-5d, solid circles). In contrast to the actual error discussed above, the predicted error can be calculated directly from the images, without knowing the true aberrations. For SNRs above 5, the predicted error for the astigmatism is close to the actual error, but for the defocus it is too small by roughly 50%.

We varied the image size between 4x4 and 768x768 pixels, while keeping the total dose constant. We found that the aberration-estimation error varied in a narrow range (Figure 6-5f) as the dose per pixel was varied almost 40000 fold.
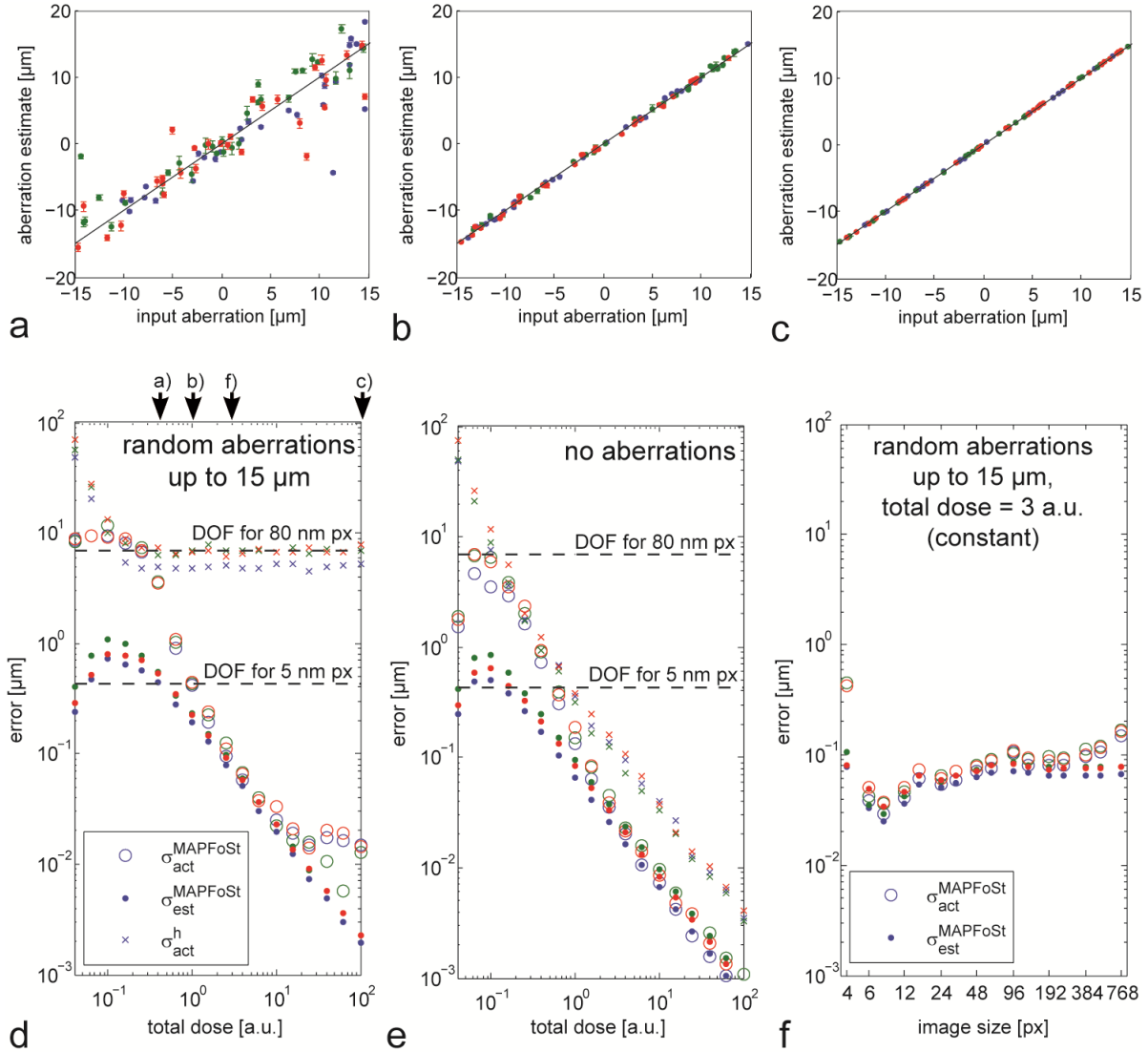
Figure 6-5. Estimation accuracy for simulated image pairs. Aberration estimates for SNRs of a): 0.86, b): 2.2 and c): 220, determined for 30 simulated image pairs (256x256 pixel) containing actual aberrations in all three modes (randomly drawn from a uniform distribution in the range ±15μm). d) Estimation error (standard deviation) in each mode as a function of the total dose used in the images, for N=30 simulated image pairs containing random aberrations at each SNR; errors predicted from the curvature of the MAPFoSt profile posterior (small full circles) are compared to the actual errors from the MAPFoSt algorithm (empty circles) and from a heuristic algorithm (crosses). e) Like d) but with all image pairs containing zero aberrations. For reference, the depth of field (DOF) for the actual pixel size of 80 nm and a pixel size of 5 nm are shown as the dashed line in d) and e).

f) Estimation error in each mode as a function of the image size for constant total dose, i.e. varying dose per pixel. Color code for all subfigures: blue=defocus, green=on-axis astigmatism, red=diagonal astigmatism.

A Heuristic Algorithm

For comparison, the same image pairs were also analyzed with a heuristic focus-and-stigmation algorithm, used in (Briggman, et al., 2011). This algorithm also uses information from a pair of large images acquired at two different defocus settings but, unlike MAPFoSt, does not make use of the fact that the object is the same for both images but does assume the spatial-frequency spectra to be very similar. For a full description of this algorithm see the appendix (chapter 9.3). We applied the algorithm to the same simulated test images that were used to evaluate MAPFoSt and found that at very low SNRs the estimation error, σ_h, (Figure 6-5d, symbol x) quickly falls with increasing SNR but levels off at a SNR of 0.25 remaining at around σ_h=5 µm for defocus and σ_h=6-8 µm for astigmatism, which is close to the depth of focus of 8 µm, expected for 80 nm pixels at an NA of 0.005. This leveling-off is caused by the algorithm mistaking defocus as a sum of defocus and astigmatism, and vice versa (data not shown). However, the heuristic algorithm does determine with a precision that varies with the SNR similarly to MAPFoSt the point of vanishing aberrations (Figure 6-5e). It should be noted that the scaling of the heuristic algorithm's aberration estimates depends strongly on the image content. The scaling used here was determined from a least-squares fit at SNR 220.

The optimal test aberration

The choice of test aberration is crucial for the performance of any phase-diversity algorithm (Lee, et al., 1999; Meynadier, et al., 1999; Dean & Bowers, 2003; Dolne, et al., 2003). The mode used as test aberration needs to "cross react" with all the modes to be estimated, which means that the mixed second derivatives of the *MTF* with respect to the test aberration and each of the other modes must be non-zero. In other words, changing the test aberration must modulate how strongly each of the other aberrations affects the image quality. While recent work (Dolne, 2011) suggests that astigmatism is a viable test aberration under certain conditions, we found that defocus is the only test aberration that allows co-estimation of both astigmatism modes, since cross-terms $a_{on\text{-}axis}z$ and $a_{diag}z$ exist in the *MTF* (Eq. 6-4, Eq. 6-5). If one of the astigmatism modes was used as test aberration, that mode and defocus could be estimated (data not shown). The other astigmatism mode could, however, not be separated from the object structure, due to the lack of an interaction term $a_{on\text{-}axis}a_{diag}$.

One would expect that making the test aberration (added for one and subtracted for the other image) too small would make aberration estimation difficult, because the two test images taken hardly differ. Conversely, if the test aberration is too large, the images will be overly blurred and contain little information at high spatial frequencies, which again would make aberration estimation imprecise.

To find the test aberration that is best in theory, we return to our example with a single spatial wave vector, and one aberration mode (defocus). Combining Eq. 6-5, Eq. 6-26 and Eq. 6-30 allows the estimation of the aberration uncertainty σ_{est} as a function of the actual aberration $\tilde{A}$, the spatial wave vector k, and the test-aberration strength T:

$$\sigma_{est}\left(\tilde{A},k,T\right) = \frac{1}{SNR} \frac{\sqrt{8}\exp\left(\frac{1}{8}k^2 NA^2 (T-\tilde{A})^2\right)\sqrt{1+\exp\left(k^2 NA^2 T\,\tilde{A}\right)}}{k^2 NA^2 |T|}$$

Eq. 6-31

Here σ_{est} is calculated from the curvature of the posterior profile at its peak, as described in chapter 6.2.2. σ_{est} is inversely proportional to the SNR, confirming the simulation results (Figure 6-5d/e). For $T \ll k\,NA$, σ_{est} scales as $1/T$, while for $T \gg k\,NA$ the term $\exp\left(\frac{1}{8}k^2 NA^2 T^2\right)$ becomes dominant (Figure 6-6a). Between those extremes there is a single minimum, the position of which depends strongly on k.

Particularly for large k, the scale of σ_{est} and the position of its minimum also depend strongly on $\tilde{A}$. The reason is that for larger actual aberrations, $\tilde{A}$, adding a large test aberration can push the signal in one or both of the images into the noise, which can be avoided by using smaller test aberrations (Figure 6-6a, left set of curves).

Choosing the size of the test aberration is, therefore, always a compromise between the performance at different spatial frequencies. To determine the test aberration that is optimal when using the whole spectrum of wave vectors, we simulated image pairs with different fixed aberrations (0, 5, 10 or 15 μm defocus, or 5 μm astigmatism), using different test aberrations from 4 to 60 μm ($N=50$ image pairs for each condition). The resulting actual estimation error σ_{act} (Figure 6-6b) shows that $13 < T < 16$ μm defocus is a good compromise for these cases. Note that image pairs taken at 5 μm defocus plus/minus test defocus can tolerate much larger test aberration sizes than image pairs taken at 5 μm astigmatism

plus/minus test defocus. This may be due to the fact that defocus is compensated by the test aberration in one of the two test images in the first case, resulting in one weakly aberrated and one strongly aberrated image, whereas for astigmatism both images are strongly aberrated.
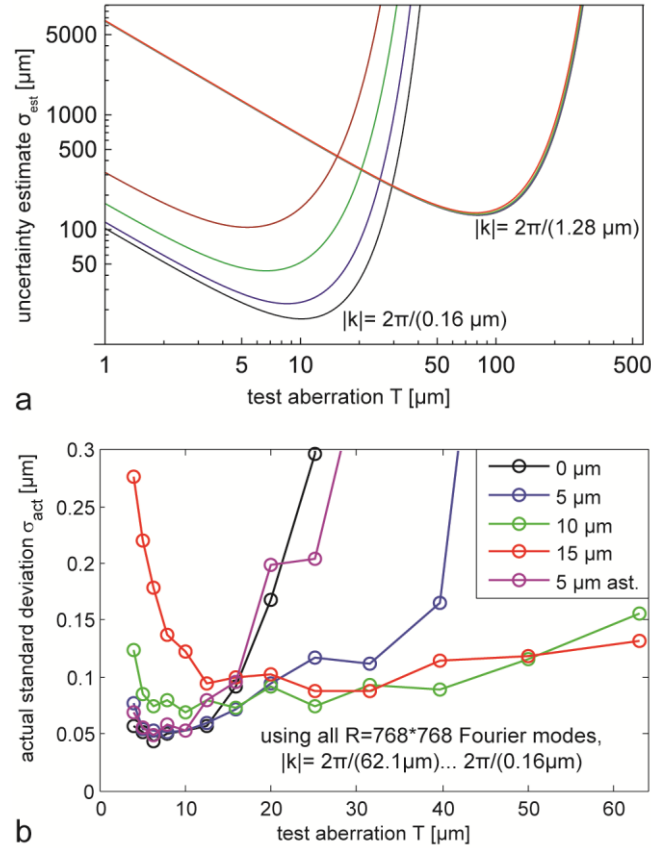
Figure 6-6. The precision of the aberration estimation as a function of test-aberration size a) for two separate spatial frequencies (λ=0.16μm, left and λ=1.28μm, right), at unit SNR, for different actual aberrations Ã = 0 μm (black), 5 μm (blue), 10 μm (green) and 15μm (red). b) Actual aberration estimation error σ_{act} as a function of test aberration size; simulated image pairs analyzed using all spatial frequencies; SNR=1, image size=768x768px, N=50 noise realizations each.

6.3.2 SEM imaging experiments

MTF shape and defocus estimation

To determine whether MAPFoSt provides a reliable estimate of the aberration parameters in a real electron microscope, a series of images was acquired while the defocus was varied from -100 μm to $+100$ μm.

We analyzed these images using MAPFoSt, using at first a Gaussian *MTF* (Figure 6-7a). We found that MAPFoSt's estimates varied linearly with one slope up to a defocus of ± 20 μm, switching to an increased slope beyond that (Figure 6-7a. Note that the scaling for the estimate was arbitrary since the NA of the electron microscope was at this point unknown). Given that the electron beam is shaped by a hard aperture, we suspected as the reason for this nonlinearity that the Gaussian *MTF* does not well describe the situation. In fact, we found that a Bessel *MTF*, which is appropriate for a top-hat beam, describes the *MTF*'s defocus dependence much better across spatial frequencies. We therefore re-analyzed the same data set using a Bessel *MTF* model for MAPFoSt and found good linearity over the full defocus range tested (Figure 6-7b).

From the slope of the aberration estimate versus actual defocus plot, the numerical aperture of the electron microscope, which depends on imaging parameters such as the beam current and the working distance, can be determined (NA was around 5 mrad for the settings used here).

There was a small amount of crosstalk between defocus and astigmatism estimates (0.02 and 0.006 μm astigmatism per μm defocus, Figure 6-7b, upper inset). Independent astigmatism measurements using modal sensing either in focus or at $\pm$ 80 μm defocus indicated that this is not an artifact of MAPFoSt aberration estimation, but reflects the change in optimal astigmatism parameters with working distance in our electron microscope.

Astigmatism estimation

A property of magnetic lenses is that, as the lens current is changed to adjust the working distance, the coordinate system for stigmation rotates with respect to the scanning axes. Furthermore, unlike the working distance (or defocus) for which the microscope manufacturers provide calibration in microns, the stigmator settings are often in internal units such as percent of the maximal values. In order to use the MAPFoSt estimates to adjust the

microscope settings, stigmator scaling and rotation angle have to be known. We determined them using several series of measurements during which astigmatism and defocus parameters were varied.

At first a through-focus series was acquired with x and y stigmators set to 1% and 0%, respectively (Figure 6-7c). As expected, the MAPFoSt astigmatism estimate was nearly constant. Conversely, a linear variation of the x astigmatism at a nominal defocus of zero resulted in linearly varying estimates for both on-axis and diagonal astigmatism (Figure 6-7d).

Together with similar measurements these data allow the determination of a general transformation matrix linking the astigmatism in instrument units ("astigmatism x", "astigmatism y") to that expressed in microns and referenced to the scan frame orientation ("diagonal astigmatism", "on-axis astigmatism").
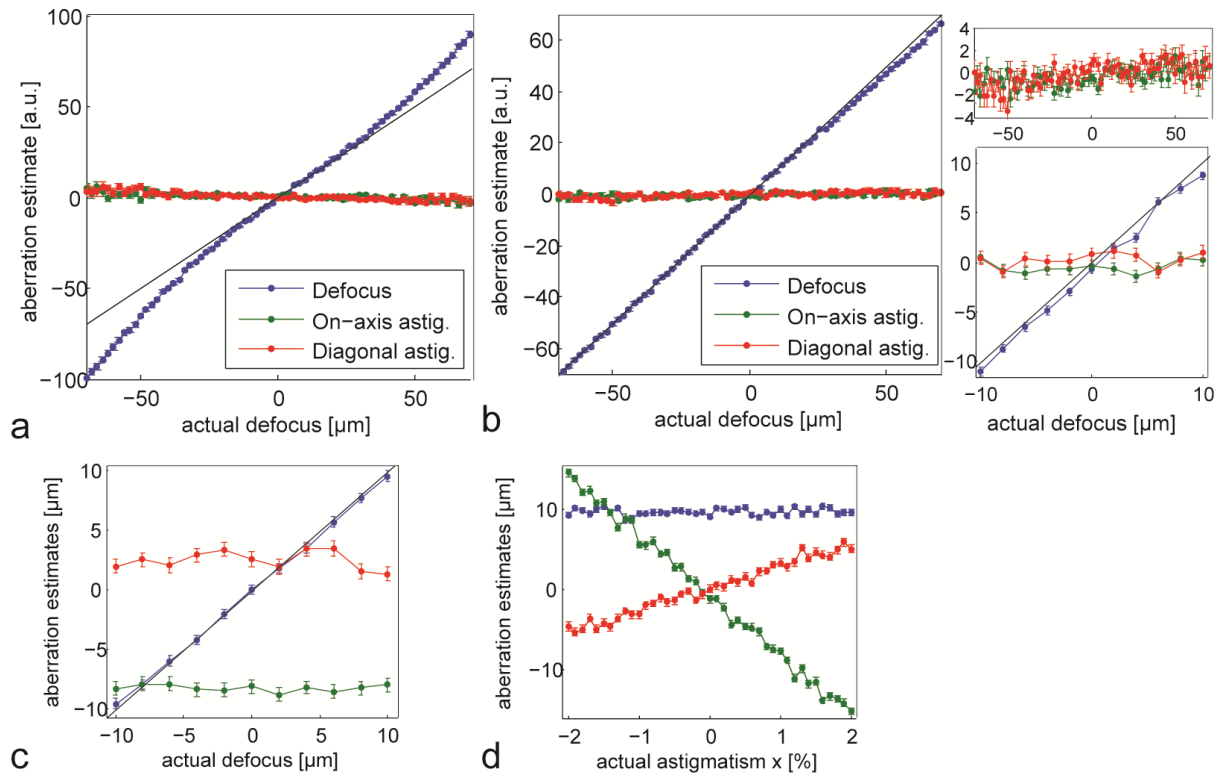
Figure 6-7. MAPFoSt aberration estimates for experimental image pairs. a) Focus is varied at zero astigmatism, analysis assumes Gaussian MTF*; b) images from a) re-analyzed assuming Bessel* MTF*; c) focus is varied at fixed astigmatism x of 1%; d) astigmatism x is varied at a fixed defocus of ~10 μm. All images had 768x768 pixels and were acquired with 400 ns pixel dwell time. The SNRs were 1.17 and 1.44 at 100 μm and 0 μm defocus, respectively.*

Limiting the spatial frequency range

We repeated the MAPFoSt analysis of the defocus series (Figure 6-7a) with different amounts of test defocus (i.e. taking images with different focus differences from the through-focus series) and using different spatial frequency ranges.

While the results were satisfactory when using all spatial frequencies (Figure 6-8d), we found a slightly increased precision when limiting the range of spatial frequencies, with the best results achieved when using only spatial frequencies below 25% of the Nyquist frequency (Figure 6-8b), in combination with test aberrations of about 30 μm defocus.
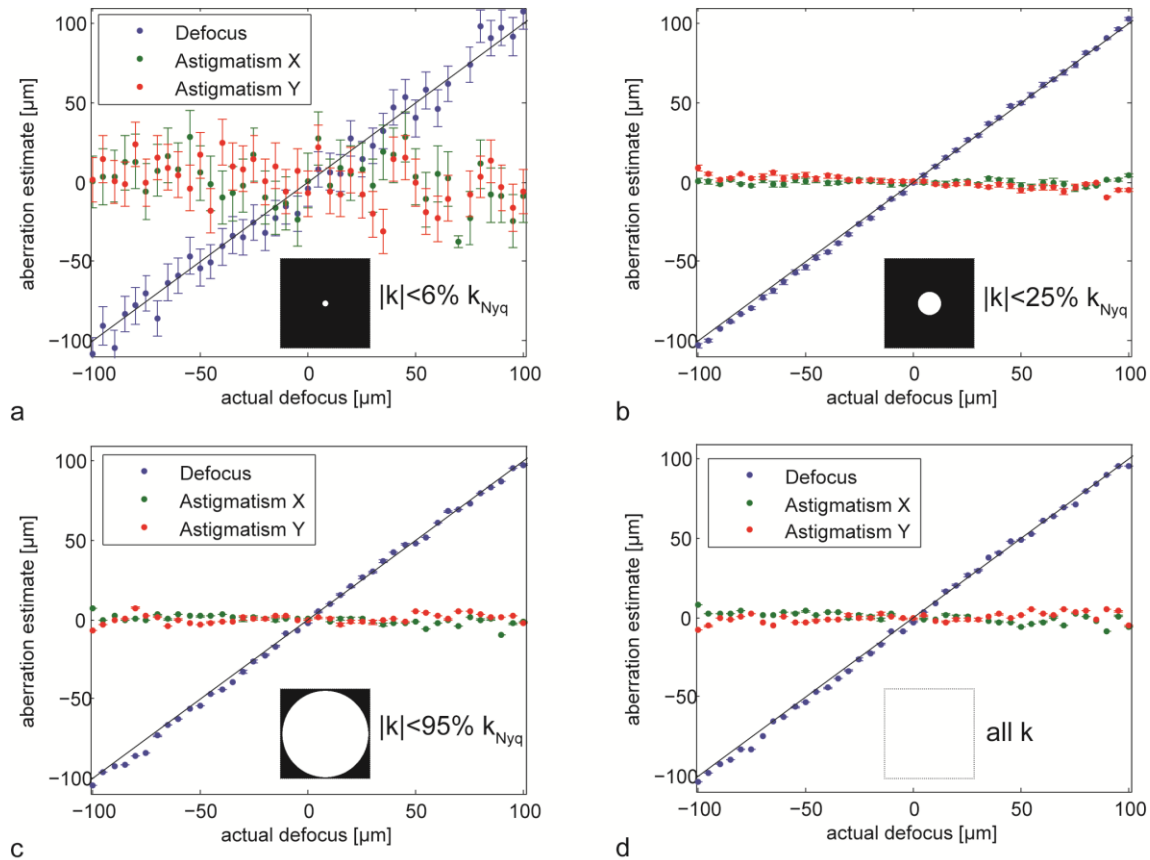
Figure 6-8. Influence of the spatial frequency range used in MAPFoSt analysis. A given through-focus series of experimental images analyzed using a) spatial frequencies $|\mathbf{k}|<0.06$ k_{Nyq}, b) $|\mathbf{k}|<0.25$ k_{Nyq}, c) $|\mathbf{k}|<0.95$ k_{Nyq}, d) all spatial frequencies

When including the higher spatial frequencies in the analysis with the Bessel *MTF*, the posterior has many local maxima; to avoid the maximization procedure getting stuck in such a local maximum, the maximum was first determined using a reduced spatial frequency range where local maxima are absent. This maximum was then used as a starting point for the subsequent run with increased range.

Estimation with no free parameters

One feature of MAPFoSt is that unlike the heuristic algorithm, for example, the scaling parameters for defocus and astigmatism estimates should depend only on the microscope settings but not on the sample. We tested this by first determining the scaling parameters independently (of MAPFoSt) and then verifying if this resulted in correctly scaled MAPFoSt aberration estimates. For these experiments, we used a working distance of 3 mm and the crossover-free mode of the SEM.

To independently estimate the numerical aperture, a high signal-to-noise in-focus image of our biological sample (see below) and a defocused image of the same region were used to calculate the Bayesian estimate of the angularly averaged *MTF* for the defocused image. This *MTF* was then visually compared with a Bessel *MTF* (Eq. 6-4), while varying the NA parameter therein until agreement of both *MTF*s was reached, at 6.78 mrad.

Inspecting the Fourier spectrum of an image taken with significant defocus and one stigmation parameter set to a large value yielded the angle between the scan frame and the SEM's coordinate systems for stigmation. We then determined the astigmatism scaling from the distance between the two line foci for a given stigmation setting. Because visual inspection proved too imprecise, we tested different metrics which were expected to have maxima at the line foci. Using a maximum-likelihood-based metric (exploiting the now-known orientation of the line focus and using an aberration-free reference image) provided the most reliable estimate (1.65 %/µm at 3.0 mm working distance, 5 keV landing energy).

The thus determined scaling parameters agree well with the MAPFoSt-derived NA and stigmator-rotation angle for five test cases (see details below), while the MAPFoSt-derived astigmatism scaling was systematically larger (Table 6-1). This systematic discrepancy likely stems from an imprecise measurement of the distance between the two line foci.

The MAPFoSt astigmatism scalings for the different test cases vary by up to 8% (Table 6-1), except for one outlier (test case 1). For the latter, we later found that initial defocus reached values of 75 µm, roughly a factor 4 larger than intended. When excluding data points taken at more than 20 µm defocus the astigmatism scaling is in the same range found for the other test cases. This implies that MAPFoSt astigmatism estimates are super-linear when strong defocus is present.

Table 6-1. Scaling and rotation parameters for the different test cases described in the text. Tabulated values are for MAPFoSt, relative to the independently determined values. Errors correspond to 95% confidence intervals.

Test case	Relative NA	Astig. rotation	Astig. scaling
1. Brain, 80 nm px	1.00 ± 0.01	-1.1°	1.48 ± 0.04
Ditto, excluding z>20μm	0.97 ± 0.13	-0.8°	1.20 ± 0.02
2. Brain, 20 nm px	0.85 ± 0.14	0.5°	1.19 ± 0.01
3. Tin-on-carbon	1.07 ± 0.08	0.3°	1.23 ± 0.02
4. Gold-on-carbon	1.04 ± 0.02	-0.1°	1.28 ± 0.02
5. Gold-on-carbon	1.01 ± 0.01	0.1°	1.27 ± 0.01

MAPFoSt convergence

One of our goals was to arrive at correct correction parameters exposing the sample to as low a dose as possible. It is therefore important to minimize the number of iterations. The residual aberration after a single iteration (taking the image pair, applying MAPFoSt, adjusting working distance and astigmatism) depends on the precision of the aberration estimates, which in turn depends on knowing the calibration constants.

To test how quickly the procedures converge for novel samples we performed the following on four test cases, involving three different samples and two different pixel sizes. In each case, we added different amounts of defocus and astigmatism relative to the previously determined best settings before taking the image pair needed for MAPFoSt. The algorithm inferred the aberration parameters using these images and adjusted the microscope settings accordingly. Up to five iterations were performed to explore the settling behavior of the algorithm. To verify how close the MAPFoSt aberration estimate after the fifth iteration came to the true aberrations present, a modal optimization (chapter 9.4) of all three modes was performed, concluding the test procedure.

Whole-brain block-face imaging

The first two test cases involved aberration estimation for tiled bock-face imaging of a cross section through a mouse brain stained in its entirety (Mikula et al., in preparation) and cut on an ultramicrotome. The resulting block face varies in focus so much that every tile needs to be

separately focused, but the use of the built-in autofocus results in burned-in regions that mar the final images taken (data not shown). Across the surface of the sample, the contrast varies from tile to tile and often within a tile, providing highly variable conditions for any autofocus. On this sample, the test procedure was performed at 80 nm (Figure 6-9a) and 20 nm (Figure 6-9b) pixel size at 27 different lateral positions. For each position, the initial astigmatism values for the 80-nm-pixel test case were independently drawn from a normal distribution with standard deviation of 15 µm. Due to the curvature of the sample surface, the initial defocus varied between 5 and 75 µm. For the 20-nm-pixel test case, we used as the starting aberrations the aberrations that remained after the first iteration of MAPFoSt to the 80 nm image, where the defocus and astigmatism values varied by 1.9 µm and 9.7 µm (standard deviation), respectively.

In these two test cases, the modal optimization was started from the result of the first iteration of MAPFoSt at 20 nm resolution. In 6 of the 27 lateral positions, these initial aberrations were too strong and modal wavefront sensing failed, either by converging instead onto a line focus (at which point astigmatism and defocus have the same, non-zero value) or because the optimal focus lay outside the parameter region searched. As a result, no independent determination of the true aberrations was available for these 6 lateral positions. Consequently, these regions had to be excluded from further analysis, even though visual inspection of their MAPFoSt images indicated good convergence after the second or third iteration.

For each of the remaining 21 lateral positions, one iteration of MAPFoSt at either 80 nm or 20nm pixel size decreased aberrations by roughly a factor of 4 until the final precision was reached, which took never more than three iterations (Figure 6-10a&b). For 80 nm pixel size, the final precision corresponded to focal spot sizes between 2 and 50 nm; for 20 nm pixel size it was between 2 and 20 nm.

Initial defocus estimates were sometimes imprecise, especially when strong astigmatism was present. However, the total aberration after each correction step was always reduced, since increases in defocus were always overcompensated by decreases in astigmatism, or vice versa. Defocus estimates were found to be correctly scaled, but astigmatism estimates were found to be consistently too high, slightly overshooting in each correction step (Table 6-1).

In a separate experiment on the same sample, the dose efficiency of MAPFoSt was analyzed by inferring the absolute dose from the level of Poisson noise. All three aberration

coefficients could be estimated to within <7% of the depth of focus, using 768x768 pixel images with an incident electron dose density of 2500 electrons/pixel resulting in 19 detected secondary electrons per pixel (uncorrected estimate from the variance) and a SNR of 1.01.
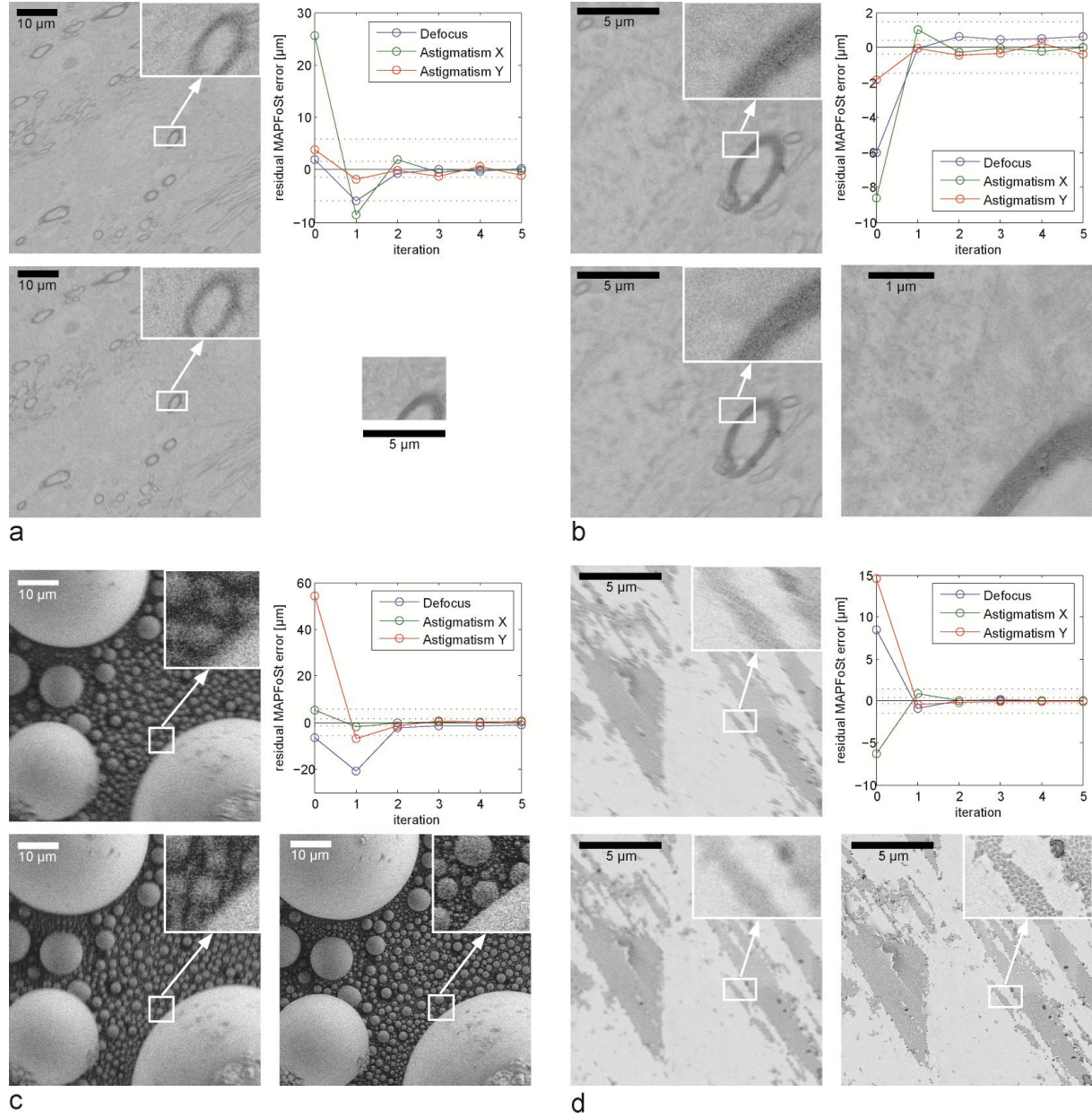
Figure 6-9. Performance of 5-iteration MAPFoSt for different test cases. Estimation in the first iteration was based on the two 768x768 pixel images shown on the left; the right image shows image quality after the fifth iteration. For a) and b), the right image was taken at 5 nm pixel size and is shown in the same scale as the insets on the left. The plots show the initial aberrations (0th iteration) as well as the residual aberrations after 1 to 5 iterations of MAPFoSt in all three aberration modes.

Figure 6-10. Initial focal spot size and spot size achieved by MAPFoSt after up to five iterations. a) Mouse brain sample imaged at 80 nm pixel size and b) 20 nm pixel size. c) Tin-on-carbon resolution target imaged at 80 nm pixel size. d) Gold-on-carbon resolution target, analyzed using improved astigmatism scaling for faster convergence.

Focusing on resolution targets

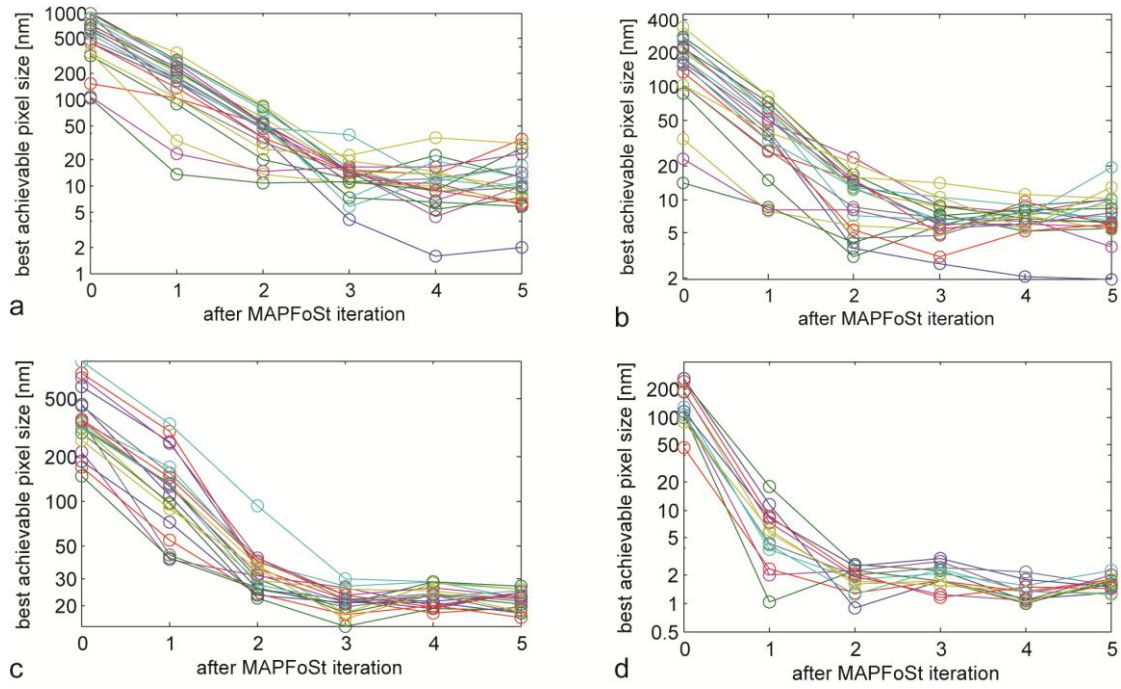For the third test case, we used a tin-on-carbon resolution target featuring spheres from several nanometers to tens of micrometers in diameter, giving the sample a three-dimensional structure. The test procedure was run using a pixel size of 80 nm (Figure 6-9c) and repeated 20 times using the same region of the sample. Initial defocus and astigmatism values for the 80-nm-pixel test case were independently drawn from a normal distribution with standard deviation of 15 μm. One or two iterations of MAPFoSt were sufficient to reach the final precision, which was between 10 and 30 nm spot size; only in one case, notably the one with the largest aberrations, a third iteration of MAPFoSt was needed to reach 30 nm spot size (Figure 6-10c). Each iteration reduced the aberrations by roughly a factor of three.

For the fourth test case, we used a gold-on-carbon resolution target with feature sizes between 5 and 150 nanometers. The test procedure was repeated 20 times each on three different sample regions, for a total of 60 different initial aberrations drawn from a normal distribution with standard deviation of 5 μm. Each MAPFoSt iteration reduced aberrations by a factor of about 4; two iterations were needed to reduce aberrations enough to reach a spot size of below

20 nm, and a final spot size of below 7 nm was reached after the third iteration (Figure 6-11). It was noted that a nonlinearity in the sample z stage used for inducing test aberrations created a small defocus bias, which was a limiting factor. Defocus and astigmatism estimates were on average too large by factors of 1.04 ± 0.02 and 1.28 ± 0.02, respectively (Table 6-1).
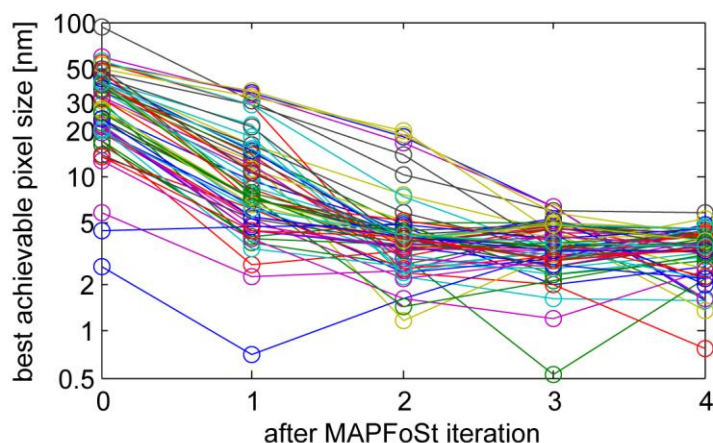

Figure 6-11. Initial focal spot size and spot size achieved by MAPFoSt on a gold-on-carbon resolution target using 20 nm pixel size, analyzed using the independently-determined astigmatism scaling.

To show the speed and quality of convergence when the astigmatism scaling is correct, the previous experiment was repeated with the astigmatism scaling reduced by said factor of 1.28. Test aberrations were created by changing the SEM working distance to avoid the nonlinearity in the z stage. To make sure the image also contained lower spatial frequencies, below the characteristic size of the gold structures on the sample, a region of the sample where the gold features covered only about 28% of the field of view was used (Figure 6-9d). The test procedure was repeated 13 times with different initial aberrations drawn from a normal distribution with standard deviation of 5 μm, always using the same sample region.

In this fifth case, one iteration of MAPFoSt was sufficient to reduce aberrations by a factor between 12 and 100, resulting in spot sizes between 1 and 20 nm. A projected final spot size of 1-3 nm was reached after only two iterations (Figure 6-10d), as judged by the results of modal wavefront sensing, which was performed with a pixel size of 5 nm. In other words, even though the actual pixel size of the images analyzed by MAPFoSt was 20 nm, the achievable spot size after just two iterations was much smaller.

Comparison with the built-in autofocus

For our biological sample, the built-in autofocus-and-stigmation routine "Focus+Stig" of the SEM (Zeiss SmartSEM software) often introduced as much as 30 µm astigmatism, even when started from a well stigmated image (data not shown) and was thus unusable for our sample and dosage requirements. Therefore, we only compared MAPFoSt to the built-in "Fine Focus" (SmartSEM), in situations where defocus but no astigmatism was present. Focusing was considered to have failed if the residual defocus exceeded the depth of focus, which is equivalent to saying that the final focal spot diameter exceeded the pixel size.

For 80 nm pixel size and initial defocus values between −25 and 25 µm, the focus estimate provided by the built-in autofocus routine deviated from the correct value by up to 11 µm, with a standard deviation σ_{act}= 4.5 µm. Focus estimates as a function of initial defocus followed a staircase pattern, leading to estimation errors with a saw tooth pattern (Figure 6-12a). For six of 26 initial defocus values, the algorithm brought no improvement, and in one case it even increased defocus. In 23% of all cases, the autofocus failed using the criteria defined in the previous paragraph.

The built-in autofocus routine took between 7.7 and 13 seconds, while continuously scanning the sample. The magnification changed several times to image different sub-regions of the field of view. Imaging at the highest magnification was only performed at the very center of the current field of view, so the final focus quality presumably depended significantly on having good contrast in that area.

For comparison, MAPFoSt is based on two full images, which distributes the dose much more widely across the sample. In the example shown in Figure 6-12a, the two images were acquired using a total scanning time of 2*0.378=0.756 seconds. While total time for one cycle was 8.6±0.2 seconds for MAPFoSt, this was due to the time needed to control the SEM, transfer data, and for computation, all of which could presumably be reduced substantially. MAPFoSt had a maximum defocus error of 4.5 µm, well below the depth of focus, and a standard deviation σ_{act}=1.2 µm for this particular dataset, which was analyzed assuming a Gaussian *MTF*. In summary, MAPFoSt required less than a tenth of the total dose, spread over a larger area, of the built-in algorithm. It was more precise, used much less scan time and slightly less total time.
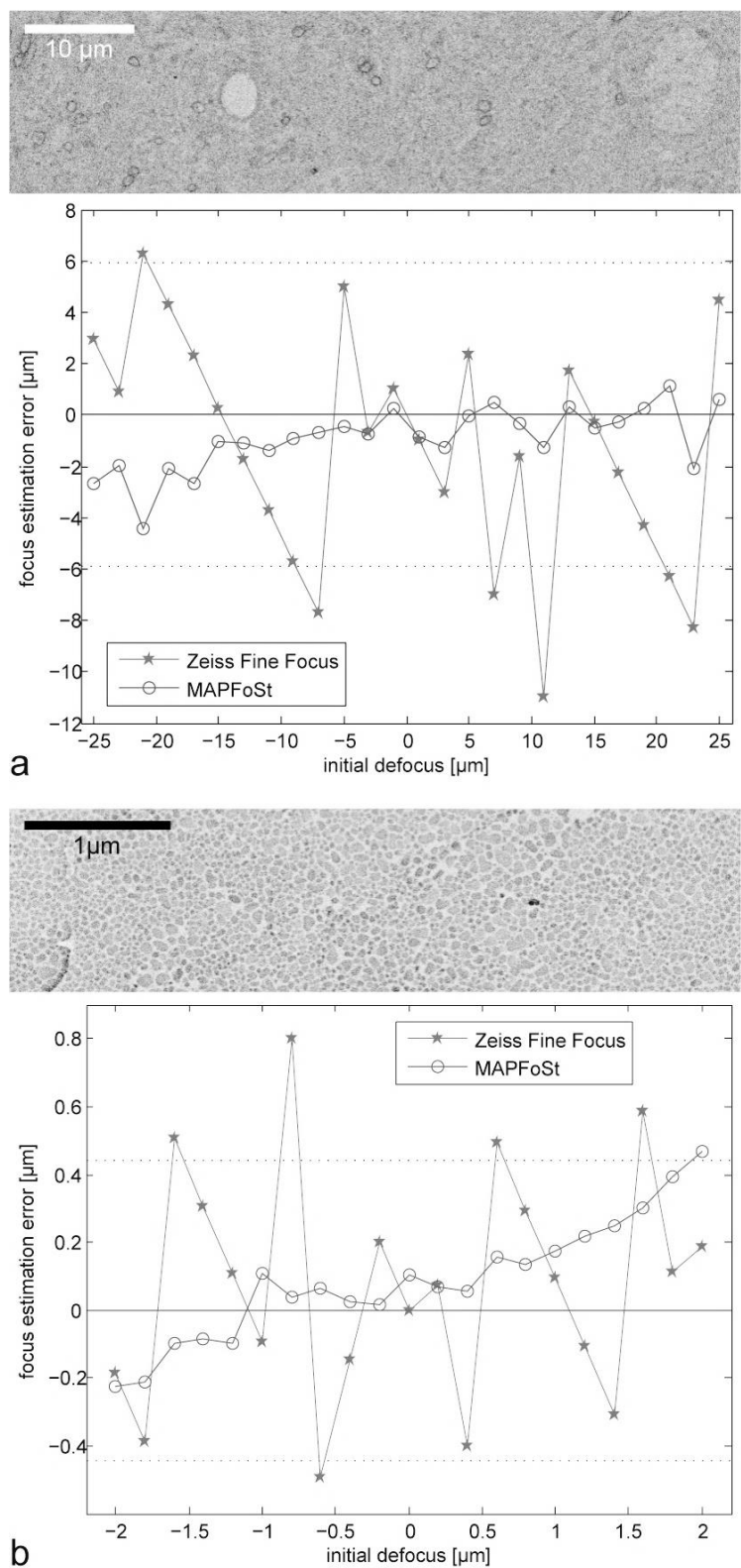
Figure 6-12. Comparing MAPFoSt defocus estimates with the built-in "Fine Focus" routine of the Zeiss Merlin SEM for a range of initial defocus values. a) Biological sample, using 80 nm pixel size; b) gold-on-carbon resolution target, using 6 nm pixel size.

Similar results were achieved with the gold-on-carbon resolution target, where the built-in "Fine Focus" was compared to MAPFoSt at 6 nm pixel size (Figure 6-12b). The built-in autofocus failed in 24% of the cases, while MAPFoSt only failed in one single case (5%). The linear trend of the MAPFoSt focus estimation error (0.15 µm/µm) indicates that the pre-determined NA value used in this analysis was roughly 15% too large with respect to the effective NA at this pixel size. Later tests by a service technician found that the electron microscope column was not in optimal condition, which limited the achievable resolution of the system to 5 nm, decreasing the effect of the small defocus test aberrations used and thereby decreasing the apparent NA.

6.4 Discussion

In this chapter we have shown that maximum-a-posteriori estimation can be used to determine defocus and astigmatism in a scanning electron microscope. Our implementation, MAPFoSt, uses a single pair of images taken at different focus settings and performs more precisely and reliably than the auto-focus routine built into the microscope. Crucially, MAPFoSt uses less than a tenth of the total electron dose, distributed evenly over the imaging area.

In an aberration range twice as large as the depth of focus, the aberration estimates show very good linearity. For defocus alone, the linear range extended over at least 9 times the depth of focus. However, we found the astigmatism estimates to be super-linear when the defocus was more than 2.5 times the depth of focus, causing astigmatism correction to overshoot by roughly 20%. Once aberrations have been reduced to within the linear range, for example by MAPFoSt at a lower magnification, single-step correction of defocus and astigmatism is possible, after acquiring just two test images of the target region (Figure 6-9d, Figure 6-10d). For larger aberrations or sample regions with insufficient contrast, iterative correction always gave satisfactory results.

In practice, true single-step correction requires the precise prior knowledge of one physical parameter (the numerical aperture) and of several calibration parameters (describing the scaling and rotation of the stigmation coordinate system). The NA is dependent on the SEM settings but not on the sample as can be concluded from the fact, that the independently determined value allowed correct MAPFoSt aberration estimation on three different samples and for two different pixel sizes. The same was true for the astigmatism rotation, which varied by less than 1.6° between the different test cases.

The astigmatism scaling turned out to be the most fickle. Fitting MAPFoSt estimates from different samples and pixel sizes gave astigmatism scaling factors that varied by about 8%, as long as the analysis was limited to the linear defocus range. This still allows a sample-independent reduction of the astigmatism by about a factor 12 for each iteration. It is conceivable to use the residual aberration detected during the second iteration to refine the calibration factors and thus accelerate the convergence.

The error in determining the astigmatism scaling (about 25% too big) used in our earlier experiments (test cases 1-4, Figure 6-9a-c) should limit the MAPFoSt convergence rate to a factor of four, close to the factors of four (test cases 1, 2 and 4) or three (test case 3) actually found. Using a MAPFoSt-determined astigmatism scaling, the correction of aberrations corresponding to as much as 12 times the depth of focus was possible in one single step, and residual aberration values corresponding to spot sizes below 1/6 of the pixel size were reached after the second iteration (test case 5, Figure 6-9d, Figure 6-10d). The ability of MAPFoSt to superfocus (reducing the spot size to far below the pixel size) would allow focusing at a lower magnification instead of at the target magnification, for example, spreading of the electron dose over a much larger area.

MAPFoSt is computationally efficient because a closed form of the posterior for the joint distribution of the aberration parameters (defocus and both astigmatisms) and the imaged object can be calculated. Since the maximum-a-posteriori object can be expressed analytically, the profile posterior needs to be maximized numerically in a space with only three dimensions. In contrast to previous work on phase diversity (Gonsalves, 1982; Paxman, et al., 1992), the particular physical model of our imaging system allows the profile posterior to be evaluated without performing several Fourier transforms during each iteration of the numerical maximization procedure. The speed of the algorithm allows the use of large test images with low signal-to-noise ratio, distributing the dose across the sample to minimize damage.

In contrast to modal aberration estimation (Neil, et al., 2000; Débarre, et al., 2009), which requires at least $M=2N+1$ test images to optimize N aberration modes, and in contrast to image-model-agnostic metric optimization techniques such as hill climbing, simulated annealing or genetic algorithms where the number of sample images needed can be even larger, MAPFoSt requires only $M=2$ test images to optimize a number of aberration modes, which we showed for $N=3$.

The heuristic focusing and stigmation algorithm (see chapters 6.3.1 and 9.3) also uses M=2 images and determines N=3 aberration modes using three different metrics. In this regard, it was a step forward compared to methods using only one single metric. However, one drawback of the heuristic algorithm is that the scaling of all three metrics depends on the image content. Once it has been calibrated for one sample the algorithm correctly predicts the size of the aberrations only for other samples with similar Fourier spectra. Modal wavefront sensing does not have this problem, because the M=2N+1 test images allow the determination of the scaling of the metric for each aberration mode (Booth, et al., 2007; Debarre, et al., 2007).

The main reason why MAPFoSt works without scaling problems with a small number of images is that instead of distilling each test image down to one or a few metric values, the full information from all test images enters into the posterior calculation. This allows defocused images to reveal information about other aberration modes such as astigmatism.

If higher-order modes are to be estimated, this does not necessarily require additional images as long as there are more spatial frequencies than aberration modes, but if the cross reaction between the test aberration and these higher order modes is small the estimation accuracy is likely to be low. To retain the speed advantage compared to Paxman et al., it would be important to find a parameterization of these higher-order modes which allows the evaluation of the *MTF* without resorting to Fourier transforms. Eq. 6-28 indicates that, if more than M=2 test images are available the full information from all images can be integrated effortlessly into the posterior. One might even choose the test-aberration size and type for the third and subsequent images dependent on a preliminary analysis of the images already taken. This could include using astigmatism or a mixture of defocus and astigmatism as test aberrations.

The calculation of a posterior includes a determination of the uncertainty for the aberration-parameter estimates. We found that marginalizing the posterior with respect to the object is not a viable alternative when the prior distribution of objects is not well known and that a maximum-a-posteriori approach is preferable. While we used a completely flat prior to analyze the experiments, which is equivalent to a maximum-likelihood approach, Eq. 6-14 with Eq. 6-20 or Eq. 6-24 shows that different priors on the object $\mathbf{O}$, for example a top-hat or a Gaussian prior, can be incorporated, as well as any arbitrary prior on the aberrations $\mathbf{A}$.

Even though MAPFoSt considerably improves low-dose focusing in scanning electron microscopy, a number of open questions and potential improvements are already apparent. First, the Bayesian statistics approach employed should be able to optimally use all information from the different spatial frequencies in the image, which is not quite consistent with our finding that ignoring higher spatial frequencies slightly improves accuracy. A possible reason is that the maximum-a-posteriori procedure might produce results not representative of the full posterior when too many spatial frequencies contain only noise. What might mitigate this is to replace the maximum-a-posteriori estimator by a maximization of the expected utility. The expected utility is a Bayes estimator convolved with a continuous utility function (MacKay, 2006). In this case we no longer maximize the probability of reaching zero aberrations exactly, but instead the probability of reducing aberrations to below a tolerable level, set, for example, by the pixel size.

Secondly, the current implementation of the algorithm is not parallelized. Since the main computational burden comes from numerically maximizing the profile posterior, a large speed boost could be expected from parallelizing calculations for different spatial frequencies, for example using multiple processor cores or a GPU. Thirdly, we modeled noise as additive Gaussian white noise; in particular at low numbers of electrons per pixel, a Poisson noise model would be more appropriate. Lastly, the effects of spherical aberration and other higher order aberrations on the *PSF* are currently not taken into account.

7 General Discussion

7.1 Correcting aberrations adds complexity

Correcting optical aberrations adds considerable complexity to an imaging system and makes it more error-prone. At the very least, an active element has to be integrated into the beam path, which often needs additional elements for calibration, and relay elements for optical conjugation. Depending on the correction algorithm used, wavefront measurement hardware can significantly increase the total size and cost of the microscope. Likewise, the aberration correction needs to be integrated on the software level, potentially hampering usability, increasing development time and the burden of maintenance. In particular, for long-term *in vivo* experiments, timing is often dictated by biology, so frequent maintenance problems can undermine the usability of an overly complex microscope.

On the other hand, a robust implementation of adaptive optics can help to compensate slight misalignments made elsewhere in the system, potentially simplifying the overall alignment. Compensation of uncontrollable aberrations, for example due to the atmosphere or sample, allows reaching a system performance which would be unthinkable even in a perfectly aligned system without active correction.

It is therefore important to balance the possible gain of adaptive optics against the added complexity of such a system. It seems only advisable for samples that otherwise could not be studied at all, or when an experimentally very simple and robust implementation can be found.

7.2 Defocus correction in high-NA OCM is worth it

In this work, we have shown that defocus correction is essential for deep imaging in high-NA OCM and we therefore integrated an automatic correction scheme into our deep-OCM microscope. Since the hardware for correction in this case was as simple as a single stepper motor (used to change the relative length of the interferometer arms), our correction scheme should be robust enough for everyday adoption in biological applications. In fact, this correction is now routinely used in commercial microscopes by LLTech (Paris, France).

7.3 Two-photon rat-brain imaging suffers from spherical aberration

Going beyond OCM, our refractive index measurement allowed us to theoretically evaluate the importance of spherical aberration for deep two-photon microscopy. We found that routinely achievable imaging depths of 200-400 μm are already starting to be limited by spherical aberrations. This is coherent with the recent experimental results from pupil segmentation (Ji, et al., 2012). However, since we only measured the average refractive index and not its spatial variations, we can make no precise statement about the magnitude of other aberration modes.

If those variations are small compared to the refractive index mismatch between immersion medium and sample, spherical aberration will dominate over those other aberrations. Good correction could then be achieved by simply using an objective with motorized correction collar, available from several manufacturers (for example motCORR objectives, Leica Microsystems, Wetzlar or FV10i-DOC, Olympus, Shinjuku, Tokyo).

If, on the other hand, spatial refractive index variations cause significant amounts of higher order aberrations, such an approach will not be very helpful. Instead, a full adaptive optics system would be needed, which brings us back to the central question: what is the best way to measure aberrations in microscopy?

7.4 The race is still on

A side-effect of our refractive index measurement using OCM was the insight that defocus aberration could be determined as deep as 900 μm in the juvenile rat brain by simple signal strength maximization. Due to the close similarities of OCM to coherence gated wavefront sensing (CGWS) this gives some hope that the latter technique can someday be used in similar samples. We are currently pursuing this path with a Linnik-based CGWS system, but it seem unlikely that comparable depths can be achieved if no way is found to combat multiple scattering (Wang, et al., 2012).

This leaves the different forms of image-based aberration measurement. As discussed in the introduction, we believe that phase diversity can lead to much more efficient estimators in microscopy, combining the virtues of pupil segmentation and modal wavefront sensing. Existing implementations in microscopy (Hanser, et al., 2003; Hanser, et al., 2004) take a heuristic approach to find the aberration parameters most consistent with the measured images.

For the simple case of two-dimensional samples, geometric optics and only three aberration modes, which is valid for scanning electron microscopy, we have shown that phase diversity in the form of MAPFoSt significantly outperforms other image-based algorithms in terms of achievable precision per dose and sample independence. It is an improvement over previous maximum likelihood implementations of phase diversity by allowing the incorporation of priors and by having linear scaling of runtime with input image size (instead of n log n) for finding the maximum of the posterior (albeit not for the initial Fourier transform of each image). This allows large low-dose images to be used for aberration correction, spreading the imaging-induced destruction of the sample to the largest area possible.

This technique has the potential to go beyond SBEM to other EM or light microscopes. Whenever there is a theoretical model for an imaging system, how it reacts to aberrations, and a model for the dominant noise sources, it should be possible to implement Phase Diversity using Bayesian inference, such as MAPFoSt.

Such an implementation can be expected to generally outperform metric-based and in particular model-agnostic algorithms in terms of aberration estimation precision at fixed total signal. Of course this comes at the expense of an increased mathematical and computational complexity, so a reasonable compromise has to be found.

In the long term, efforts should be undertaken to make Bayesian implementations of Phase Diversity, such as MAPFoSt, the standard in all image-based adaptive optics microscopes.

8 Acknowledgements

9 Appendices

9.1 Deep-OCM motor placement

Even though for simplicity and didactic purposes, chapter 4.2.1 talked about "reference arm length", the more general expression "relative arm length" would be more appropriate. Making the reference arm longer can equivalently be replaced by shortening the sample arm. For a setup with full flexibility, it is therefore enough to motorize two out of the three components sample (z), sample-arm objective (ℓ) and reference arm (d).
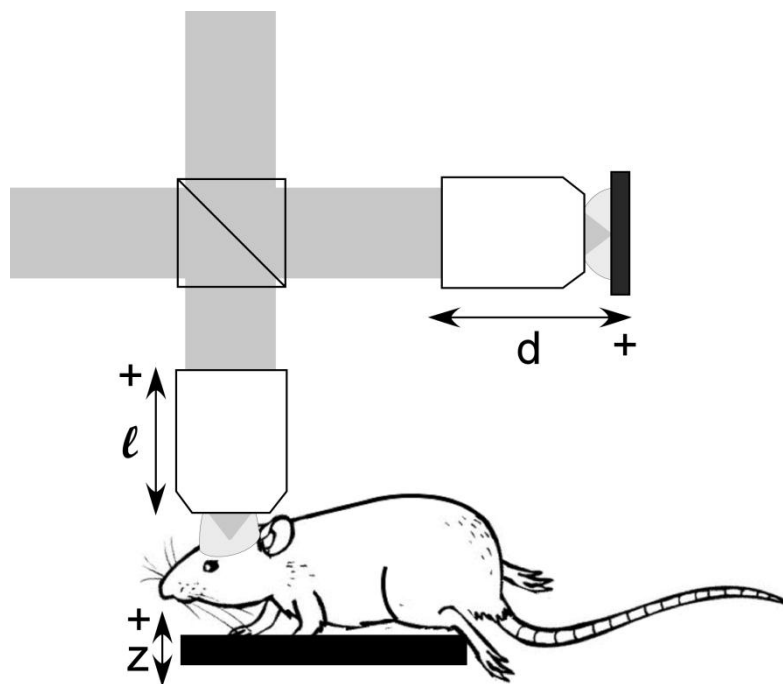
Figure 9-1. Possible motor placements in a full field OCM system: the sample (z), the sample arm objective (ℓ) and the reference arm (d). The direction of positive movement for each motor is marked by +.

To understand this subchapter it is important to keep the following (slightly unintuitive) facts in mind: the focus is defined by the distance between objective and sample, but it *does not determine which plane is being imaged* in OCM. The imaging plane is solely determined by the coherence volume, i.e. by the relative length of sample arm and reference arm.

Three fundamental operations need to be implemented with the two motors:

1) changing the imaging depth inside the sample by a nominal distance Δz, ignoring defocus

2) moving the focus inside the sample, keeping the imaging plane fixed

3) focus tracking, i.e. changing imaging and focusing depths by the same amount. The defocus slope $s = \dfrac{\delta}{z} = \dfrac{2d}{z}$ needs to be known for this.

The physical movements needed for these three operations are summarized in Table 9-1, separately for the three cases of motor placement.

Table 9-1

	Operation 1 changing depth, ignoring defocus	**Operation 2** focus scan at fixed imaging depth	**Operation 3** changing depth, with focus tracking
Sample and reference arm motorized	$z \to z + \Delta z$ $\ell \to \ell$ $d \to d$	$z \to z - \Delta\ell$ $\ell = const$ $d \to d + n_g \Delta\ell$	$z \to z + \Delta z$ $\ell = const$ $d \to d + \dfrac{s}{2}\Delta z$
Sample and objective motorized		$z \to z + (n_g - 1)\Delta\ell$ $\ell \to \ell + n_g \Delta\ell$ $d = const$	$z \to z + \left(\dfrac{s}{2} + 1\right)\Delta z$ $\ell \to \ell + \dfrac{s}{2}\Delta z$ $d = const$
Objective and reference arm motorized	$z = const$ $\ell \to \ell - \Delta z$ $d \to d + \Delta z$	$z = const$ $\ell \to \ell + \Delta\ell$ $d \to d + (n_g - 1)\Delta\ell$	$z = const$ $\ell \to \ell + \Delta z$ $d \to d + \left(\dfrac{s}{2} - 1\right)\Delta z$

9.2 Derivations for MAPFoSt

Derivations were done with Mathematica 6 and Mathematica 8 (Wolfram Research).

9.2.1 Calculating the MTF and its derivatives

■ **Definitions and MTF with astigmatism in cylindrical coordinates**

Approximating the ellipse lengths for focal length>>astigmatism; express pupil radius r / focal length f as tNA (tangens-based NA, i.e. $\tan \alpha$ instead of $\sin \alpha$):

```
ellipseaexact[Δz_, z_] = r (Δz - z) / (Δz + f);
ellipsebexact[Δz_, z_] = r (Δz + z) / (Δz - f);
ellipsea[Δz_, z_] = tNA Sqrt[( Δz - z)^2];
ellipseb[Δz_, z_] = tNA Sqrt[(- ( Δz + z))^2];
```

rotated coordinate system for k_x, k_y:

```
kxt[kx_, ky_, ϕ_] = kx * Cos[ϕ] + ky * Sin[ϕ];
kyt[kx_, ky_, ϕ_] = -kx * Sin[ϕ] + ky * Cos[ϕ];
```

The MTF (modulation transfer function) is the fourier transform of the PSF, which is an ellipse in our case, so we get a Bessel function: (starting 2010-02-09 (MTF for SPFSEM08*.nb) the MTF is normalized to MTF(0)=1 instead of π, and the parameter is kx, ky instead of fx, fy)

```
ρ[kx_, ky_, z_, Δz_, ϕ_] =
  Sqrt[kxt[kx, ky, ϕ]^2 * ellipsea[Δz, z]^2 + kyt[kx, ky, ϕ]^2 * ellipseb[Δz, z]^2]
```

$$\sqrt{\left(\text{tNA}^2\,(-z-\Delta z)^2\,(ky\,\text{Cos}[\phi]-kx\,\text{Sin}[\phi])^2+\text{tNA}^2\,(-z+\Delta z)^2\,(kx\,\text{Cos}[\phi]+ky\,\text{Sin}[\phi])^2\right)}$$

■ **Going to "cartesian" coordinates for the astigmatism (expressing ϕ and Δz through $a_{\text{ax(ial)}}$ and a_{diag})**

```
ρcart[kx_, ky_, z_, aax_, adiag_] =
  FullSimplify[ρ[kx, ky, z, Sqrt[aax^2 + adiag^2], ArcTan[aax, adiag] / 2],
    {aax ∈ Reals, adiag ∈ Reals}]
```

$$\sqrt{\left(\text{tNA}^2\,\left(-2\,\text{aax}\,kx^2\,z-4\,\text{adiag}\,kx\,ky\,z+2\,\text{aax}\,ky^2\,z+\left(kx^2+ky^2\right)\left(\text{aax}^2+\text{adiag}^2+z^2\right)\right)\right)}$$

```
MTFcart[kx_, ky_, z_, aax_, adiag_] = (*Exp[- ρcart[kx,ky,z,aax,adiag]^2/8]*)
  2 BesselJ[1, ρcart[kx, ky, z, aax, adiag]] / ρcart[kx, ky, z, aax, adiag]
```

$$\left(2\,\text{BesselJ}\left[1,\sqrt{\left(\text{tNA}^2\right.}\right.\right.$$
$$\left.\left(-2\,\text{aax}\,kx^2\,z-4\,\text{adiag}\,kx\,ky\,z+2\,\text{aax}\,ky^2\,z+\left(kx^2+ky^2\right)\left(\text{aax}^2+\text{adiag}^2+z^2\right)\right)\right)]\right)/$$
$$\left(\sqrt{\left(\text{tNA}^2\,\left(-2\,\text{aax}\,kx^2\,z-4\,\text{adiag}\,kx\,ky\,z+2\,\text{aax}\,ky^2\,z+\left(kx^2+ky^2\right)\left(\text{aax}^2+\text{adiag}^2+z^2\right)\right)\right)}\right)$$

■ **Show BesselMTF**

```
BesselMTF = 2 BesselJ[1, ρcart[kx, ky, z, aax, adiag]] / ρcart[kx, ky, z, aax, adiag]
```

$$\left(2\,\text{BesselJ}\left[1,\sqrt{\left(\text{tNA}^2\right.}\right.\right.$$
$$\left.\left(-2\,\text{aax}\,kx^2\,z-4\,\text{adiag}\,kx\,ky\,z+2\,\text{aax}\,ky^2\,z+\left(kx^2+ky^2\right)\left(\text{aax}^2+\text{adiag}^2+z^2\right)\right)\right)]\right)/$$
$$\left(\sqrt{\left(\text{tNA}^2\,\left(-2\,\text{aax}\,kx^2\,z-4\,\text{adiag}\,kx\,ky\,z+2\,\text{aax}\,ky^2\,z+\left(kx^2+ky^2\right)\left(\text{aax}^2+\text{adiag}^2+z^2\right)\right)\right)}\right)$$

```
Plot[ (2 BesselJ[1, x])/x , {x, 0, 40}, PlotRange → Full]
```
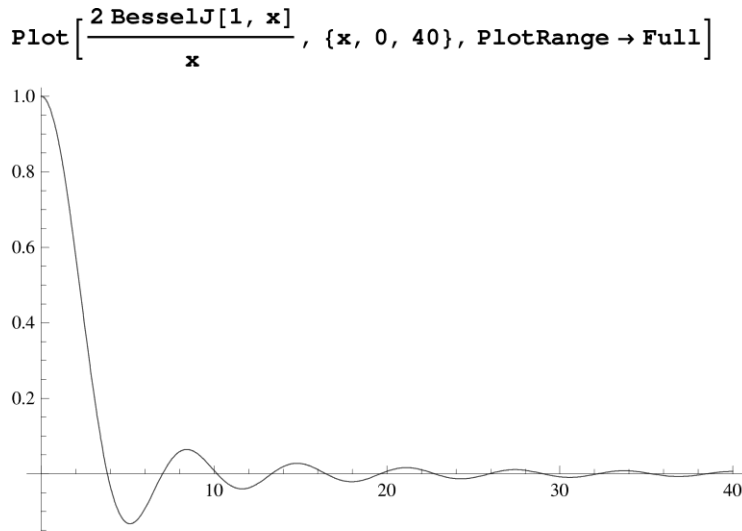

■ Calculate the second derivative of the MTF:

```
fsD = Simplify[D[MTFcart[kx, ky, z, aax, adiag], {{z, aax, adiag}, 2}]];
```

```
dummy = Table[dummya[i, j], {i, 1, Length[fsD]}, {j, 1, Length[fsD[[1]]]}];
denominator2 = FullSimplify[
    Denominator[Together[Flatten[dummy].Flatten[fsD /. ρab -> ρcart]]], tNA > 0]
```

$$2 \, tNA \left(-2 \, aax \, kx^2 \, z - 4 \, adiag \, kx \, ky \, z + 2 \, aax \, ky^2 \, z + \left(kx^2 + ky^2\right) \left(aax^2 + adiag^2 + z^2\right)\right)^{5/2}$$

This matches the argument of the Bessel function (ρ)! So I can calculate the special cases (where fsD is not well defined) from the quadratic Taylor term of MTFcartρab at $\rho=0$:

```
speciald2MTF =
 Simplify[D[Normal[Series[MTFcartρab[kx, ky, z, aax, adiag], {ρab[kx, ky, z, aax,
         adiag], 0, 2}]] /. ρab → ρcart, {{z, aax, adiag}, 2}]] // TableForm
```

$$-\frac{1}{4} \left(kx^2 + ky^2\right) tNA^2 \qquad \frac{1}{4} \left(kx^2 - ky^2\right) tNA^2 \qquad \frac{1}{2} kx \, ky \, tNA^2$$

$$\frac{1}{4} \left(kx^2 - ky^2\right) tNA^2 \qquad -\frac{1}{4} \left(kx^2 + ky^2\right) tNA^2 \qquad 0$$

$$\frac{1}{2} kx \, ky \, tNA^2 \qquad 0 \qquad -\frac{1}{4} \left(kx^2 + ky^2\right) tNA^2$$

■ Calculate the first derivative of MTF :

```
d1MTFsym = D[MTFcart[kx, ky, z, aax, adiag], {{z, aax, adiag, tNA}, 1}];
```

```
denominator1 = FullSimplify[Denominator[
    Together[a1 d1MTFsym[[1]] + a2 d1MTFsym[[2]] + a3 d1MTFsym[[3]]]], tNA > 0]
```

$$tNA \left(-2 \, aax \, kx^2 \, z - 4 \, adiag \, kx \, ky \, z + 2 \, aax \, ky^2 \, z + \left(kx^2 + ky^2\right) \left(aax^2 + adiag^2 + z^2\right)\right)^{3/2}$$

-> Special cases again are all $\rho=0$, where d1MTF=0.

118

9.2.2 Calculating the MAPFoSt posterior and profile posterior

Three cases how to deal with the object O in the expression p (I1, I2 | A, O) = p (O) * p (I1 | A, O) p (I2 | A, O)
- plug in maximum likelihood O
- integrate it out, flat prior on the object
- integrate it out, gaussian prior.

```
p0delta = PDF[NormalDistribution[Object * MTF1, sigmaN], I1]
    PDF[NormalDistribution[Object * MTF2, sigmaN], I2];
p0ML = Simplify[p0delta /. Solve[D[p0delta, Object] == 0, Object][[1]]];
p0flat = Integrate[PDF[NormalDistribution[Object * MTF1, sigmaN], I1]
    PDF[NormalDistribution[Object * MTF2, sigmaN], I2],
    {Object, -∞, ∞}, Assumptions → {sigmaN ∈ Reals, sigmaN > 0,
      sigmaO ∈ Reals, sigmaO > 0, MTF1² + MTF2² > 0}];
p0gauss = Integrate[PDF[NormalDistribution[0, sigmaO], Object]
    PDF[NormalDistribution[Object * MTF1, sigmaN], I1]
    PDF[NormalDistribution[Object * MTF2, sigmaN], I2],
    {Object, -∞, ∞}, Assumptions → {sigmaN ∈ Reals, sigmaN > 0,
```
$$\text{sigmaO} \in \text{Reals, sigmaO} > 0, \ \frac{\text{MTF1}^2}{\text{sigmaN}^2} + \frac{\text{MTF2}^2}{\text{sigmaN}^2} + \frac{1}{\text{sigmaO}^2} > 0\}];$$
```
p1delta = p0delta /. {MTF1 → MTF[A + t1], MTF2 → MTF[A + t2]}
p1flat = p0flat /. {MTF1 → MTF[A + t1], MTF2 → MTF[A + t2]}
p1gauss = p0gauss /. {MTF1 → MTF[A + t1], MTF2 → MTF[A + t2]}
p1ML = p0ML /. {MTF1 → MTF[A + t1], MTF2 → MTF[A + t2]}
```

results in

$$\text{p1flat} = \frac{e^{-\frac{(I2\,MTF[A+t1]-I1\,MTF[A+t2])^2}{2\,sigmaN^2\,(MTF[A+t1]^2+MTF[A+t2]^2)}}}{\sqrt{2\pi}\ sigmaN\ \sqrt{MTF[A+t1]^2+MTF[A+t2]^2}};$$

$$\text{p1gauss} = \frac{e^{-\frac{(I1^2+I2^2)\,sigmaN^2+sigmaO^2\,(I2\,MTF[A+t1]-I1\,MTF[A+t2])^2}{2\,sigmaN^2\,(sigmaN^2+sigmaO^2\,(MTF[A+t1]^2+MTF[A+t2]^2))}}}{2\pi\ sigmaN\ \sqrt{sigmaN^2+sigmaO^2\,(MTF[A+t1]^2+MTF[A+t2]^2)}};$$

$$\text{p1ML} = \frac{e^{-\frac{(I2\,MTF[A+t1]-I1\,MTF[A+t2])^2}{2\,sigmaN^2\,(MTF[A+t1]^2+MTF[A+t2]^2)}}}{2\pi\ sigmaN^2};$$

■ **Simplify[Log[p]] doesn' t work, so we take the Log by hand :**

$$\text{lnpFlatPrior} = -\frac{(I2\,MTF[A+t1]-I1\,MTF[A+t2])^2}{2\,sigmaN^2\,(MTF[A+t1]^2+MTF[A+t2]^2)} -$$
$$\text{Log}\left[\sqrt{2\pi}\ sigmaN\ \sqrt{MTF[A+t1]^2+MTF[A+t2]^2}\right];$$
$$\text{lnpGaussPrior} = -\left((I1^2+I2^2)\,sigmaN^2+sigmaO^2\,(I2\,MTF[A+t1]-I1\,MTF[A+t2])^2\right) \Big/$$
$$\left(2\,sigmaN^2\,(sigmaN^2+sigmaO^2\,(MTF[A+t1]^2+MTF[A+t2]^2))\right) -$$
$$\text{Log}\left[2\pi\ sigmaN\ \sqrt{(sigmaN^2+sigmaO^2\,(MTF[A+t1]^2+MTF[A+t2]^2))}\right];$$
$$\text{lnpML} = -\frac{(I2\,MTF[A+t1]-I1\,MTF[A+t2])^2}{2\,sigmaN^2\,(MTF[A+t1]^2+MTF[A+t2]^2)} - \text{Log}\left[2\pi\ sigmaN^2\right];$$

■ **Taking derivative of log p (I1,I2|A,O) with respect to the object O**

```
p1delta = p0delta /. {MTF1 → MTF[A + t1], MTF2 → MTF[A + t2]}
```

$$\frac{e^{-\frac{(I1-Object\ MTF[A+t1])^2}{2\ sigmaN^2} - \frac{(I2-Object\ MTF[A+t2])^2}{2\ sigmaN^2}}}{2\ \pi\ sigmaN^2}$$

```
dOlnp = Simplify[D[Log[p1delta], Object]]
```

$$\frac{1}{sigmaN^2}\left(I1\ MTF[A + t1] - Object\ MTF[A + t1]^2 + MTF[A + t2]\ (I2 - Object\ MTF[A + t2])\right)$$

```
dAlnp = Simplify[D[Log[p1delta], A]]
```

$$\frac{1}{sigmaN^2}$$

Object ((I1 – Object MTF[A + t1]) MTF′[A + t1] + (I2 – Object MTF[A + t2]) MTF′[A + t2])

■ **Taking first derivative of log p (I2 | A, I1) with respect to A**

```
lnpFlatPriorprime = Simplify[D[Log[p1flat], A]];
lnpGaussPriorprime = Simplify[D[Log[p1gauss], A]];
lnpMLprime = Simplify[D[Log[p1ML], A]]
```

= (I2 MTF[A + t1] – I1 MTF[A + t2]) (I1 MTF[A + t1] + I2 MTF[A + t2])

(–MTF[A + t2] MTF′[A + t1] + MTF[A + t1] MTF′[A + t2])) $\Big/$

$\left(sigmaN^2\ \left(MTF[A + t1]^2 + MTF[A + t2]^2\right)^2\right)$

■ Second derivative:

Protect existing derivatives to correctly transform it into MATLAB code later :

```
lnpMLprimeprot = lnpMLprime /. Derivative[1][MTF] → MTFdi
```

((I2 MTF[A + t1] – I1 MTF[A + t2]) (I1 MTF[A + t1] + I2 MTF[A + t2])

(–MTF[A + t2] MTFdi[A + t1] + MTF[A + t1] MTFdi[A + t2])) $\Big/$

$\left(sigmaN^2\ \left(MTF[A + t1]^2 + MTF[A + t2]^2\right)^2\right)$

```
d2lnpML = Simplify[D[lnpMLprimeprot, A]] /.
   {Derivative[1][MTF] → MTFdj, Derivative[1][MTFdi] → d2MTFij}
```

$\Big($(I1 MTF[A + t1] + I2 MTF[A + t2]) $\left(MTF[A + t1]^2 + MTF[A + t2]^2\right)$

(–MTF[A + t2] MTFdi[A + t1] + MTF[A + t1] MTFdi[A + t2])

(I2 MTFdj[A + t1] – I1 MTFdj[A + t2]) + (I2 MTF[A + t1] – I1 MTF[A + t2])

$\left(MTF[A + t1]^2 + MTF[A + t2]^2\right)$ (–MTF[A + t2] MTFdi[A + t1] + MTF[A + t1] MTFdi[A + t2])

(I1 MTFdj[A + t1] + I2 MTFdj[A + t2]) –

4 (I2 MTF[A + t1] – I1 MTF[A + t2]) (I1 MTF[A + t1] + I2 MTF[A + t2])

(–MTF[A + t2] MTFdi[A + t1] + MTF[A + t1] MTFdi[A + t2])

(MTF[A + t1] MTFdj[A + t1] + MTF[A + t2] MTFdj[A + t2]) +

(I2 MTF[A + t1] – I1 MTF[A + t2]) (I1 MTF[A + t1] + I2 MTF[A + t2])

$\left(MTF[A + t1]^2 + MTF[A + t2]^2\right)$ (d2MTFij[A + t2] MTF[A + t1] – d2MTFij[A + t1]

MTF[A + t2] + MTFdi[A + t2] MTFdj[A + t1] – MTFdi[A + t1] MTFdj[A + t2])) $\Big/$

$\left(sigmaN^2\ \left(MTF[A + t1]^2 + MTF[A + t2]^2\right)^3\right)$

9.3 The heuristic SEM autofocus and auto-stigmation algorithm

The heuristic algorithm previously used (Briggman, et al., 2011) also makes use of the fact that aberrations change the *MTF* and thereby the Fourier spectrum of images; however it first calculates coefficients for each image, and then combines the coefficients from two test images $\mathbf{I_1}$, $\mathbf{I_2}$ (acquired with test aberrations +$\mathbf{T}$ and −$\mathbf{T}$ respectively) to estimate the actual aberrations.

In its current implementation, each image is cropped to 512x512 pixels, the mean value is subtracted, the autocorrelation calculated and cropped to the center 64x64 pixel region $A(x,y)$. Then the dot-product with a number of different weight functions is calculated to obtain coefficients *apx, amx, apy, amy, fi, and fo;*

$$apx = \frac{\iint A(x,y) \times \left[\sin^2(\varphi)\right] \times \left[\exp\left(-\frac{r^2}{\alpha}\right) - \exp\left(-\frac{r^2}{\beta}\right)\right]}{\iint \left[\sin^2(\varphi)\right] \times \left[\exp\left(-\frac{r^2}{\alpha}\right) - \exp\left(-\frac{r^2}{\beta}\right)\right]}$$

$$amx = \frac{\iint A(x,y) \times \left[\cos^2(\varphi)\right] \times \left[\exp\left(-\frac{r^2}{\alpha}\right) - \exp\left(-\frac{r^2}{\beta}\right)\right]}{\iint \left[\cos^2(\varphi)\right] \times \left[\exp\left(-\frac{r^2}{\alpha}\right) - \exp\left(-\frac{r^2}{\beta}\right)\right]}$$

$$apy = \frac{\iint A(x,y) \times \left[\sin^2\left(\varphi + \frac{\pi}{4}\right)\right] \times \left[\exp\left(-\frac{r^2}{\alpha}\right) - \exp\left(-\frac{r^2}{\beta}\right)\right]}{\iint \left[\sin^2\left(\varphi + \frac{\pi}{4}\right)\right] \times \left[\exp\left(-\frac{r^2}{\alpha}\right) - \exp\left(-\frac{r^2}{\beta}\right)\right]}$$

$$amy = \frac{\iint A(x,y) \times \left[\sin^2\left(\varphi - \frac{\pi}{4}\right)\right] \times \left[\exp\left(-\frac{r^2}{\alpha}\right) - \exp\left(-\frac{r^2}{\beta}\right)\right]}{\iint \left[\sin^2\left(\varphi - \frac{\pi}{4}\right)\right] \times \left[\exp\left(-\frac{r^2}{\alpha}\right) - \exp\left(-\frac{r^2}{\beta}\right)\right]}$$

$$fi = \frac{\iint A(x,y) \times \left[\exp\left(-\frac{r^2}{\gamma}\right) - \exp\left(-\frac{r^2}{\delta}\right)\right]}{\iint \left[\exp\left(-\frac{r^2}{\gamma}\right) - \exp\left(-\frac{r^2}{\delta}\right)\right]}$$

$$fo = \frac{\iint A(x,y) \times \left[\exp\left(-\frac{r^2}{\varepsilon}\right) - \exp\left(-\frac{r^2}{\gamma}\right)\right]}{\iint \left[\exp\left(-\frac{r^2}{\varepsilon}\right) - \exp\left(-\frac{r^2}{\gamma}\right)\right]}$$

with $\alpha = 6$, $\beta = 0.5$, $\gamma = 3$, $\delta = 0.5$ and $\varepsilon = 9$ (all in pixels²).

Now the coefficients are used to calculate single-image estimators for astigmatism and focus that are normalized for image contrast and signal strength but still depend on the spatial-frequency spectrum of the object.

$$astgx = \frac{apx - amx}{apx + amx}$$

$$astgy = \frac{apy - amy}{apy + amy}$$

$$foc = \frac{fi - fo}{fi + fo}$$

The differences between the corresponding coefficients for the two images are uncalibrated estimators for the actual aberrations. To obtain calibrated estimates, the coefficients c_1, c_2, and c_3 need to be determined for each sample

$$z = c_1(foc_1 - foc_2)$$

$$a_{on-axis} = c_2(astgx_1 - astgx_2)$$

$$a_{diagonal} = c_3(astgy_1 - astgy_2)$$

Note, that the heuristic algorithm also requires its astigmatism estimates to be rotated to match the electron microscope's coordinate system,

$$\begin{pmatrix} a_x \\ a_y \end{pmatrix} = \mathbf{R} \begin{pmatrix} a_{on-axis} \\ a_{diagonal} \end{pmatrix}$$

where $\mathbf{R}$ is the appropriate 2D rotation matrix.

9.4 Modal wavefront sensing for SEM

Modal wavefront sensing (Neil, et al., 2000; Débarre, et al., 2008; Débarre, et al., 2009) was used in chapter 1 as a reference to provide a reliable, independent determination of the best astigmatism and focus settings. It mimics and formalizes the aberration optimization procedure a human operator would typically follow. Images are taken with several (in our

case seven) different values for one of the aberration parameters (defocus or astigmatism) and for each image, a metric judging image quality is calculated. The dependence of the metric on the aberration parameter is fitted with a Gaussian-function-with-offset in order to determine the optimal parameter value.

The metric is constructed by integrating the image power in an annulus of spatial frequencies, since low spatial frequencies in the images are mostly unchanged by aberrations and high spatial frequencies are often dominated by noise. We used the range from 0.035 to 0.212 times the one-dimensional Nyquist frequency for our metric.

For small initial aberrations, defocus and both astigmatism modes are orthogonal with respect to this metric, meaning that the global optimum can be found simply by doing a one-dimensional optimization of one parameter after the other. However, when initial aberrations are too large, two problems can appear. Firstly, the metric values will get very noisy. Secondly, if initial aberrations happen to correspond to settings close to a line focus, which suppresses signal except in one preferred direction within the frequency range used by the metric, the algorithm will get stuck in the local maximum corresponding to the line focus, i.e. with identical amounts of defocus and astigmatism. To mitigate the second problem, we always performed modal wavefront sensing using the result of MAPFoSt as a starting point, so that initial aberrations generally were very small. To make sure noise was not the dominant problem, and to exclude temporal drifts and effects of sample destruction due to overexposure, a forward-backward scan of aberration parameters was performed. For the biological sample, two subsequent iterations of modal sensing led to clear peaks in the metric for all three modes (Figure 9-2).
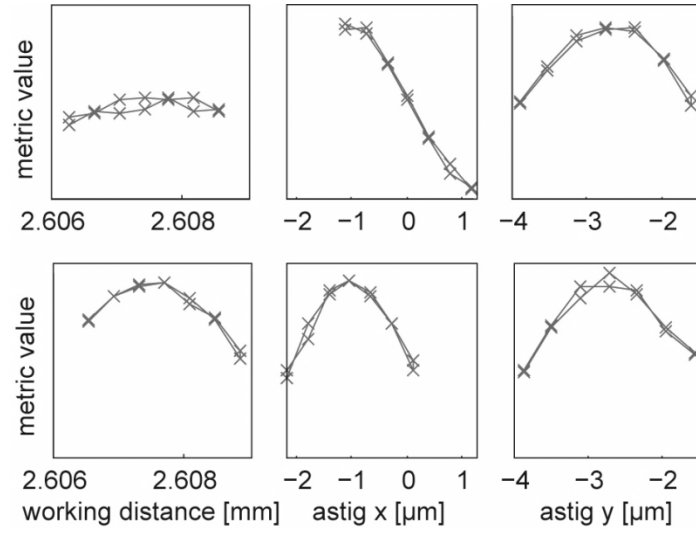
Figure 9-2. Modal wavefront sensing provides a reference for microscope parameters corresponding to zero aberrations. Consecutive modal scans of a) working distance, b) astigmatism x and c) astigmatism y allow removal of the residual astigmatism x present after the first iteration of 20 nm MAPFoSt in Figure 7b, as evidenced by a second iteration of modal scans d) working distance, e) astigmatism x and f) astigmatism y. All 6 subfigures use the same y scaling for the metric.

Note that in principle, modal sensing can work with as little as three images per aberration mode. Since we wanted to use it as a ground-truth reference, we used as many as 14 images per mode.

10 Literature

ALEXANDROV, S.A., ZVYAGIN, A.V., DILUSHA SILVA, K.K.M.B. & SAMPSON, D.D. (2003). Bifocal optical coherenc refractometry of turbid media. Opt. Lett. **28**(2), 117-119.

ANDEGEKO, Y., PESTOV, D., LOZOVOY, V.V. & DANTUS, M. Ultrafast multiphoton microscopy with high-order spectral phase distortion compensation. In *Multiphoton Microscopy in the Biomedical Sciences IX*, pp. 71830W-71836. SPIE.

AZUCENA, O., CREST, J., KOTADIA, S., SULLIVAN, W., TAO, X., REINIG, M., GAVEL, D., OLIVIER, S. & KUBBY, J. (2011). Adaptive optics wide-field microscopy using direct wavefront sensing. Opt. Lett. **36**(6), 825-827.

BABA, N., TERAYAMA, K., YOSHIMIZU, T., ICHISE, N. & TANAKA, N. (2001). An auto-tuning method for focusing and astigmatism correction in HAADF-STEM, based on the image contrast transfer function. J Electron Microsc (Tokyo) **50**(3), 163-176.

BATES, W.J. (1947). A wavefront shearing interferometer. Proceedings of the Physical Society **59**(6), 940.

BAUMANN, N. & PHAM-DINH, D. (2001). Biology of oligodendrocyte and myelin in the mammalian central nervous system. Physiol Rev **81**(2), 871-927.

BEAUREPAIRE, E., BOCCARA, A.C., LEBEC, M., BLANCHOT, L. & SAINT-JALMES, H. (1998). Full-field optical coherence microscopy. Opt Lett **23**(4), 244-246.

BEN AROUS, J., BINDING, J., LÉGER, J., CASADO, M., TOPILKO, P., GIGAN, S., CLAUDE BOCCARA, A. & BOURDIEU, L. (2011). Single myelin fiber imaging in living rodents without labeling by deep optical coherence microscopy. J. Biomed. Opt. **16**(11), 116012.

BETZIG, E., PATTERSON, G.H., SOUGRAT, R., LINDWASSER, O.W., OLENYCH, S., BONIFACINO, J.S., DAVIDSON, M.W., LIPPINCOTT-SCHWARTZ, J. & HESS, H.F. (2006). Imaging intracellular fluorescent proteins at nanometer resolution. Science **313**(5793), 1642-1645.

BINDING, J. (2008). Adaptive Optics in Two-Photon-Microscopy. In *Fakultät für Physik und Astronomie*, pp. 99. Heidelberg: Ruprecht-Karls-Universität Heidelberg.

BINDING, J., BEN AROUS, J., LÉGER, J.-F., GIGAN, S., BOCCARA, C. & BOURDIEU, L. (2011). Brain refractive index measured in vivo with high-NA defocus-corrected full-field OCT and consequences for two-photon microscopy. Opt. Express **19**(6), 4833-4847.

BINDING, J. & RÜCKEL, M. (in preparation). Coherence-Gated Wavefront Sensing. In *Adaptive Optics for Biological Imaging*, Kubby, J. (Ed.): Taylor & Francis.

BINNIG, G., ROHRER, H., GERBER, C. & WEIBEL, E. (1982a). Surface Studies by Scanning Tunneling Microscopy. Phys Rev Lett **49**(1), 57-61.

BINNIG, G., ROHRER, H., GERBER, C. & WEIBEL, E. (1982b). Tunneling through a controllable vacuum gap. Appl Phys Lett **40**(2), 178-180.

BLACKMAN, R.B. & TUKEY, J.W. (1959). *The measurement of power spectra: from the point of view of communications engineering*. Dover Publications.

BLANC, A., FUSCO, T., HARTUNG, M., MUGNIER, L. & ROUSSET, G. (2003). Calibration of NAOS and CONICA static aberrations. Astronomy and Astrophysics **399**(1), 373-383.

BOOTH, M.J., DEBARRE, D. & WILSON, T. Image-based wavefront sensorless adaptive optics. In Carreras, R. A., Gonglewski, J. D. and Rhoadarmer, T. A. (Eds.), pp. 671102-671107. SPIE.

BORN, M. & WOLF, E. (1999). *Principles of Optics*. Cambridge, U.K.: Cambridge University Press.

BOTCHERBY, E.J., JUSKAITIS, R., BOOTH, M.J. & WILSON, T. (2007). Aberration-free optical refocusing in high numerical aperture microscopy. Opt. Lett. **32**(14), 2007-2009.

BRIGGMAN, K.L., HELMSTAEDTER, M. & DENK, W. (2011). Wiring specificity in the direction-selectivity circuit of the retina. Nature **471**(7337), 183-U167.

CHAIGNEAU, E., WRIGHT, A.J., POLAND, S.P., GIRKIN, J.M. & SILVER, R.A. (2011). Impact of wavefront distortion and scattering on 2-photon microscopy in mammalian brain tissue. Opt. Express **19**(23), 22755-22774.

CHENG, J.X., VOLKMER, A. & XIE, X.S. (2002). Theoretical and experimental characterization of coherent anti-Stokes Raman scattering microscopy. J Opt Soc Am B **19**(6), 1363-1375.

COULPIER, F., DECKER, L., FUNALOT, B., VALLAT, J.-M., GARCIA-BRAGADO, F., CHARNAY, P. & TOPILKO, P. (2010). CNS/PNS boundary transgression by central glia in the absence of Schwann cells or Krox20/Egr2 function. The Journal of neuroscience : the official journal of the Society for Neuroscience **30**(17), 5958-5967.

DAIMON, M. & MASUMURA, A. (2007). Measurement of the refractive index of distilled water from the near-infrared region to the ultraviolet region. Appl. Opt. **46**(18), 3811-3820.

DEAN, B.H. & BOWERS, C.W. (2003). Diversity selection for phase-diverse phase retrieval. J. Opt. Soc. Am. A **20**(8), 1490-1504.

DEBARRE, D., BOOTH, M.J. & WILSON, T. (2007). Image based adaptive optics through optimisation of low spatial frequencies. Opt. Express **15**(13), 8176-8190.

DÉBARRE, D., BOTCHERBY, E.J., BOOTH, M.J. & WILSON, T. (2008). Adaptive optics for structured illumination microscopy. Opt. Express **16**(13), 9290-9305.

DÉBARRE, D., BOTCHERBY, E.J., WATANABE, T., SRINIVAS, S., BOOTH, M.J. & WILSON, T. (2009). Image-based adaptive optics for two-photon microscopy. Opt. Lett. **34**(16), 2495-2497.

DENG, S., LIU, L., CHENG, Y., LI, R. & XU, Z. (2010). Effects of primary aberrations on the fluorescence depletion patterns of STED microscopy. Opt. Express **18**(2), 1657-1666.

DENK, W. & HORSTMANN, H. (2004). Serial block-face scanning electron microscopy to reconstruct three-dimensional tissue nanostructure. Plos Biol **2**(11), 1900-1909.

DENK, W., STRICKLER, J.H. & WEBB, W.W. (1990). Two-Photon Laser Scanning Fluorescence Microscopy. Science **248**(4951), 73-76.

DING, H. & ET AL. (2006). Refractive indices of human skin tissues at eight wavelengths and estimated dispersion relations between 300 and 1600 nm. Phys Med Biol **51**(6), 1479.

DOLNE, J. Cramer-Rao Lower Bound for Passive and Active Imaging Systems. In pp. IWB4. Optical Society of America.

DOLNE, J.J., TANSEY, R.J., BLACK, K.A., DEVILLE, J.H., CUNNINGHAM, P.R., WIDEN, K.C. & IDELL, P.S. (2003). Practical Issues in Wave-Front Sensing by Use of Phase Diversity. Appl. Opt. **42**(26), 5284-5289.

DREHER, A.W., BILLE, J.F. & WEINREB, R.N. (1989). Active Optical Depth Resolution Improvement of the Laser Tomographic Scanner. Appl Optics **28**(4), 804-808.

DUBOIS, A., VABRE, L., BOCCARA, A.C. & BEAUREPAIRE, E. (2002). High-resolution full-field optical coherence tomography with a Linnik microscope. Appl Optics **41**(4), 805-812.

EGNER, A. & HELL, S.W. (1999). Equivalence of the Huygens-Fresnel and Debye approach for the calculation of high aperture point-spread functions in the presence of refractive index mismatch. Journal of Microscopy **193**(3), 244-249.

FARRAR, M.J., RENNINGER, W., FETCHO, J.R., WISE, F.W. & SCHAFFER, C.B. Third Harmonic Generation as a Novel Technique for Imaging Myelin in the Central Nervous System. In *Biomedical Optics*, pp. BMC2. Optical Society of America.

FARRAR, MATTHEW J., WISE, FRANK W., FETCHO, JOSEPH R. & SCHAFFER, CHRIS B. (2011). In Vivo Imaging of Myelin in the Vertebrate Central Nervous System Using Third Harmonic Generation Microscopy. Biophys J **100**(5), 1362-1371.

FEIERABEND, M., RÜCKEL, M. & DENK, W. (2004). Coherence-gated wave-front sensing in strongly scattering samples. Opt Lett **29**(19), 2255-2257.

FERCHER, A.F. (1996). Optical Coherence Tomography (Review Paper). J Biomed Opt **1**(2), 157-173.

FU, Y., HUFF, T.B., WANG, H.-W., CHENG, J.-X. & WANG, H. (2008). Ex vivo and in vivo imaging of myelin fibers in mouse brain by coherent anti-Stokes Raman scattering microscopy. Opt. Express **16**(24), 19396-19409.

FUJIMOTO, J., BREZINSKI, M., TEARNEY, G., BOPPART, S., BOUMA, B., HEE, M., SOUTHERN, J. & SWANSON, E. (1995). Optical biopsy and imaging using optical coherence tomography. Nat Med **1**(9), 970-972.

GEORGE, M.R., FABIAN, A.C., SANDERS, J.S., YOUNG, A.J. & RUSSELL, H.R. (2009). X-ray observations of the galaxy cluster PKS 0745−191: to the virial radius, and beyond. Mon Not R Astron Soc **395**(2), 657-666.

GONSALVES, R.A. (1982). Phase retrieval and diversity in adaptive optics. Opt Eng **21**, 829-832.

GOTTSCHALK, W. (1993). Ein Messverfahren zur Bestimmung der optischen Parameter biologischer Gewebe in vitro. pp. 172. Karlsruhe: Universität Karlsruhe.

GUIZAR-SICAIROS, M., THURMAN, S.T. & FIENUP, J.R. (2008). Efficient subpixel image registration algorithms. Opt. Lett. **33**(2), 156-158.

GUIZAR, M. (2008). dftregistration.m - Efficient subpixel image registration by cross-correlation. In *Matlab Central - File Exchange on mathworks.com*.

HAISS, F., JOLIVET, R., WYSS, M.T., REICHOLD, J., BRAHAM, N.B., SCHEFFOLD, F., KRAFFT, M.P. & WEBER, B. (2009). Improved in vivo two-photon imaging after blood replacement by perfluorocarbon. The Journal of Physiology **587**(13), 3153-3158.

HANSER, B.M., GUSTAFSSON, M.G.L., AGARD, D.A. & SEDAT, J.W. (2001). Phase retrieval of widefield microscopy point spread functions. Three-Dimensional and Multidimensional Microscopy: Image Acquisition and Processing Viii **2**(18), 60-68.

HANSER, B.M., GUSTAFSSON, M.G.L., AGARD, D.A. & SEDAT, J.W. (2003). Phase retrieval for high-numerical-aperture optical systems. Opt Lett **28**(10), 801-803.

HANSER, B.M., GUSTAFSSON, M.G.L., AGARD, D.A. & SEDAT, J.W. (2004). Phase-retrieved pupil functions in wide-field fluorescence microscopy. J Microsc-Oxford **216**, 32-48.

HARDY, J.W. (1998). *Adaptive Optics For Astronomical Telescopes*. Oxford: Oxford University Press.

HARRIS, K.M. & KATER, S.B. (1994). DENDRITIC SPINES - CELLULAR SPECIALIZATIONS IMPARTING BOTH STABILITY AND FLEXIBILITY TO SYNAPTIC FUNCTION. Annual Review of Neuroscience **17**, 341-371.

HARTMANN, J. (1900). Bemerkungen über den Bau und die Justirung von Spektrographen. Zeit. f. Instrumentkd. **20**, 17.

HEINTZMANN, R. (2010). Correcting distorted optics: back to the basics. Nat Meth **7**(2), 108-110.

HELL, S.W., REINER, G., CREMER, C. & STELZER, E.H.K. (1993). Aberrations in confocal fluorescence microscopy induced by mismatches in refractive index. Journal of Microscopy **169**, 391-405.

HELL, S.W. & WICHMANN, J. (1994). Breaking the diffraction resolution limit by stimulated emission: stimulated-emission-depletion fluorescence microscopy. Opt. Lett. **19**(11), 780-782.

HESS, S.T., GIRIRAJAN, T.P.K. & MASON, M.D. (2006). Ultra-high resolution imaging by fluorescence photoactivation localization microscopy. Biophys J **91**(11), 4258-4272.

HUFF, T. & CHENG, J.X. (2007). In vivo coherent anti-Stokes Raman scattering imaging of sciatic nerve tissue. Journal of Microscopy **225**(2), 175-182.

IZATT, J.A., HEE, M.R., OWEN, G.M., SWANSON, E.A. & FUJIMOTO, J.G. (1994). Optical Coherence Microscopy in Scattering Media. Opt Lett **19**(8), 590-592.

JACOBSEN, H., HÄNNINEN, P., SOINI, E. & HELL, S. (1994). Refractive-index-induced aberrations in two-photon confocal fluorescence microscopy. Journal of Microscopy **176**(3), 226-230.

JI, N., MILKIE, D.E. & BETZIG, E. (2009). Adaptive optics via pupil segmentation for high-resolution imaging in biological tissues. Nat Meth **7**(2), 141-147.

JI, N., SATO, T.R. & BETZIG, E. (2012). Characterization and adaptive optical correction of aberrations during in vivo imaging in the mouse cortex. Proceedings of the National Academy of Sciences **109**(1), 22-27.

JUETTE, M.F., GOULD, T.J., LESSARD, M.D., MLODZIANOSKI, M.J., NAGPURE, B.S., BENNETT, B.T., HESS, S.T. & BEWERSDORF, J. (2008). Three-dimensional sub-100 nm resolution fluorescence microscopy of thick samples. Nat Meth **5**(6), 527-529.

KLAR, T.A., JAKOBS, S., DYBA, M., EGNER, A. & HELL, S.W. (2000). Fluorescence microscopy with diffraction resolution barrier broken by stimulated emission. P Natl Acad Sci USA **97**(15), 8206-8210.

KNUETTEL, A. & BOEHLAU-GODAU, M. (2000). Spatially confined and temporally resolved refractive index and scattering evaluation in human skin performed with optical coherence tomography. J Biomed Opt **5**(1), 83-92.

KOBAT, D., DURST, M., NISHIMURA, N., WONG, A., SCHAFFER, C. & XU, C. (2009). Deep tissue multiphoton microscopy using longer wavelength excitation. Opt. Express **17**, 13354-13364.

LABIAU, S., DAVID, G., GIGAN, S. & BOCCARA, A.C. (2009). Defocus test and defocus correction in full-field optical coherence tomography. Opt. Lett. **34**(10), 1576-1578.

LEE, D.J., ROGGEMANN, M.C. & WELSH, B.M. (1999). Cramér-Rao analysis of phase-diverse wave-front sensing. J. Opt. Soc. Am. A **16**(5), 1005-1015.

LEVINE, B.M., MARTINSEN, E.A., WIRTH, A., JANKEVICS, A., TOLEDO-QUINONES, M., LANDERS, F. & BRUNO, T.L. (1998). Horizontal line-of-sight turbulence over near-ground paths and implications for adaptive optics corrections in laser communications. Appl Optics **37**(21), 4553-4560.

LIANG, J.Z., GRIMM, B., GOELZ, S. & BILLE, J.F. (1994). Objective Measurement of Wave Aberrations of the Human Eye with the Use of a Hartmann-Shack Wave-Front Sensor. J Opt Soc Am A **11**(7), 1949-1957.

LÖFDAHL, M.G. & SCHARMER, G. (1994). Wavefront sensing and image restoration from focused and defocused solar images. Astron. Astrophys. Suppl. **107**, 243-264.

LUE, N., BEWERSDORF, J., LESSARD, M.D., BADIZADEGAN, K., DASARI, R.R., FELD, M.S. & POPESCU, G. (2007). Tissue refractometry using Hilbert phase microscopy. Opt Lett **32**(24), 3522-3524.

MACKAY, D.J.C. (2006). Decision Theory. In *Information theory, inference, and learning algorithms*, pp. 451-453. Cambridge [u.a.]: Cambridge Univ. Press.

MALACARA, D. (1992). *Optical Shop testing*. New York: John Wiley \& Sons, Inc.

MARSH, P.N., BURNS, D. & GIRKIN, J.M. (2003). Practical implementation of adaptive optics in multiphoton microscopy. Opt Express **11**(10), 1123-1130.

MEYNADIER, L., MICHAU, V., VELLUET, M.-T., CONAN, J.-M., MUGNIER, L.M. & ROUSSET, G. (1999). Noise Propagation in Wave-Front Sensing with Phase Diversity. Appl. Opt. **38**(23), 4967-4979.

MIKULA, S., TROTTS, I., STONE, J.M. & JONES, E.G. (2007). Internet-enabled high-resolution brain mapping and virtual microscopy. NeuroImage **35**(1), 9-15.

MILKIE, D.E., BETZIG, E. & JI, N. (2011). Pupil-segmentation-based adaptive optical microscopy with full-pupil illumination. Opt. Lett. **36**(21), 4206-4208.

NEIL, M.A., BOOTH, M.J. & WILSON, T. (2000). New modal wave-front sensor: a theoretical analysis. J Opt Soc Am A Opt Image Sci Vis **17**(6), 1098-1107.

NICOLLS, F.C., DE JAGER, G. & SEWELL, B.T. (1997). Use of a general imaging model to achieve predictive autofocus in the scanning electron microscope. Ultramicroscopy **69**(1), 25-37.

OGASAWARA, M., FUKUDOME, Y., HATTORI, K., TAMAMUSHI, S., KOIKARI, S. & ONOGUCHI, K. (1998). Automatic Focusing and Astigmatism Correction Method based on Fourier Transform of Scanning Electron Microscope Images. Jpn J Appl Phys **38**, 957.

OHEIM, M., BEAUREPAIRE, E., CHAIGNEAU, E., MERTZ, J. & CHARPAK, S. (2001). Two-photon microscopy in brain tissue: parameters influencing the imaging depth. J Neurosci Meth **111**(1), 29-37.

ONG, K.H., PHANG, J.C.H. & THONG, J.T.L. (1998). A robust focusing and astigmatism correction method for the scanning electron microscope—Part III: An improved technique. Scanning **20**(5), 357-368.

PAXMAN, R.G., SCHULZ, T.J. & FIENUP, J.R. (1992). Joint estimation of object and aberrations by using phase diversity. J. Opt. Soc. Am. A **9**(7), 1072-1085.

POMMIER, J. (2008). Simple SSE and SSE2 optimized sin, cos, log and exp. pp. C source code.

PRIETO, P.M., VARGAS-MARTIN, F., GOELZ, S. & ARTAL, P. (2000). Analysis of the performance of the Hartmann-Shack sensor in the human eye. J Opt Soc Am A **17**(8), 1388-1398.

RAGAZZONI, R. (1996). Pupil plane wavefront sensing with an oscillating prism. J Mod Optic **43**(2), 289-293.

RAPPAZ, B., MARQUET, P., CUCHE, E., EMERY, Y., DEPEURSINGE, C. & MAGISTRETTI, P. (2005). Measurement of the integral refractive index and dynamic cell morphometry of living cells with digital holographic microscopy. Opt Express **13**(23), 9361-9373.

RASMUSSEN, C.E. (2006). Matlab function *minimize.m*.

RICHARDS, B. & WOLF, E. (1959). Electromagnetic Diffraction in Optical Systems .2. Structure of the Image Field in an Aplanatic System. Proc R Soc Lon Ser-A **253**(1274), 358-379.

RIMMELE, T.R. & RADICK, R.R. Solar adaptive optics at the National Solar Observatory. In *Adaptive Optical System Technologies*, pp. 72-81. SPIE.

RODDIER, F. (1988). Curvature Sensing and Compensation - a New Concept in Adaptive Optics. Appl Optics **27**(7), 1223-1225.

ROPER, S., MOORES, M., GELIKONOV, G., FELDCHTEIN, F., BEACH, N., KING, M., GELIKONOV, V., SERGEEV, A. & REITZE, D. (1998). In vivo detection of experimentally induced cortical dysgenesis in the adult rat neocortex using optical coherence tomography. J Neurosci Meth **80**(1), 91-98.

RUDNAYA, M., MATTHEIJ, R. & MAUBACH, J. (2009). Iterative autofocus algorithms for scanning electron microscopy. Microsc. Microanal **15**(Suppl 2), 1108–1109.

RUDNAYA, M., TER MORSCHE, H., MAUBACH, J. & MATTHEIJ, R. (2011a). A Derivative-Based Fast Autofocus Method in Electron Microscopy. Journal of Mathematical Imaging and Vision, 1-14.

RUDNAYA, M.E., VAN DEN BROEK, W., DOORNBOS, R.M.P., MATTHEIJ, R.M.M. & MAUBACH, J.M.L. (2011b). Defocus and twofold astigmatism correction in HAADF-STEM. Ultramicroscopy **111**(8), 1043-1054.

RUECKEL, M., MACK-BUCHER, J.A. & DENK, W. (2006). Adaptive wavefront correction in two-photon microscopy using coherence-gated wavefront sensing. P Natl Acad Sci USA **103**(46), 17137-17142.

RUST, M.J., BATES, M. & ZHUANG, X. (2006). Sub-diffraction-limit imaging by stochastic optical reconstruction microscopy (STORM). Nat Meth **3**(10), 793-796.

SACCHET, D., MOREAU, J., GEORGES, P. & DUBOIS, A. (2008). Simultaneous dual-band ultra-high resolution full-field optical coherence tomography. Opt Express **16**(24), 19434-19446.

SAUVAGE, J.-F., FUSCO, T., ROUSSET, G. & PETIT, C. (2007). Calibration and precompensation of noncommon path aberrations for extreme adaptive optics. J. Opt. Soc. Am. A **24**(8), 2334-2346.

SCHARMER, G., BALASUBRAMANIAM, K.S. & RADICK, R.R. (1999). Object-Independent Fast Phase-Diversity. In *High Resolution Solar Physics: Theory, Observations, and Techniques*, Rimmele, T. R. (Ed.), pp. 330.

SCHERER, S.S. & WRABETZ, L. (2008). Molecular mechanisms of inherited demyelinating neuropathies. Glia **56**(14), 1578-1589.

SHACK, R.V. & PLATT, B.C. (1971). Lenticular Hartmann-screen. Optical Sciences Center Newsletter **5**(1), 15-16.

SHEPPARD, C. & COGSWELL, C. (1991). Effects of aberrating layers and tube length on confocal imaging properties. Optik(Stuttgart) **87**(1), 34-38.

SHEPPARD, C.J.R., ROY, M. & SHARMA, M.D. (2004). Image formation in low-coherence and confocal interference microscopes. Appl Optics **43**(7), 1493-1502.

SHERMAN, L., YE, J.Y., ALBERT, O. & NORRIS, T.B. (2002). Adaptive correction of depth-induced aberrations in multiphoton scanning microscopy using a deformable mirror. J Microsc-Oxford **206**, 65-71.

SRINIVASAN, V.J., RADHAKRISHNAN, H., JIANG, J.Y., BARRY, S. & CABLE, A.E. (2012). Optical coherence microscopy for deep tissue imaging of the cerebral cortex with intrinsic contrast. Opt. Express **20**(3), 2220-2239.

SUN, J., LEE, S.J., WU, L., SARNTINORANONT, M. & XIE, H. (2012). Refractive index measurement of acute rat brain tissue slices using optical coherence tomography. Opt. Express **20**(2), 1084-1095.

TEARNEY, G., BOUMA, B., BOPPART, S., GOLUBOVIC, B., SWANSON, E. & FUJIMOTO, J. (1996). Rapid acquisition of in vivo biological images by use of optical coherence tomography. Opt Lett **21**(17), 1408-1410.

TEARNEY, G.J., BREZINSKI, M.E., SOUTHERN, J.F., BOUMA, B.E., HEE, M.R. & FUJIMOTO, J.G. (1995). Determination of the Refractive-Index of Highly Scattering Human Tissue by Optical Coherence Tomography. Opt Lett **20**(21), 2258-2260.

THEER, P. & DENK, W. (2006). On the fundamental imaging-depth limit in two-photon microscopy. J Opt Soc Am A **23**(12), 3139-3149.

TOPILKO, P., SCHNEIDER-MAUNOURY, S., LEVI, G., BARON-VAN EVERCOOREN, A., CHENNOUFI, A.B., SEITANIDOU, T., BABINET, C. & CHARNAY, P. (1994). Krox-20 controls myelination in the peripheral nervous system. Nature **371**(6500), 796-799.

TÖRÖK, P., VARGA, P., LACZIK, Z. & BOOKER, G.R. (1995). Electromagnetic diffraction of light focused through a planar interface between materials of mismatched refractive indices: an integral representation. J. Opt. Soc. Am. A **12**(2), 325-332.

TROTTS, I., MIKULA, S. & JONES, E.G. (2007). Interactive visualization of multiresolution image stacks in 3D. NeuroImage **35**(3), 1038-1043.

TWYMAN, F. & GREEN, A. (1916). British patent No. 103832.

TYSON, R.K. (1997). *Principles Of Adaptive Optics*. Boston: Academic Press.

VABRE, L., DUBOIS, A. & BOCCARA, A.C. (2002). Thermal-light full-field optical coherence tomography. Opt Lett **27**(7), 530-532.

VO-DINH, T.E. (2003). *Biomedical Photonics Handbook*. Boca Raton: CRC Press.

WANG, H.F., FU, Y., ZICKMUND, P., SHI, R.Y. & CHENG, J.X. (2005). Coherent anti-stokes Raman scattering imaging of axonal myelin in live spinal tissues. Biophys J **89**(1), 581-591.

WANG, J., LEGER, J.-F., BINDING, J., BOCCARA, C., GIGAN, S. & BOURDIEU, L. Measuring aberrations in the rat brain by a new coherence-gated wavefront sensor using a Linnik interferometer. In *ProcSPIE*, Conchello, J.-A., Cogswell, C. J., Wilson, T. and Brown, T. G. (Eds.), pp. 822702-822707. SPIE.

YUAN, X., CHITTAJALLU, R., BELACHEW, S., ANDERSON, S., MCBAIN, C.J. & GALLO, V. (2002). Expression of the green fluorescent protein in the oligodendrocyte lineage: A transgenic mouse for developmental and physiological studies. Journal of Neuroscience Research **70**(4), 529-545.

ZOMMER, S., RIBAK, E.N., LIPSON, S.G. & ADLER, J. (2006). Simulated annealing in ocular adaptive optics. Opt. Lett. **31**(7), 939-941.

ZVYAGIN, A., SILVA, K.K.M.B., ALEXANDROV, S., HILLMAN, T., ARMSTRONG, J., TSUZUKI, T. & SAMPSON, D. (2003). Refractive index tomography of turbid media by bifocal optical coherence refractometry. Opt. Express **11**(25), 3503-3517.

11 List of Acronyms

2PLSM	Two-photon laser scanning microscopy
AO	Adaptive optics
CARS	Coherent anti-stokes Raman scattering microscopy
CGWS	Coherence gated wavefront sensing
CNP	Cyclic nucleotide phosphodiesterase
COM	Center of mass
deep-OCM	Deep optical coherence microscopy
DOF	Depth of field
EGFP	Enhanced green fluorescent protein
EM	Electron microscopy
FE-SEM	Field emission scanning electron microscope
ff-OCT	Full-field OCT
FPALM	Fluorescence photo activation localization microscopy
FT	Fourier transforms
FWHM	Full width at half maximum
MAPFoSt	Maximum a posterior focus and stigmation
MBP	Myelin basic protein
ML	Maximum likelihood
MTF	Modulation transfer function
NA	Numerical aperture
OCT	Optical coherence tomography
OCM	Optical coherence microscopy
PALM	Photoactivated localization microscopy
PNS	Peripheral nervous system
PSF	Point spread function
SBEM	Serial block-face electron microscopy
SEM	Scanning electron microscope
s.e.m.	standard error of the estimated mean
SHS	Shack-Hartmann sensor
SIM	Structured illumination microscopy
SNR	Signal-to-noise ratio
STED	Stimulated emission depletion
STORM	Stochastic optical reconstruction microscopy
THG	Third harmonic generation

12 French summary / Résumé substantiel de cette thèse

Introduction

Souvent, les découvertes en sciences sont liées à des nouvelles possibilités expérimentales. Une multitude des modes d'imagerie ont été inventée au cours du temps avec des propriétés très variées. En particulier, la microscopie joue un rôle fondamental pour la compréhension des systèmes biologiques. La découverte des cellules, les couches de tissu dans la peau, les formes variées des neurones, la formation des pili chez les bactéries n'en sont que quelques exemples.

L'organe humain le plus complexe à comprendre est sans doute le cerveau. Avec des prolongements des neurones de longueur typique d'une dizaine de centimètres, mais des diamètres de l'ordre du micromètre ou même dizaine des nanomètres, des microscopes avec une résolution très fine sur des champs d'observation énormes sont nécessaires. Pour l'analyse de la structure, des microscopes électroniques travaillant sur des échantillons fixés peuvent être très utile. En parallèle, la compréhension de la fonction du cerveau va dépendre de la faculté de visualiser en temps réel des changements dans le cerveau d'un organisme vivant en fonction de son environnement.

A l'échelle globale du cerveau, l'imagerie par résonance magnétique (I.R.M.), la tomographie à émission de positons (PET) et la tomodensitométrie peuvent être des méthodes utiles, mais pour une compréhension sur l'échelle des neurones individuels, la microscopie optique semble plus adaptée. Elle est peu destructive, ce qui permet l'imagerie in vivo, et bien résolue, de l'ordre du micromètre (ou mieux avec des nouvelles méthodes qui contournent la limite de la diffraction).

La microscopie optique en biologie est surtout limitée par deux effets : les limitations de profondeur de pénétration imposées par la diffraction et l'absorption de la lumière, et l'impossibilité d'obtenir la focalisation optimale de la lumière en présence d'aberrations optiques.

Aberrations optiques

Dans un système d'imagerie d'optique géométrique, tout rayon doit être focalisé au même endroit pour atteindre la résolution optimale (Figure 1a). Le terme « aberrations optiques » décrit tout effet de déviation des rayons du chemin désiré. En régime d'optique ondulatoire,

chaque onde individuelle doit arriver au foyer avec la même phase pour maximiser l'interférence constructive. Même des aberrations très faibles et qui ne changent pas d'une façon notable la direction des ondes peuvent induire des changements substantiels de phase relative. L'alignement des composants optiques d'un système optique peut induire des aberrations (Figure 1b), ainsi que les couches d'échantillons traversés (Figure 1c).

Une façon simple pour décrire mathématiquement les aberrations est par une fonction de front d'onde. Le front d'onde est la surface de phase constante d'une onde hypothétique qui, après propagation dans un système sans aberration, produit le même champ focal que l'onde réelle dans le système aberré. La fonction de front d'onde est la différence de phase spatiale entre un front d'onde sans aberration (donc plat ou sphérique) et le front d'onde avec aberrations.

Les sources principales des aberrations varient selon les modes d'imagerie. Pendant plusieurs siècles, la production des lentilles et miroirs n'était que partiellement maîtrisée, ce qui limitait plus ou moins fortement la qualité des images. Plus récemment, la qualité a augmenté jusqu'au point où, en astronomie, le chemin optique hors l'instrument lui-même devient le facteur limitant. Les turbulences atmosphériques, c'est-à-dire les fluctuations de densité et d'indice de réfraction de l'air, produisent des aberrations qui évoluent à grande vitesse.

En ophtalmologie, les imperfections de la cornée humaine limitent non seulement la vision du patient, mais aussi le diagnostic des maladies de la rétine basée sur l'imagerie de la rétine à travers l'œil.

En microscopie électronique, des lentilles électromagnétiques sont utilisées pour focaliser les électrons sur l'échantillon. Chaque changement de paramètre d'imagerie, par exemple du courant du faisceau ou de l'énergie des électrons, demande une correction des paramètres des lentilles pour éviter des aberrations.

En microscopie optique des échantillons épais, les couches superficielles et la structure de la surface peuvent générer des aberrations quand les couches en profondeur sont étudiées (Figure 1c). L'influence exacte dépend du type de microscope ; par exemple pour la microscopie confocale les aberrations sur les chemins d'excitation et d'émission sont d'une importance comparable, mais pour la microscopie à deux photons ce ne sont que les aberrations à l'excitation qui comptent en pratique.

Mesurer et corriger les aberrations

Pour la correction des aberrations, on peut intégrer un élément actif dans le chemin optique qui permet de modifier le profil spatial du front d'onde (Figure 1d). On parle alors d'une optique active ou d'une optique adaptative. Le concept joue un rôle important en astronomie et plus récemment en microscopie. En général, l'élément actif est la partie facile ; la vraie question est comment le piloter, c'est-à-dire comment mesurer les aberrations qu'il faut corriger.

En astronomie, c'est souvent possible de mesurer les aberrations directement, en utilisant la lumière d'une source ponctuelle suffisamment brillante. Cette lumière, par exemple issue d'une étoile proche de la zone d'intérêt, traverse la zone des turbulences atmosphériques avant d'arriver sur un senseur de front d'onde, par exemple un senseur Shack-Hartmann.

De la même façon, la lumière d'un laser peut être transmise par un élément optique de basse qualité qui produit des aberrations, et ce front d'onde analysée par le Shack-Hartmann (Figure 2). Ce senseur découpe le faisceau incident spatialement en le focalisant avec une grille de petites lentilles sur un détecteur résolu spatialement, comme une caméra CCD. La position de la tache focale sous chaque lentille par rapport à leur axe optique permet à remonter au tilt moyen du sous-faisceau incident sur cette lentille. Outre le Shack Hartmann, un senseur pyramidal, un senseur de courbure de front d'onde ou d'autres types d'interféromètre peuvent être utilisés pour l'analyse d'un front d'onde.

Malheureusement, ces méthodes ne sont pas facilement applicables à la microscopie 3D parce que ces méthodes nécessitent d'utiliser uniquement une source unique ponctuelle ou, au mieux, une source bidimensionnelle. Par exemple, la lumière fluorescente d'un échantillon biologique marqué à des positions différentes en 3D va générer, sur le CCD d'un Shack Hartmann, plusieurs systèmes des taches focales, plus ou moins focalisés grâce à leurs positions axiales différentes, qui vont en général être impossible à séparer.

Pour certains échantillons diffusant, une solution est le Coherence Gated Wavefront Sensing (CGWS) qui utilise un interféromètre de faible cohérence pour sélectionner le signal provenant d'une certaine profondeur, un algorithme numérique comparable au Shack Hartmann pour le dépliement de phase et une moyenne sur une petite zone spatiale pour s'affranchir des effets de tavelure sur le front d'onde. Hélas, la diffusion multiple limite

l'utilité du CGWS à des profondeurs de quelques libres parcours moyens ; de plus la méthode marche seulement pour des échantillons avec une distribution aléatoire des diffuseurs.

Détermination indirecte des aberrations par analyse d'images de test

Une alternative aux mesures directes du front d'onde est l'utilisation de méthodes indirectes basées sur l'analyse des images.

En général, un élément actif dans le chemin optique permet de modifier les aberrations du système d'une façon contrôlée. L'analyse de plusieurs images prises avec des configurations différentes de l'élément actif permet la détermination de la configuration optimale minimisant les aberrations.

Selon la façon de choisir les configurations pour les images de test et la façon d'analyser les données, on peut distinguer plusieurs catégories d'algorithme de mesure indirecte des aberrations.

Pour des techniques de microscopie nouvelles, un modèle mathématique de la formation de l'image n'est pas toujours disponible. Dans ce cas, on est limitée à prendre des images d'une façon plus ou moins aléatoire et à estimer leur qualité avec une métrique qui prend son maximum pour des conditions d'imagerie sans aberrations. Par exemple, on peut utiliser le contraste de l'image comme métrique, parce qu'il ne peut que diminuer avec l'ajout d'aberrations. Après l'acquisition de quelques images et le calcul des valeurs de la métrique pour chaque perturbation ajoutée, un algorithme heuristique est utilisé pour déterminer les prochains paramètres de correction à tester. Cet algorithme heuristique peut être basé, par exemple, sur le gradient des valeurs de la métrique, sur une optimisation génétique ou alors sur des méthodes de recuit simulé.

Souvent, il est possible d'analyser mathématiquement l'effet des aberrations sur la formation d'images dans un système optique. Dans ce cas, on ne sait pas seulement qu'une certaine métrique va prendre son maximum quand toute aberration a été corrigée, mais on peut déduire d'une façon précise comment la valeur de la métrique va diminuer avec l'introduction des aberrations. Cette analyse permet de choisir d'une façon intelligente la paramétrisation des aberrations et les images de test à prendre, et d'en déduire avec efficacité les paramètres optimaux de correction.

En particulier, on peut choisir une paramétrisation ou tous les paramètres sont orthogonaux; c'est-à-dire que la correction d'une de ces aberrations ne change jamais les valeurs optimales pour les autres paramètres. Cette approche s'appelle mesure modale de front d'onde.

Les méthodes décrites jusqu'ici sont toutes basées sur des images de test prises avec une modulation des aberrations, donc avec une modulation de la phase du faisceau. Le Shack Hartmann, par contre, sépare spatialement le faisceau en sous-faisceaux pour l'analyse des pentes locales.

Cette approche a été transformée en méthode indirecte sous le nom de segmentation de pupille (Section 1.9.3). Le diamètre du faisceau d'excitation d'un microscope à deux photons est réduit et plusieurs images sont prises pour différentes positions de ce faisceau dans la pupille de l'objectif. Chaque image est déplacée latéralement en fonction du tilt moyenne du front d'onde sur la sous-pupille utilisée. La corrélation de ces images permet alors la détermination des pentes locales du front d'onde, comme dans le Shack Hartmann.

La mesure modale et la segmentation de pupille sont des approches assez différentes ; la question se pose de savoir s'il n'est pas possible de trouver un algorithme plus général dont les deux approches ci-dessus sont des cas particuliers. Et effectivement, la diversité de phase, qui a été développée en astronomie comme méthode d'analyse basée sur un modèle du processus d'imagerie peut, d'une façon naturelle, accommoder modulations d'amplitude et de phase. Les applications existantes en microscopie plein champ n'utilisent pas ce cadre probabiliste qui donne une force prédictive maximale, pourvu que le modèle du microscope et le modèle du bruit soient suffisamment bien connus.

Pour démontrer la puissance de la diversité de phase dans un système de microscopie simple, je présente dans cette thèse l'algorithme Maximum-A-Posteriori Focus and Stigmation (MAPFoSt) qui permet la correction de la mise au point et de l'astigmatisme avec seulement deux images de test (Chapitre 6).

Pour explorer si des aberrations optiques jouent une rôle important dans l'imagerie optique du cortex des rats, nous avons développé une modalité de microscopie par cohérence optique qui a permis la mesure exacte et in vivo de l'indice de réfraction moyenne du cerveau du rat.

Le microscope est décrit en chapitre 2, les valeurs d'indices trouvés en chapitre 4. Dans le chapitre 3, je montre que ce microscope permet la visualisation des fibres myélinisées à la fois

dans le cortex et dans le système nerveux périphérique. Les conséquences de la valeur de l'indice de réfraction pour la microscopie à deux photons et la justification de la nécessité de l'optique adaptative dans ce système sont présentées dans le chapitre 5.

Deep-OCM

Le microscope par cohérence optique optimisé pour l'imagerie profonde (deep-OCM) développé au cours de cette thèse (Chapitre 2) est une combinaison de plusieurs améliorations de l'OCT plein champ (Figure 2-1). La source lumineuse est une lampe halogène (250 W) qui forme, sans filtre spectral, le centre d'une illumination Köhler. La caméra InGaAs permet alors d'obtenir un spectre effectif large dans l'infrarouge centré sur λ=1100 nm avec une largeur à mi-hauteur de 170 nm.

La lumière entre un interféromètre Linnik, donc un interféromètre de Michelson avec un objectif de microscope dans chaque bras. L'objectif de grande ouverture numérique dans le bras objet permet des grandissements considérables, mais avec des quantités de dispersion très variables sur le champ. Pour corriger cette dispersion correctement pour tout le champ en même temps, ce n'est pas suffisant de mettre un bloc de verre dans le bras de référence ; il faut utiliser un objectif identique à celui du bras d'objet.

La séparation du signal interférométrique et du fond lumineuse se fait par la modulation de la longueur de bras de référence. Le miroir placé au foyer de l'objectif de référence est déplacé par un piezo synchronisé à l'acquisition de la caméra infrarouge.

La correction automatisée du défocus (défaut de mise au point) est une propriété importante du deep-OCM. Dans des échantillons ayant un indice de réfraction légèrement différent de celui du milieu d'immersion, le plan d'imagerie défini par l'effet de cohérence s'éloigne du foyer de l'objectif en pénétrant le tissu (Figure 4-1). Une adaptation continue de longueur de bras de référence est nécessaire pour synchroniser leur pénétration dans l'échantillon, ce qui maximise la netteté des images et le niveau de signal. Deux platines de translations motorisées sont nécessaires pour la correction automatique de défocus, dont une peut être la platine qui bouge l'échantillon par rapport au microscope (Section 9.1). Dans le cerveau du rat, cette correction augmente par un facteur de 2,5 la profondeur maximale d'imagerie atteignable.

Imagerie de myéline avec deep-OCM

L'imagerie de la myéline dans le cerveau, mais aussi dans le système nerveux périphérique, est importante pour la recherche sur plusieurs neuropathies, comme la sclérose en plaques.

Sur des échelles spatiales de l'ordre du millimètre, il est possible de visualiser la myélinisation avec l'I.R.M.. Malheureusement, cette technique n'est pas capable de distinguer des fibres individuelles ; pour cette raison, la myélinisation éparse de la matière grise n'est pas accessible. La microscopie Coherent Anti-Stokes Raman Scattering (C.A.R.S.) et la microscopie Third Harmonic Generation (T.H.G.) peuvent résoudre le problème, mais seulement pour des faibles profondeurs de pénétration à l'ordre de 30 ou 50 microns.

En dehors du problème de la présence de tavelures dans les images, le deep-OCM peut atteindre les mêmes résolutions que les microscopies C.A.R.S. et T.H.G.. Dans le cerveau du rat, nous sommes capables de visualiser des fibres individuelles jusqu'à la profondeur de 340 microns (Figure 3-5). Ces fibres sont également visibles dans le cerveau d'une souris transgénique, où une étude de co-localisation avec des sondes fluorescentes a pu démontrer que le deep-OCM est sensible aux fibres myélinisées (Figure 3-2). Dans le cortex des rats âgés de 3, 6 et 12 semaines, la densité des fibres dépend fortement de l'âge (Figure 3-3, 3-6). L'imagerie à grand champ du cervelet démontre que c'est bien les fibres myélinisées qui sont le plus visible en deep-OCM (Figure 3-4).

Le deep-OCM nous permet également l'imagerie des fibres dans le nerf sciatique d'une souris, même in vivo (Figure 3-8) ; la comparaison entre le nerf d'une souris saine et le nerf d'une souris transgénique qui a une myélinisation limitée montre qu'il est possible de faire la différence entre les deux cas (Figure 3-7).

Pour le diagnostic de neuropathie chez l'homme, il semble possible d'envisager l'utilisation du deep-OCM pour remplacer des biopsies de nerf périphérique qui sont nécessaires aujourd'hui pour certains diagnostics des maladies nerveuses. De plus, la profondeur de pénétration dans le cerveau pour l'imagerie des fibres myélinisées individuelles pourrait jouer un grand rôle dans la recherche des maladies auto-immunes. Sans marquage chimique, il est possible d'utiliser le deep-OCM pour suivre la démyélinisation et la remyélinisation éventuelle en fonction des traitements expérimentaux.

Indice de réfraction du cerveau de rat in vivo

Pour tout modèle optique du cerveau, l'indice de réfraction est un paramètre important ; notamment pour le calcul des aberrations dues au tissu. Etant donné qu'il n'y avait pas de mesures in vivo de l'indice du cerveau des rats, nous avons utilisé le deep-OCM pour le mesurer.

À la base de la méthode de mesure est l'indépendance du plan d'imagerie de l'OCM, qui est fixée par la longueur du bras de référence, du plan focal de l'objectif. Le mouvement du premier par rapport au deuxième modifie la netteté et surtout le niveau de signal du deep-OCM, avec un maximum quand les deux sont bien superposés. Un changement d'indice de réfraction bouge le plan d'imagerie et le plan focal dans des directions opposées (Figure 4-1). La distance entre ces deux plans, qui peut être déterminée en optimisant de nouveau la superposition des deux plans, donne une information sur l'indice de réfraction moyen du tissu traversé si on la regarde en fonction de la profondeur dans le tissu.

Etant donné la largeur du spectre utilisé dans notre système et la grande ouverture numérique, le modèle mathématique du système que nous avons établi prend en compte la dépendance de l'indice de réfraction avec la longueur d'onde mais aussi le changement du chemin optique avec l'angle d'incidence et de rétrodiffusion dans le tissu (Figure 4-2). En faisant le choix d'une hypothèse sur la dispersion dans le tissu, il est possible de déterminer numériquement la valeur de l'indice de réfraction en utilisant les mesures décrites dans le dernier paragraphe.

Nos mesures dans les cerveaux de sept rats âgés de 3, 6 et 12 semaines dans, en total, 19 positions latérales différentes montrent une certaine variation de l'indice de réfraction. Étrangement, la variation n'était pas liée à la profondeur dans le tissu, ni à l'âge des animaux (Figure 4-3). La valeur moyenne trouvé était n' = 1.3526 ± 0.0029 (écart type), ± 0.0007 (erreur standard de moyen) dans la gamme de longueur d'onde $\lambda = 1.1 \pm 0.1$ µm. L'indice de réfraction de l'eau pure dans cette gamme de longueur d'onde varie de n = 1.3222 à n = 1.3252. Ces valeurs sont plutôt faibles en comparaison des mesures faites dans des tranches de tissu, mais en bon d'accord avec des mesures in vivo récemment publiées.

Conséquences de la valeur de l'indice pour la microscopie à deux photons

Pour déduire les conséquences de la valeur de l'indice de réfraction du tissu pour la microscopie à deux photons, il est en principe nécessaire de connaître l'indice partout dans le cône de tissu traversé par la lumière jusqu'au foyer. Avec notre technique, nous pouvions

seulement déterminer l'indice moyen sur le volume traversé, du coup il n'est pas possible de remonter aux aberrations complètes (i.e. aux fluctuations locales de l'indice).

Néanmoins, notre résultat suffit pour déterminer une limite basse sur les aberrations, notamment par un calcul des aberrations sphériques en utilisant l'hypothèse d'un indice de réfraction homogène. Ces aberrations sphériques peuvent être exprimées en termes de pertes de résolution et de pertes de signal pour le cas de la microscopie biphotonique (Figure 5-1). D'après notre calcul, les résolutions axiale et latérale devraient rester à peu près constantes jusqu'à des profondeurs de 200 μm. En même temps, le niveau du signal commence à décroître déjà à quelques dizaines de micromètres de profondeur et atteint autour de 60 % du maximum à 200 μm de profondeur pour un objectif d'ouverture numérique de 1,0 à la longueur d'onde d'excitation de 1,1 μm. À 400 μm de profondeur, la résolution axiale a diminué par un facteur de 2 et le signal n'atteint que 15 % de la valeur en surface.

Des résultats expérimentaux récemment publiés montrent que les pertes réelles de résolution sont encore pires, ce qui implique que notre modèle d'un indice de réfraction homogène n'explique pas à lui seul les aberrations.

Maximum-A-Posteriori Focus and Stigmation (MAPFoSt)

En microscopie électronique à balayage, un faisceau d'électrons de haute énergie est focalisé sur la surface d'un échantillon. L'interaction des électrons avec l'échantillon peut produire des électrons secondaires, mais aussi rétrodiffuser une partie des électrons. Les deux sortes d'électrons peuvent être distinguées grâce à leur énergie différente. Les détecteurs ne sont pas résolus spatialement, donc le volume d'interaction et par conséquent la PSF sont déterminés seulement par la focalisation et l'énergie du faisceau incident.

Pour atteindre une résolution maximale, la distance focale des lentilles électromagnétiques doit être ajustée à la position de l'échantillon. De plus, les imprécisions dans le système ou bien des champs extérieurs peuvent induire de l'astigmatisme qui doit être compensé avec deux circuits intégrés dans le microscope électronique. Le comportement précis du faisceau peut changer avec le temps, par exemple à cause de dérives thermiques lentes. De plus, chaque changement de paramètres de microscopie, comme la distance de travail, l'énergie des électrons, le courant total du faisceau incident etc… peut modifier les valeurs optimales pour l'astigmatisme et pour la distance focale. C'est donc important d'avoir un moyen automatisé d'optimisation de ces paramètres d'aberrations.

Etant donné le petit nombre de paramètres à optimiser pour maximiser la résolution, ce n'est pas difficile d'implémenter un algorithme basé sur une métrique de qualité qui corrige un paramètre après l'autre, si nécessaire d'une façon itérative. Malheureusement, des échantillons biologiques sont souvent très fragiles et nécessitent de minimiser la dose d'électrons utilisée pendant l'optimisation de la PSF. Il est clair que chaque image contient bien plus d'informations sur la PSF qu'on pourrait espérer extraire avec une seule métrique. Surtout avec plusieurs images de test pris avec des paramètres d'aberrations différents, l'analyse devrait prendre en compte la différence d'aberrations entre les images (qui est connue), le fait que l'objet est en général stationnaire et l'interaction entre l'objet et la PSF aberrée.

On pourrait envisager d'analyser les images avec plusieurs métriques, jusqu'à utiliser une métrique par fréquence spatiale dans l'image. Dans ce cas, il se pose la question de la façon de combiner l'information potentiellement complémentaire de toutes ces métriques pour arriver à la meilleure estimation d'aberrations possible avec des données basées sur une dose d'électrons fixes.

En astronomie, une technique d'estimation de front d'onde basée sur deux ou plusieurs images de test a été décrite sous le nom de diversité de phase. L'idée de base est de regarder les images de test dans l'espace de Fourier. Chaque image peut donc être exprimée comme le produit de la transformée de Fourier de l'objet avec la transformée de Fourier de la PSF (qu'on appelle fonction de transfert de modulation, MTF) plus du bruit. Si un modèle de la MTF est disponible, on peut séparer l'influence de l'objet sur l'image de l'influence de la MTF. Des implémentations de cette idée de base existent déjà même en microscopie électronique, mais avec des propriétés peu favorables par rapport aux images très bruitées qu'on peut utiliser pour notre algorithme.

Pour démontrer la puissance de la diversité de phase pour la microscopie, nous avons développé l'algorithme Maximum-A-Posteriori Focus and Stigmation (MAPFoSt) qui analyse deux images de test de notre microscope électronique dans l'esprit de l'inférence bayésienne. Par rapport aux implémentations de la diversité de phase en astronomie, MAPFoSt permet l'analyse des données d'une façon plus efficace, parce que nous utilisons un modèle pour la MTF qui contient seulement le défaut de mise au point et l'astigmatisme de premier ordre et qu'on peut du coup calculer en temps linéaire, sans utilisation de transformée de Fourier.

Le processus d'imagerie

Nous travaillons sous l'hypothèse de l'invariance de translation, c'est-à-dire que le faisceau d'électrons ne change pas sa forme pendant le balayage. Nous supposons aussi que la courbure de champ est négligeable et qu'on peut approximer le bruit dans les images par une distribution gaussienne. Nous utilisons pour notre système la théorie d'optique des rayons au lieu de la théorie d'optique des ondes parce que les tailles de pixel utilisé (5-80 nm) sont bien supérieures à la limite de la diffraction (autour de 1,7 nm dans notre cas).

Dans l'espace réel, l'image peut être exprimée comme convolution de l'objet avec la PSF, à qui s'ajoute le bruit. Dans l'espace de Fourier, cela correspond à dire que l'image est le produit de l'objet avec la MTF ; étant donné qu'on suppose que le bruit est un bruit gaussien blanc, on peut directement modéliser le bruit dans l'espace de Fourier (Équation 6-2).

La PSF est un disque solide elliptique. Ses dimensions et son orientation dépendent des paramètres d'aberrations (défaut de mise au point, astigmatisme sur l'axe et l'astigmatisme en diagonale). Sa transformée de Fourier, la MTF, peut s'exprimer d'une façon simple avec une fonction de Bessel (Équation 6-4).

La probabilité d'acquérir une certaine image de test ($\mathbf{I_1}$) sachant les aberrations actuelles ($\tilde{\mathbf{A}} + \mathbf{T}_1$) et connaissant l'objet ($\mathbf{O}$) est une simple distribution gaussienne (Équation 6-12). Avec le théorème de Bayes, on peut remonter à la probabilité jointe de certaines valeurs d'aberrations et d'un certain objet en utilisant deux images de test (Équation 6-14). Le choix d'une probabilité a priori assez simple pour l'objet (par exemple, une gaussienne ou alors un top-hat) peut permettre la détermination analytique du maximum de la fonction de probabilité par rapport à l'objet. Ce maximum, qui dépend encore de l'aberration, peut être considéré comme projection maximale de la distribution de probabilité a posteriori ; il s'appelle profil de la distribution de probabilité a posteriori (Équation 6-27). Pour déterminer les aberrations les plus probables connaissant deux images de test, il suffit de déterminer la valeur $\mathbf{A}$ qui maximise le profil de la distribution de probabilité a posteriori.

Résultats

En utilisant des paires d'images de test simulées, nous trouvons qu'on peut estimer et le défaut de mise au point et l'astigmatisme avec des aberrations de test de quelques microns de défaut de mise au point. La précision d'estimation décroît avec l'augmentation des aberrations, mais l'algorithme fonctionne sans biais (Figure 6-4). L'erreur de l'estimation dépend de façon

inverse de la dose totale utilisée pour les images de test (Figure 6-5), mais peu de la taille en pixel des images si la dose totale reste constante. La valeur optimale pour le défocus de test décroît avec la fréquence spatiale et, à une fréquence spatiale de l'image fixe, avec la taille d'aberrations actuelles (Figure 6-6). Pour une situation expérimentale, le choix de la valeur de défocus de test est donc un compromis entre les différentes fréquences spatiales présentes dans l'image.

Avec des paires d'images expérimentales, nous avons trouvé que l'algorithme marche en principe, mais que le système des coordonnées de l'astigmatisme utilisé par notre microscope a subi une rotation par rapport au système utilisé dans notre logiciel (Figure 6-7).

Pour estimer correctement les aberrations dans des images expérimentales, il faut d'abord estimer correctement l'ouverture numérique du faisceau incident des électrons (qui joue le rôle de facteur d'échelle pour toutes les aberrations), la rotation du système des coordonnées de l'astigmatisme et aussi l'échelle des unités utilisées pour l'astigmatisme. Ces paramètres devraient en théorie dépendre seulement du microscope, mais pas de l'échantillon. Nous avons testé plusieurs configurations de travail avec plusieurs échantillons différents pour vérifier cette indépendance (Table 6-1). Même si les valeurs préalablement déterminées indépendamment n'étaient correctes que pour l'ouverture numérique et la rotation d'astigmatisme, l'échelle d'astigmatisme trouvé pour les conditions de travail différent était, entre eux, grosso modo cohérent.

Si l'analyse MAPFoSt est basée seulement sur les basses fréquences spatiales de l'image, une estimation imprécise des aberrations est néanmoins possible. Les fréquences moyennes contribuent beaucoup pour améliorer la précision d'estimation, mais les hautes fréquences sont souvent dominées par le bruit et n'ajoutent aucune information (Figure 6-8).

La correction d'aberrations avec MAPFoSt est possible sur des échantillons très divers (Figure 6-9) à une taille de pixel de 80 nm ou alors de 20 nm. Si les paramètres du microscope, comme l'ouverture numérique et les unités utilisées pour les paramètres d'astigmatisme, ne sont pas connues assez précisément, la convergence sur les paramètres nécessaires pour une correction d'aberrations optimales ne se fait pas en un seul pas. Un petit nombre de paires d'images est donc nécessaire pour atteindre la résolution finale (Figure 6-10). Si les paramètres sont connus précisément, c'est possible de diminuer les aberrations par un facteur entre 12 et 100 avec une seule paire d'images. La taille du faisceau au foyer peut diminuer à

des valeurs bien inférieures à la taille des pixels utilisés pour la détermination des aberrations (Figure 6-11).

Notre intérêt principal pour l'utilisation de MAPFoSt est de focaliser sur des zones différentes du cerveau de rat avec la dose minimale, pour pouvoir prendre des images de grandes surfaces, jusqu'à la taille du cerveau entier, avec une taille de pixel de 80 nm pour suivre sur des longues distances les connexions myélinisées du cerveau. Le temps total de cette acquisition est estimé à plusieurs mois au moins. Il est donc important que notre algorithme marche sur des zones de tissu de contraste et de contenu très variable, ce que nous pouvions constater pendant nos tests (test cases 1 et 2).

Notre algorithme doit permettre de déterminer quand il n'a pas été capable de focaliser correctement sur une zone d'échantillon, pour faciliter l'intervention de l'homme si nécessaire. Comme métrique de succès, nous utilisons la courbure du profil de probabilité postérieure au maximum (Équation 6-31). Cette courbure correspond, pour une fonction de probabilité gaussienne, à la matrice des covariances des paramètres d'aberrations. Elle a tendance à être trop optimiste parce qu'elle néglige les corrélations entre l'estimation des aberrations et l'estimation de l'objet (Figure 6-5e) ; il est donc préférable de mettre une valeur limite qui est inférieure à la valeur maximale réellement acceptable, par exemple par un facteur de deux ou trois.

Nous avons comparé les performances de notre algorithme MAPFoSt avec l'autofocus intégré de notre microscope électronique (ZEISS MERLIN avec logiciel SmartSEM). Pour nos échantillons biologiques, l'algorithme de Zeiss n'a pas réussi à réduire les aberrations suffisamment dans 23 % des cas, avec une erreur résiduelle avec un écart type de 4,5 μm. Pour les mêmes conditions, MAPFoSt réussissait toujours, laissait que 1,2 μm (écart type) d'erreur résiduelle et réduisait le temps d'exposition et du coup la dose par un facteur 10 (Figure 6-12a).

Pour un autre échantillon, avec des structures d'or sur une surface de charbon avec des structures de taille caractéristique entre 5 et 150 nm, l'algorithme de Zeiss ne marchait pas dans 24 % des cas ; notre propre algorithme marchait toujours sauf dans un seul cas (5 %), probablement à cause d'une valeur imprécise de l'ouverture numérique (Figure 6-12b). En résumé, MAPFoSt est plus fiable et plus précis que l'algorithme commercial, tout en utilisant moins d'une dixième de la dose.

144

Discussion

Dans ce projet de thèse, nous avons présenté une nouvelle méthode de microscope optique par cohérence, nommée deep-OCM, qui est optimisée pour l'imagerie avec une résolution du micromètre à des profondeurs de plusieurs centaines de micromètres dans des échantillons diffusants avec un indice de réfraction légèrement différent de celui de l'eau.

Une des structures principales accessibles au deep-OCM sont des fibres myélinisées individuelles dans le cortex des rongeurs. Il n'était pas auparavant possible de les imager à des profondeurs jusqu'à plus que 300 μm, ce qui pourrait dans le futur aider au diagnostic des neuropathies chez l'homme, mais aussi pour la compréhension de ces maladies dans des modèles animaux.

Le deep-OCM permet également de mesurer l'indice de réfraction moyen du tissu in vivo. Cette méthode a été utilisée jusqu'à maintenant avec des systèmes d'OCT de basse ouverture numérique. Nous l'avons adapté pour prendre en compte des ouvertures numériques arbitraires ainsi que des hypothèses plus variées sur la dispersion dans le tissu. Les valeurs d'indices de réfraction trouvée dans le cerveau des rats âgés de 3, 6 et 12 semaines ne dépendent pas d'une façon significative de l'âge, ni de la profondeur dans le tissu. Néanmoins, il y avait des fluctuations de l'indice d'une position latérale à l'autre, qui était de même ordre que la variation entre les animaux. Utilisant l'hypothèse que la dispersion dans le tissu est égale à la dispersion dans l'eau, nous trouvons une valeur moyenne qui est à peu près 2 % supérieure à l'indice de réfraction de l'eau pure.

À cause de cette valeur d'indice de réfraction, l'aberration sphérique limite la résolution et le niveau de signal pour la microscopie à deux photons avec des objectifs d'ouverture numérique de 1,0 à des profondeurs de moins de 400 μm. Il est donc important de compenser les aberrations avec une optique adaptative pour profiter de la résolution maximale et de la meilleure profondeur de pénétration possible. Les résultats récents montrent que, effectivement, la correction des aberrations en microscopie à deux photons peut augmenter le signal et la résolution.

Néanmoins, pour chaque projet de microscopie, on doit se poser la question de savoir si la complexité ajoutée par une optique adaptative est réellement justifiée. Au minimum, il faut introduire l'élément actif dans le chemin optique, qui nécessite souvent des éléments additionnels par exemple pour la conjugaison des plans et pour la calibration. La qualité

optique des éléments actifs « désactivés » est généralement très mauvaise, c'est-à-dire qu'au début de chaque expérience il faut généralement trouver les paramètres de l'élément actif qui compensent ses propres aberrations, avant de commencer à compenser les aberrations du reste du système et de l'échantillon.

Cette complexité additionnelle peut diminuer l'utilité du microscope, en particulier pour des expériences in vivo de longue durée ou l'incertitude apportée par l'aspect biologique demande une grande fiabilité du microscope. En même temps, si un algorithme d'optimisation des aberrations fiable est disponible, l'optique adaptative peut augmenter la stabilité du système.

Pour le deep-OCM, la correction du défaut de la mise au point est un facteur important pour atteindre les grandes profondeurs. Étant donné que l'optimisation de longueur de bras de référence est en tout cas nécessaire de temps en temps pour compenser des dérives thermiques, l'automatisation de cette procédure, qui ne nécessite qu'un seul moteur additionnel et un peu de programmation, réprésente une amélioration notable de la fiabilité du système. Par ailleurs, l'aspect de correction du défaut de mise au point induit par la pénétration dans un échantillon avec un indice de réfraction différent de celui du médium d'immersion devient de plus en plus important avec l'augmentation de l'ouverture numérique des objectifs utilisés.

Pour des méthodes fiables de mesure d'aberrations en microscopie, nous travaillons encore sur le CGWS, qui pourrait en principe fournir une mesure directe des aberrations dans des échantillons biologiques diffusants, mais qui est fortement limitée par la diffusion multiple pour les objectifs de grande ouverture numérique (les seuls pour lesquels l'optique adaptative est vraiment intéressante).

De ce fait, nous avons aussi travaillé sur des méthodes de mesures d'aberrations indirectes. Le concept de diversité de phase a été exploité en astronomie avec une rigueur qui manque en microscopie dans les implémentations existantes. Pour démontrer la puissance de cette méthode, si elle est basée sur une approche statistique, nous avons implémenté un algorithme pour notre microscope électronique qui permet de déterminer la valeur du défaut de mise au point et de l'astigmatisme en n'utilisant que deux images de test prises avec une petite différence de défaut de mise au point. Notre algorithme n'a pas besoin de faire des transformées de Fourier pendant la recherche numérique du maximum de la fonction de

probabilité, ce qui accélère fortement le calcul par rapport aux algorithmes existants en astronomie et qui permet l'exploitation des images bien plus grandes.

La diversité de phase basée sur une approche statistique a le potentiel d'aller au-delà de la microscopie électronique à balayage. Il pourrait être appliqué à d'autres types de microscope électronique et aux microscopies optiques. À partir du moment où un modèle théorique pour un système d'imagerie est disponible qui décrit l'effet des aberrations sur les images et les sources dominantes de bruit, il devrait être possible d'implémenter la diversité de phase basée sur l'inférence bayésienne à ces microscopies, comme nous l'avons fait avec MAPFoSt.